Terminal Behavioral Modeling of Electric Machines for Real-Time Emulation and System-level Analyses

Arash Nazari

Thesis submitted to the faculty of the Virginia Polytechnic Institute and State University in partial fulfillment of the requirements for the degree of

Master of Science
In
Electrical Engineering

Dushan Boroyevich, Chair

Igor Cvetkovic, Co-Chair

Mohamed Belkhayat

May 9, 2022

Arlington, Virginia

Keywords: Modeling and simulation, active rectifier, System stability study, linearization, permanent magnet synchronous machine, induction machine, motor control, Hardware-In-The-Loop (HIL), Power Hardware-In-The-Loop (PHIL)

Terminal Behavioral Modeling of Electric Machines for Real-Time Emulation and System-level Analyses

Arash Nazari

Abstract

The stability of interconnected power converter systems has been an important focus of study in the field of power electronics and power systems. With the ever-increasing application of electrical machines by means of electrification of vehicles, airplanes, and shipboards, a detailed study of the related dynamics is very important to ensure the proper implementation and stable behavior of the overall system. Linearization of rotating machine dynamics is well established. However, hardware techniques that verify these linear models are not well established. The present thesis advances a new technique for the hardware verification of a linear TBM of a PM machine. This technique can be extended to other types of machines. Using this modeling method, it is possible to have accurate behavior of electrical and mechanical terminal dynamics of the machine without detailed information about the internal structure of the machine, material characteristics, or topology of the machine. Instead, an accurate model of the electrical and mechanical terminals of the machine is achieved by measuring specific frequency responses of the machine to distinguish the dynamic relation of the various electrical and mechanical quantities of the machine. The directly measured frequency responses are coupled with the dynamics of the source and load in the electrical and mechanical terminals of the machine thus in order to decouple the described dynamics a mathematical process is used that results in decoupling of the controller and drive on the electrical side and the dynamics of the mechanical load and mechanical shaft at the mechanical terminal of the machine. The resulting model is the linear time-invariant representation of the electrical machine at a specific operating point of interest. Additionally, this work represents the application of this modeling method for accurate measurement of internal parameters of the machine such as inductances and mechanical inertia, and also characterization of the mechanical shaft coupler. The resulting unterminated model of the machine is a very important matter of information for system integrators and electrical and mechanical

designs related to the application of the machine, to ensure the stable and sustainable operation of the machine. By incorporating and integrating a combination of commercially available devices such as frequency response analyzer, Hardware-In-The-Loop (HIL), Power-Hardware-In-The-Loop (PHIL) and various other electrical and mechanical sensors, a test setup has been developed that is capable of operating and studying arbitrary frame small-signal related measurements required for terminal behavioral modeling of the electrical machines. The resulting model of the machine that has been extracted from this modeling method is then used to compare in the time domain with the real machine in the case of transient change in the mechanical load on the shaft to discover the validity of this modeling procedure.

Terminal Behavioral Modeling of Electric Machines for Real-Time Emulation and System-level Analyses

Arash Nazari

General Audience Abstract

According to the data from the International Energy Agency, around half of the electricity used globally is consumed by electric motors. Moreover, the growth in the electric vehicle industry will increase their application even further, hence the development of high-fidelity models of electric machines for real-time emulation, system-level analyses, and stability studies still stands out as an important and needed research focus. New modeling concepts that go beyond the standard industry practice can be used at the design and integration stage to ensure the stable behavior of the overall system. Furthermore, convenient testing and identification pressures can help ensure the long-term operation of the system. Aligned with this trend, this thesis is studying permanent magnet synchronous machines (PMSM) using small-signal terminal-behavioral three-port networks. Having such a behavioral model of the machine available provides many opportunities for system integrators, and even enables an *in-situ* system observation and stability assessment at both the machine's electrical and mechanical interfaces. This capability can undoubtedly be of high importance in practice, as it offers new insights into dynamic interactions of the electro-mechanical systems, the governor or turbine control design in ships, aircraft, electrical vehicles, and even large synchronous machines in power plants. A so-called characterization testbed has been built that combines Hardware-In-The-Loop (HIL) and Power-Hardware-In-The-Loop (PHIL) environments, with sensor-interface boards that are used to properly scale measured signals for machine control. The frequency-response-analyzer is used to sweep the proper electrical or mechanical terminal of the machine by perturbing the proper control signal within the machine controller running in PHIL and reading *d-q* currents, voltages, torque, and speed variables whose dynamic ratios are then obtained without the need for interrupting the normal operation of the electrical machine.

The capability of acquiring such a detailed model of the machine while the machine is in operation is an important benefit of this modeling method, in comparison to the conventional identification methods widely applied in the industry. The resulting model is a linearized time-invariant representation of the electrical machine at a specific operating point of interest and can be used by system integrators to ensure the stability of the system using well-known stability assessment methodologies. Furthermore, this modeling strategy has been experimentally verified for the first time on electrical machines, and the resulting model has been compared with the transient behavior of the machine in the presence of a step change in the mechanical load of the machine.

To my mother ***Sakineh Nazari***

Acknowledgment

I am delighted to have an opportunity to thank all of those who supported me during my graduate program at Virginia Tech.

First and foremost, I would like to express my gratitude for my advisor Dr. Igor Cvetkovic for giving me the opportunity to pursue my graduate research at the Center for Power Electronics Systems (CPES), Virginia Tech. His guidance, insightful discussions and continued support has allowed me to perform my research. I am especially thankful for his generous approach to guidance and significant openness towards my research.

I am also very thankful to my co-advisor Dr. Dushan Boroyevich for all the time he spent with me during my research. I am very thankful for all technical discussions, opinions and suggestions and support during my research.

I would also want to thank my committee member Dr. Mohamed Belkhayat for his thoughtful suggestions, insightful discussions and kind support. Every discussion with him has always sparked un-foreseen and fruitful paths in my research. His valuable inputs have significantly influenced my research.

I am grateful for my very intelligent friends at Arlington lab, Mr. Haris Bin Ashraf, Mr. Vladimir Mitrovic, Mr. Milad Abtin, Mr. Jack Knoll, Mr. Taha Moaz, Mr. He Song, Ms. Qian Li, Mr. Vinay Mutyala, Mr. Benjamin Albano, Dr. Fabiano Costa and Dr. Bo Wen. I am also grateful for the CPES staff, including, Ms. Audri Cunningham, Mr. Dennis Gove, Mr. Matthew Scanland, Mr. David Gilham, Ms. Teresa Rose, Ms. Na Ren, Mr. Neil Croy, Ms. Angela Diamon, and Ms. Brandy Grim.

Last but not least, I wish to thank my family for their continuous support during all stages of my life. Words cannot demonstrate my appreciation for the enormous amount of care and encouragement I have received from my family.

Table of Contents

List of Figures

List of Tables

Chapter 1

Introduction

This chapter starts with the general motivation and objectives related to the modeling and simulation of power converter systems. This general demonstration of the importance of the matter is followed by a short description of different common methods for modeling and simulation of the power converter system, such as conventional average models, detailed switching models, dynamic phasor models and terminal behavioral models, their pros and cons, and the application of each methodology. Additionally, the terminal behavioral model is described in detail. Finally, at the end of the chapter the thesis outline is described.

1.1 Motivation And Objectives

Penetration of distributed energy resources into the electrical grid has accelerated in previous decades because of the global increase in electricity demand, growing environmental concerns associated with the conventional form of the electrical grid, and increasing government policies. The global distributed energy generation market size was valued at 242.6 billion USD in 2019, and is expected to grow at a compound annual growth rate (CAGR) of 11.5% from 2020 to 2027 [1]. Factors such as growing environmental awareness, increasing government regulations and emission reduction targets, and the demand for energy are expected to drive the market over the forecast period. With increases in the deployment of distributed and renewable energy resources, the application of power electronics as power processing units between sources, loads and energy storage systems has also increased. Enabled by significant flexibility and controllability of power electronics units, the future power system will have much better control characteristics and overall efficiency. On the other hand, the future power system will have more complexity associated with control and operation, due to the intermittent nature of distributed and renewable energy resources and the high complexity of a grid that includes many power electronics units. Voltage and frequency deviation problems emerge more often when the reverse power flow occurs under a supply-demand imbalance in distributed power systems.

To ensure the stability and sustainability of the power grid in the future, proper simulations and modeling of large-scale interconnected power electronics units are essential; however, due to the lack of availability of detailed high fidelity models and the computational burden associated with the simulation of detailed models, simplifications of power electronics circuits in the form of average models or simplified equivalent representations of different elements of the power system are often essential to avoiding very long and impractical simulation times. Additionally, the impracticality of gathering detailed information about all of the internal elements of a complex system of interconnected power converters are also inconvenient. These challenges have been motivations for developing fundamental approaches to tackle the aforementioned problems.

1.2 Detailed Switching Models

Using detailed switching models, it is possible to observe and understand the operation of power converters at different switching stages. This model can be used to accurately observe the time domain representation of currents and voltages of the model and use this information for choosing proper components for the circuitry [2]. Detailed switching models require detailed information of the topology, circuitry, and control aspects of the power convers to represent an accurate operation of the system. Additionally, using detailed switching modeling methodology it is possible to accurately observe or estimate the voltage and currents of different elements of the system during the switching cycle, enabling capabilities for the designing of components or evaluating the shortcomings of the design by observing the time domain representation of voltage and currents. If detailed information about different aspects of the power converters, such as circuit, control and operational conditions are available, then this modeling method can be developed to study the characteristics of these systems. Additionally, the simulating run time required is usually high as a result of the computational burden associated with this modeling method. This factor limits the application of this methodology to small models, such as one or a small number of interconnected power converters since modeling large combination of interconnected power converts would be impractically time consuming. These main limitations associated with this methodology are important limiting factors, as well as incentive for exploring other modeling solutions.

1.3 Average Models

Average models are widely used in the field of power electronics. Utilization and adoption of average models for power converters were first proposed by Wester and Middlebrook [3] By averaging over the duty cycle it is possible to develop models that, in comparison to the detailed switching model, are much more computationally efficient, at the cost of lower details, although they are still suitable for many of the modeling and control requirements in the design and operation stage. Resulting models from this methodology neglect the switching action while representing a continuous model that still represents the nonlinear control dynamics of the converters. Unlike the detailed switching models, the timestep associated with computerized simulated models resulting from this methodology can be much larger than the switching cycle, resulting in faster simulations achieved with this method. While the simplicity associated with this method makes it applicable for modeling systems of interconnected power converters, the lack of representation of the switching action and the resulting harmonics could potentially result in unwanted harmonic interactions in the real implementation of the power converters.[4] Observing harmonic interactions resulting from the switching action and PWM modulators of different interconnected converters are an example that reveals the insufficient solution that this method represents in applications that require high degree of accuracy and reliability.

1.4 Dynamic Phasor Models

Dynamic phasor model, also known as generalized state space models, is a modeling method that represents the model of the system in the time-frequency domain [5]. This modeling method can represent the switching harmonics accurately however it is still more computationally efficient in comparison to the detailed switching model [4]. In comparison to the conventional average models, this model can also show the harmonic interactions between the interconnected power converters, resulting in more realistic model of the system [6]. Taking multiple pre-assumptions into account, by using this methodology, it has been possible to observe harmonic iteration instability instances that are observable with detailed switching models, but the conventional average models cannot

show [4], [6]. While providing proper solutions to some of the challenges of modeling and simulation, this method still has some limitations. The computational efficiency associated with this modeling method is dependent of the number of harmonics included in the model. Additionally, in the case of unstable cases that are discoverable with this method, intuitive insights for the selection of combination of harmonics required for study of occurrence of the unstable case are still to be discovered. The need for detailed information about the components, topology, circuitry and control aspects of the system are also another limiting factor for developing models based on this methodology. The advantages and disadvantages of this methodology are more or less observed in other related frequency modeling methods such as Harmonic State Space model [7].

1.5 Terminal Behavioral Models

Detailed information about the components, topology, circuitry, and control aspects of systems are not always easily achievable, thus modeling and simulation of systems experiences an important challenge that need to be addressed. A two-port electrical equivalent model of the DC power converters has been developed steadily since the 1970s through the work represented by Middlebrook [8]. This proposed approach has been a very convenient methodology to model the complex dynamic systems that involve multiple interconnected power converters. Dynamic interactions between the various interconnected power converters in the load and source can result in well-known oscillations and instability modes in the systems that have power electronics units integrated inside them [9], [10]. Individual power converters that comprise a complex system can be individually modeled and simulated using the two-port network and as a result, modeling and simulation of the complex system of interconnected power converters can be compartmentalized, resulting in facilitation of known small-signal stability assessment methodologies to assure the overall stability of the combined complex system. [10]–[12], As a result, controller design as well as some component design constraints can be incorporated to tackle the stability requirements of the system. Details of the controller structure and values, as well as topology and detailed information of the power converters are usually not shared by manufacturers to satisfy the intellectual property protection policies However, when using the two-port modeling method it is possible to estimate the

necessary behavioral model of the power converters to perform proper stability assessment of the system without the need for detailed information about the internal circuitry or control design of the power converter. Two-port networks have been widely used in power electronics in a variety of applications, such as simulations related to the spacecraft power system [13], characterization of the nonlinear components of the power electronics circuit such as PWM modulator [14], modeling and simulation of DC-DC converters, modeling active rectifiers [15], [16] and designing resonant converters [17], [18] and piezoelectric circuits [19]. Furthermore, the issues related to the electromagnetic interference have also been a topic of focus related to this modeling method by representing the circuitry in a two port or one port fashion. These models are represented by one-port or two-port networks [20], [21]. It is important to observe that the application of one-port networks-based models is constrained because the load or source of the object of the modeling turns out to be part of the model. Therefore, the model is restricted to be used for that particular load or source. The application of network models with more than one port allows for decoupling the effects of the dynamics of what is supplying and loading the model. This possibility is explored and elaborated in the case of PM machines in this paper. The representation of three-phase AC converters with synchronous *d-q* reference frames was formalized in [22] This kind of modeling makes it easy to linearize the converters because the operation points in a steady state are constant values. However, a multiple-input and multiple-output (MIMO) impedance matrix is formed in *dq*-frame. The matrix is composed of single-input, single-output transfer functions and the stability of three-phase converters must be inferred by the generalized Nyquist criterion. This work propelled research regarding the modeling of the converters in these frames and provided new tools for accessing the stability of power electronics systems [23]–[26]. The alternative for linearizing the converter, represented in AC sequence components, is with the technique known as harmonic linearization [27]. Permanent magnetic synchronous machines (PMSM) are electromechanical devices of increasing relevance nowadays. Due to their high torque density, efficiency, and controllability for a broad range of speeds, PMSMs are gaining market share in applications such as electric vehicles [28], traction systems, and robotics [29] The stability issues of these machines related to their electrical ports have been tackled in the literature. Work represented in [30], suggested to use impedance analysis to investigate the problem of sub-

synchronous electrical oscillations caused by the interaction of wind farms and the power grid through a dc-link. However, the authors do not provide any procedure for modeling the PMSM as a Thevenin equivalent. The issue of oscillations in the PMSM mechanical drive is well-reported in the literature [31], [32]. However, the models are either a complete set of nonlinear equations or linearized in a state-space form, which is not convenient to apply to the impedance analysis and requires detailed knowledge of the components of system. This thesis proposes to model the PMSM with a three-port network circuit. Two of these ports refer to the electrical connection of the machine in *d-q* channels. The third one is related to the rotor connection with the mechanical load. The model is composed of a set of nine transfer functions relating the *d* and *q* voltages and currents of the electrical ports with the torque and speed of the mechanical port. This model is obtained through sweeping sinusoidal perturbations on the machine ports. However, the transfer function obtained through these perturbations includes the dynamics of the electrical source and mechanical load of the PMSM operating as a motor. These dynamics must be decoupled from the final three-port network model. Toward this end, an extension of the work discussed in [11] where the model is obtained by the product of two matrices is proposed. The first matrix is composed of elements of the measured transfer functions. The second is also composed of measured transfer functions and serves as a linear transformation to decouple the source and load port's influence on the first matrix [33] . To extend the cited work, we define a mechanical impedance as the ratio of the torque over the rotor speed. The voltage perturbation signals on the PMSM electrical *d-q* ports are driven by a vector control technique based on the flux orientation principle [34]. This drive system is a standard option to control the machines because it has a better dynamic response than scalar drive approaches. Furthermore, its references are defined in the *d-q* reference frame as it is the PMSM network model for its electrical ports. A mechanically coupled induction machine is used to impose the perturbation torque signal on the rotor's shaft.

1.6 Terminal Behavioral Models for Electrical Machines

The application of permanent magnet synchronous machines (PMSM) has been growing due to their high-power density and torque characteristics that make them a

compact solution to a wide variety of applications, such as wind farms, electrical vehicles, ship propulsion systems, and aircrafts [35]–[37]. Proper integration of this electro-mechanical component to the system requires detailed and high-fidelity models that represent the electrical and mechanical characteristics of the machine accurately. Without having such models of the machine and applying proper stability assessment techniques to the system, its reliability and sustainability of the operation of such systems would be questionable. To tackle this matter, this thesis proposes adopting the so-called terminal behavioral modeling method to electrical machines and, for the first time, experimentally verify this matter by developing a characterization test bed capable of controlling the machine, operating the machine at the operating point of interest, and measuring various electrical and mechanically related frequency responses from the source and load terminals. The unterminated model of the machine is developed by representing the machine as a three-port linear network in which two of the ports are related to the electrical connections and the third describes the mechanical connection of the machine to the shaft coupler. The electrical ports are described in the synchronous *d-q* reference frame, and the mechanical one is featured in the form of a mechanical impedance. Using the decoupling procedure related to the TBM modeling study, it is possible to decouple the dynamics of the electrical connection, such as the dynamics of the current and speed controller, as well as the mechanical dynamics coupled through the mechanical shaft of the machine.

1.7 Thesis Outline

This thesis includes various topics related to the application of a modeling methodology for high fidelity emulation of permanent magnet synchronous machines. Detailed background study, mathematical derivation, simulation results, and hardware verification of the methodology are represented throughout the chapters of this thesis.

Chapter 1 provides a more general survey of different modeling and simulation approaches that are common for modeling of various electrical systems and advantages and disadvantages that are associated with each molding method. survey of the published work around two-port network models of power converters and the terminal behavioral

modeling method are then discussed in details. Their necessity, application, and a summary of the results and comparisons that are already established using this modeling methodology are also discussed in this chapter.

Chapter 2 presents the conventional dynamic modeling method for permanent magnet machines as well as details related to controller design strategy and time domain simulations of the resulting model. Additionally, since the mechanical torque on the shaft is being imposed using an induction machine, the dynamic mode of induction machine is also presented in this chapter. The state-space model and small signal model of PM machines is also developed is this chapter. These representations are then used in next chapter to demonstrate the capabilities of the TBM decoupling procedure in decoupling the source and load dynamics.

Chapter 3 represents the application of TBM modeling methodology to permanent magnet synchronous machines. In this chapter, the details of required frequency response measurements that are necessary for obtaining the TBM model of the machine, as well as details of the decoupling procedure are presented in details. Mathematical explanation of the decoupling method is first presented and then followed by simulation results. For preparing the simulation result, the dynamic model of permanent magnet machine is used and the model of induction machine is also used to provide the torque perturbations.

Chapter 4 represents the hardware implementation aspect and real case experiments related to this modeling method. Introduction of Hardware-In-The-Loop (HIL) and Power-Hardware-In-The-Loop (PHIL), frequency response analyzer, and various other implementation challenges are elaborated on in this section. Additionally, the characterization of the mechanical shaft interface is also discussed in detail in this section. Finally, this chapter includes the comparison of the resulting TBM model and time domain response acquired from the experimental test setup to verify the model.

Chapter 5 includes summaries of the results achieved through this thesis including the advantages and disadvantages of real case implementation and challenges related to the experimental implementation of the system. Additionally, this chapter presents insights for future research plans related to this work.

Chapter 2

Introduction

Permanent magnet synchronous machines provide superior power density and torque characteristics in comparison to other types of electrical machines. These characteristics are the reason for the implementation of such machines in wide variety of applications such as EV industry. Various car manufacturers use this type of the machine for the purpose of traction and with ever-increasing trends in application of electrical vehicles, the overall instances of using this kind of machines are an increasing trend. Usage of this type of machines in electrical appliances in residential and commercial domains are also increasing. Main focus of this chapter is developing the dynamic model of machines and control to prepare the requirements needed for terminal behavioral modeling study.

2.1 Different Types of PM Machines

Different types of PM machines have been developed relevant to different applications. The main categories of the permanent magnet machines include slot-less stator, slotted stator, radial flux, or axial flux type. Additionally, locations of the permanent magnets on the rotor could be different to form different types of machines. These magnets could be installed on the surface of the rotor or integrated inside the rotor core sheets. In the case of surface-mounted magnets, the d and q axes inductances are very close to each other since the permeability of the magnetic material is very close to the permeability of the air. The type of machine used in the experimental implementation section of this thesis, is the surface mount type of PM machine. Different design considerations such as geometry, material and various simulations and analysis are taken into account for developing these types of machines [38].

2.2 Modeling of Permanent Magnet Synchronous Motor

In this section, a conventional dynamic mode of PMSM is represented. Equations that describe the terminal voltage of the motor in *abc* frame can be written as Eqn. (2.1)

where v_{abc} is the terminal voltage of the stator winding, i_{abc} is the stator winding current, $\lambda_{abc}$are the total flux linkage. λ_{abcm} represents the permanent magnet flux linkage and R_s is the stator winding resistance.

$$\underbrace{\begin{bmatrix} v_a \\ v_b \\ v_c \end{bmatrix}}_{\text{Vabc}} = \underbrace{\begin{bmatrix} R_s & 0 & 0 \\ 0 & R_s & 0 \\ 0 & 0 & R_s \end{bmatrix}}_{\text{Stator Resistance Matrix}} \underbrace{\begin{bmatrix} i_a \\ i_b \\ i_c \end{bmatrix}}_{\text{iabc}} + \frac{d}{dt} \underbrace{\begin{bmatrix} \lambda_a \\ \lambda_b \\ \lambda_c \end{bmatrix}}_{\lambda\text{abc}} \tag{2.1}$$

$$\begin{bmatrix} \lambda_a \\ \lambda_b \\ \lambda_c \end{bmatrix} = \underbrace{\begin{bmatrix} L_{aa} & L_{ab} & L_{ac} \\ L_{ba} & L_{bb} & L_{bc} \\ L_{ca} & L_{cb} & L_{cc} \end{bmatrix}}_{\text{Inductance Matrix}} \begin{bmatrix} i_a \\ i_b \\ i_c \end{bmatrix} + \underbrace{\begin{bmatrix} \lambda_{am} \\ \lambda_{bm} \\ \lambda_{cm} \end{bmatrix}}_{\lambda_{abcm}} \tag{2.2}$$

L_{aa}, L_{bb} and L_{cc} represent the self-inductances while other components of the inductance matrix represent the mutual inductances as it is shown in Eqn. (2.3) -(2-9).

$$L_{ab} = L_{ba} = -M_s - L_m \cos\left(2\left(\theta_e + \frac{\pi}{6}\right)\right) \tag{2.3}$$

$$L_{bc} = L_{cb} = -M_s - L_m \cos\left(2\left(\theta_e + \frac{\pi}{6} - \frac{2\pi}{3}\right)\right) \tag{2.4}$$

$$L_{ca} = L_{ac} = -M_s - L_m \cos\left(2\left(\theta_e + \frac{\pi}{6} + \frac{2\pi}{3}\right)\right) \tag{2.5}$$

$$L_{aa} = L_s + L_m \cos 2\theta_e \tag{2.6}$$

$$L_{bb} = L_s + L_m \cos\left(2(\theta_e - 2\pi/3)\right) \tag{2.7}$$

$$L_{cc} = L_s + L_m \cos\left(2(\theta_e + 2\pi/3)\right) \tag{2.8}$$

$$\begin{bmatrix} \lambda_{am} \\ \lambda_{bm} \\ \lambda_{cm} \end{bmatrix} = \begin{bmatrix} \lambda_m \cos\ \theta_e \\ \lambda_m \cos\left(\theta_e - 2\pi/3\right) \\ \lambda_m \cos\left(\theta_e + 2\pi/3\right) \end{bmatrix} \tag{2.9}$$

Equation (2.10) and (2.11) shows the Park-Clarke transformation and inverse Park-Clarke transformation. Using this transformation, it is possible form *d-q* representation of the variables which is then used to intuitively control and operate the machine.

$$x_{dq0} = \sqrt{\frac{2}{3}} \begin{bmatrix} cos(\theta) & cos\left(\theta - \frac{2\pi}{3}\right) & cos\left(\theta + \frac{2\pi}{3}\right) \\ -sin(\theta) & -sin\left(\theta - \frac{2\pi}{3}\right) & -sin\left(\theta + \frac{2\pi}{3}\right) \\ \sqrt{\frac{1}{2}} & \sqrt{\frac{1}{2}} & \sqrt{\frac{1}{2}} \end{bmatrix} \begin{bmatrix} a \\ b \\ c \end{bmatrix} \tag{2.10}$$

$$x_{abc} = \sqrt{\frac{2}{3}} \begin{bmatrix} cos\,(\theta) & -sin\,(\theta) & \sqrt{\frac{1}{2}} \\ cos\,\left(\theta - \frac{2\pi}{3}\right) & -sin\,\left(\theta - \frac{2\pi}{3}\right) & \sqrt{\frac{1}{2}} \\ cos\,\left(\theta + \frac{2\pi}{3}\right) & -sin\,\left(\theta + \frac{2\pi}{3}\right) & \sqrt{\frac{1}{2}} \end{bmatrix} \begin{bmatrix} d \\ q \\ 0 \end{bmatrix} \tag{2.11}$$

Applying Park's transformation to the equation above, the *dq* model can be obtained. The d axis is aligned with the magnetic flux, and the q axis is aligned with the torque. Therefore, the motor model in the d-q frame can be written as Eqn. (2.12)- (2.14).

$$v_d = R_s i_d + L_d \frac{di_d}{dt} - N\omega i_q L_q \tag{2.12}$$

$$v_q = R_s i_q + L_q \frac{di_q}{dt} + N\omega(i_d L_d + \psi_m) \tag{2.13}$$

$$T_e = \frac{3}{2} N\big(i_q(i_d L_d + \psi_m) - i_d i_q L_q\big) \tag{2.14}$$

The equation that relates the electrical torque, load torque, bearing friction and speed of the rotor is then defined as Eqn. (2.13).

$$T_e = T_L + B\omega_m + J\frac{d\omega_m}{dt} \tag{2.15}$$

T_e and T_l represent the mechanical torque generated by the motor and load torque. B represents the mechanical friction. ω_m represents the rotational speed of the rotor and J represents the inertia. Using above equations, the dynamic model of the PMSM can be developed. This model is then used to develop Terminal Behavioral Model (TBM) and

validate the results. Fig. 2.1 shows the Simulink model which is representing the same equations that were discussed in part 2.2.

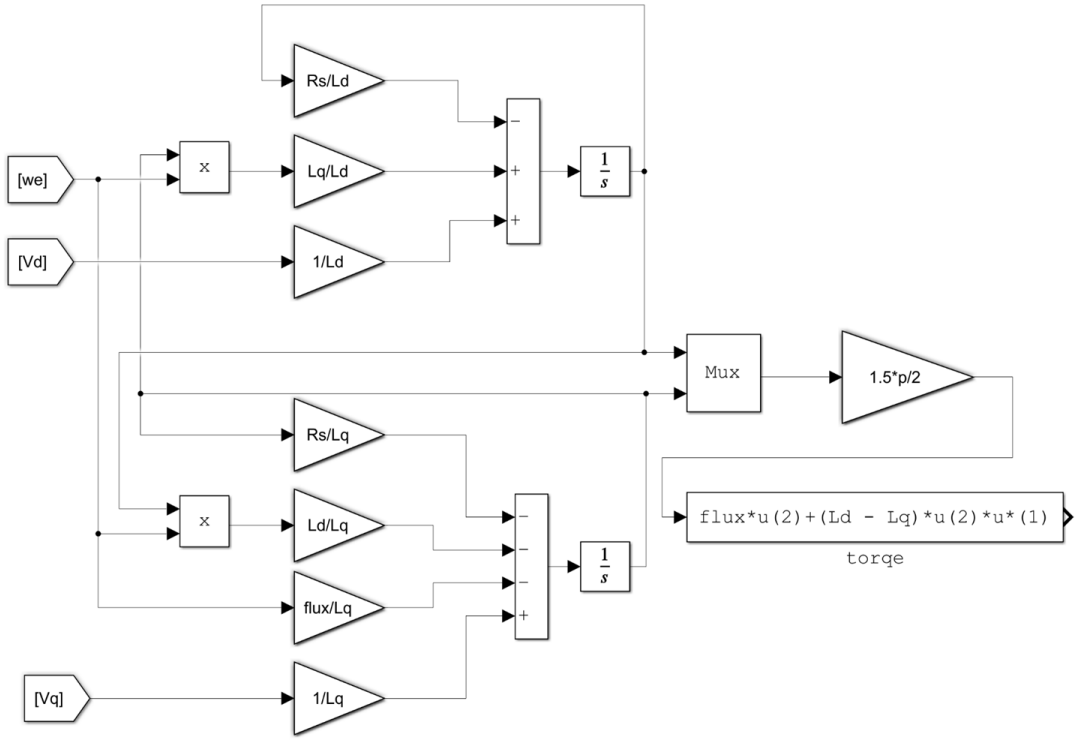

Figure 2.1: PMSM Conventional Dynamic Model (CMD) in Simulink

This conventional dynamic model is used to implement the Terminal Behavioral Modeling method and validate the mathematical derivation for decoupling the dynamics of the load and source. This model is a nonlinear model however as it is demonstrated later in this thesis, it is possible to use the linearized representation of this model at the operating point of interest to develop the required frequency responses needed for TBM study.

2.3 State Space Model of PMSM

As it was shown in the previous part, equations of the PMSM can be described in d-q coordinates (2.14)- (2.16). As we can see in this representation, we have multiplication of the state variables. In the case that we want to develop the state space representation of the PMSM we need to write the linearized form of this equations.

$$\frac{di_d}{dt} = -\frac{R_s}{L_d} i_d + \frac{L_q p}{L_d} \omega i_q + \frac{1}{L_d} u_d \tag{2.16}$$

$$\frac{di_q}{dt} = -\frac{R_s}{L_q} i_q - \frac{L_d p}{L_q} \omega i_d - \frac{p\psi_f}{L_q} \omega + \frac{1}{L_q} u_q \tag{2.17}$$

$$\frac{d\omega}{dt} = \frac{1}{J}\left[\frac{3p}{2}\left(\psi_f i_q + \left(L_d - L_q\right) i_d i_q\right) - T_F - T_L\right] \tag{2.18}$$

In these equations i_d , i_q , u_d and u_q represent the current and voltage of the stator in d and q axis. L_d and L_q represent the d and q axis inductances. ω represents the rotational speed and T_L and T_F represent the load torque and friction torque. p represents the number of poles and R_s represent the stator resistance. Using Taylor series, a function can be approximated at a specific point using Eqn. (2.17).

$$\vec{f}(\vec{x},\vec{u}) = \vec{f}(\vec{x}_0,\vec{u}_0) + \frac{\partial \vec{f}(\vec{x}_0,\vec{u}_0)}{\partial \vec{x}} \cdot (\vec{x} - \vec{x}_0) + \frac{\partial \vec{f}(\vec{x}_0,\vec{u}_0)}{\partial \vec{u}} \cdot (\vec{u} - \vec{u}_0) + \frac{1}{2!}\left[\frac{\partial^2 \vec{f}(\vec{x}_0,\vec{u}_0)}{\partial \vec{x}^2} \cdot (\vec{x} - \vec{x}_0)^2 + 2\frac{\partial^2 \vec{f}(\vec{x}_0,\vec{u}_0)}{\partial \vec{x}\partial \vec{u}} \cdot (\vec{x} - \vec{x}_0)(\vec{u} - \vec{u}_0) + \frac{\partial^2 \vec{f}(\vec{x}_0,\vec{u}_0)}{\partial \vec{u}^2} \cdot (\vec{u} - \vec{u}_0)^2\right] \tag{2.17}$$

By using the first three terms of the Taylor series we can approximate the multiplication form that appear in Eqn. (2.14)- (2.16) as the Eqn. (2.18)- (2.20).

$$\omega i_q \approx \omega_0 i_{q0} + \omega_0\left(i_q - i_{q0}\right) + i_{q0}(\omega - \omega_0) \tag{2.18}$$

$$\omega i_d \approx \omega_0 i_{d0} + \omega_0(i_d - i_{d0}) + i_{d0}(\omega - \omega_0) \tag{2.19}$$

$$i_d i_q \approx i_{d0} i_{q0} + i_{d0}\left(i_q - i_{q0}\right) + i_{q0}(i_d - i_{d0}) \tag{2.20}$$

By substituting the linearized form of the multiplication to the original equations, we can achieve the linearized equations at specific operating point as Eqn. (2.21)- (2.23) show.

(2.21)

$$\frac{di_d}{dt} = -\frac{R_s}{L_d} i_d + \frac{L_q p}{L_d} \omega_0 i_{q0} + \frac{L_q p}{L_d} \omega_0 (i_q - i_{q0}) + \frac{L_q p}{L_d} i_{q0} (\omega - \omega_0) + \frac{1}{L_d} u_d$$

(2.22)

$$\frac{di_q}{dt} = -\frac{R_s}{L_q} i_q - \frac{L_d p}{L_q} \omega_0 i_{d0} + -\frac{L_d p}{L_q} \omega_0 (i_d - i_{d0}) - \frac{L_d p}{L_q} i_{d0} (\omega - \omega_0) - \frac{p\psi_f}{L_q} \omega + \frac{1}{L_q} u_q$$

(2.23)

$$\frac{d\omega}{dt} = \frac{1}{J}\left[\frac{3p}{2}\left(\psi_f i_q + \left(L_d - L_q\right) i_{d0} i_{q0} + \left(L_d - L_q\right) i_{d0}\left(i_q - i_{q0}\right) + \left(L_d - L_q\right) i_{q0}\left(i_d - i_{d0}\right)\right) - B\omega - T_L\right]$$

In this equation friction torque is approximated with a constant *B* multiplied by the angular speed. The resulting equations can be used to form the standard form of state space model as Eqn. (2.24).

$$\begin{bmatrix} \frac{di_d}{dt} \\ \frac{di_q}{dt} \\ \frac{d\omega_m}{dt} \end{bmatrix} = \begin{bmatrix} -\frac{R_s}{L_d} & \frac{L_q p}{L_d}\omega_0 & \frac{L_q p}{L_d} i_{q0} \\ -\frac{L_d p}{L_q}\omega_0 & -\frac{R_s}{L_q} & -\frac{L_d p}{L_q} i_{d0} - \frac{p\psi_f}{L_q} \\ \frac{3p}{2J}\left(L_d - L_q\right) i_{q0} & \frac{3p}{2J}\left(\psi_f + \left(L_d - L_q\right) i_{d0}\right) & -\frac{B}{J} \end{bmatrix} \begin{bmatrix} i_d \\ i_q \\ \omega_m \end{bmatrix} + \begin{bmatrix} \frac{1}{Ld} & 0 & 0 \\ 0 & \frac{1}{Lq} & 0 \\ 0 & 0 & -\frac{1}{J} \end{bmatrix} \begin{bmatrix} v_{id} \\ v_{iq} \\ T_o \end{bmatrix} + \begin{bmatrix} -\frac{L\, q\, i_{q0} \omega_0 p}{Ld} \\ \frac{Ld i_{d0} \omega_0 p}{Lq} \\ -\frac{3p}{2J}\left(L_d - L_q\right) i_{d0} i_{q0} \end{bmatrix} \quad (2.24)$$

2.4 Small Signal Model of PMSM

In this section small signal model of the PM machine is also developed and compared with the state space model. This model is based on the characteristics of the machine including the internal parameters and the operation point of the machine but it does not reflect on the dynamic characteristics of the electrical source or mechanical load connected to the machine. By representing each state variable as the operating point steady state and small perturbation we can represent the variables as Eqn. (2.25).

$$x = X + \tilde{x} \tag{2.25}$$

In equation above, X is steady state value at a considered operating point and $\tilde{x}$ shows the small-signal perturbation. Table 2.1 shows all the state variables in the form of small signal and operating point steady state value. i_d, i_q, v_d and v_q are the current and voltage in d and q axis. ω and t represent the speed and torque. I_d, I_q, V_d, V_q, T and W represent the operating point while ,$\tilde{\imath}_d, \tilde{\imath}_q$, $\tilde{v}_d, \tilde{v}_q$, $\tilde{t}$ and $\tilde{\omega}$ represent the small signal perturbation of the previously mentioned parameters

$i_d = I_d + \tilde{\imath}_d$	$v_d = V_d + \tilde{v}_d$	$t = T + \tilde{t}$
$i_q = I_q + \tilde{\imath}_q$	$v_q = V_q + \tilde{v}_q$	$\omega = W + \tilde{\omega}$

Table 2.1: Small signal form of PMSM variables

In this section the aforementioned representation of variables is substituting the original form of variables that are presented in Eqn. (2.14)- (2.16). Eqn. (2.26)- (2.28) show substituted state variables by their small signal form.

(2.26)

$$\frac{d(I_d+\tilde{\imath}_d)}{dt} = -\frac{R_s}{L_d}(I_d + \tilde{\imath}_d) + \frac{L_q p}{L_d}(W + \tilde{\omega})(I_q + \tilde{\imath}_q) + \frac{1}{L_d}(V_d + \tilde{v}_d)$$

(2.27)

$$\frac{d(I_q+\tilde{\imath}_q)}{dt} = -\frac{R_s}{L_q}\left(I_q + \tilde{\imath}_q\right) - \frac{L_d p}{L_q}(W + \tilde{\omega})(I_d + \tilde{\imath}_d) - \frac{p\psi_f}{L_q}(W + \tilde{\omega}) + \frac{1}{L_q}\left(V_q + \tilde{v}_q\right) \tag{2.28}$$

$$\frac{d(W+\tilde{\omega})}{dt} = \frac{1}{J}\left[\frac{3p}{2}\left(\psi_f(I_q + \tilde{\imath}_q) + \left(L_d - L_q\right)(I_d + \tilde{\imath}_d)(I_q + \tilde{\imath}_q)\right) - T_L\right]$$

Following, this representation of the equations is simplified to form small signal model of PM machine as the first step equation related to the *d-axis* current can be expanded as Eqn. (2.29).

$$\frac{d(I_d + \tilde{\imath}_d)}{dt} = -\frac{R_s}{L_d}I_d - \frac{R_s}{L_d}\tilde{\imath}_d + \frac{L_q p}{L_d}WI_q + \frac{L_q p}{L_d}I_q\tilde{\omega} + \frac{L_q p}{L_d}\tilde{\imath}_q W + \frac{L_q p}{L_d}\tilde{\imath}_q\tilde{\omega} + \frac{1}{L_d}V_d + \frac{1}{L_d}\tilde{v}_d \tag{2.29}$$

Values of the steady state signal form can be removed from the both side of the equation as represented in Eqn. (2.30).

$$\cancel{\frac{d(I_d)}{dt}} + \frac{d(\tilde{\imath}_d)}{dt} = \cancel{-\frac{R_s}{L_d}I_d} - \frac{R_s}{L_d}\tilde{\imath}_d + \cancel{\frac{L_q p}{L_d}WI_q} + \frac{L_q p}{L_d}I_q\tilde{\omega} + \frac{L_q p}{L_d}\tilde{\imath}_q W + \frac{L_q p}{L_d}\tilde{\imath}_q\tilde{\omega} + \cancel{\frac{1}{L_d}V_d} + \frac{1}{L_d}\tilde{v}_d \tag{2.30}$$

Since the perturbation signal has a small value, multiplication of the two perturbation signals will be very small and can be removed from the equation as it is shown in Eqn. (2.31)

$$\frac{d(\tilde{\imath}_d)}{dt} = -\frac{R_s}{L_d}\tilde{\imath}_d + \frac{L_q p}{L_d}I_q\tilde{\omega} + \frac{L_q p}{L_d}\tilde{\imath}_q W + \frac{L_q p}{L_d}\tilde{\imath}_q\tilde{\omega} + \frac{1}{L_d}\tilde{v}_d \tag{2.31}$$

Resulting small signal equation for the *d-axis* can be shown as Eqn. (2.32).

$$\frac{d\tilde{\imath}_d}{dt} = -\frac{R_s}{L_d}\tilde{\imath}_d + \frac{L_q p}{L_d} I_q \tilde{\omega} + \frac{L_q p}{L_d}\tilde{\imath}_q W + \frac{1}{L_d}\tilde{v}_d \tag{2.32}$$

Similarly, by replacing the small signal representation of variables for q-axis current, equation related to the q-axis current can be expanded as Eqn. (2.33).

$$\frac{d(I_q + \tilde{\imath}_q)}{dt} = -\frac{R_s}{L_q}(I_q + \tilde{\imath}_q) - \frac{L_d p}{L_q}(W + \tilde{\omega})(I_d + \tilde{\imath}_d) - \frac{p\psi_f}{L_q}(W + \tilde{\omega}) + \frac{1}{L_q}(V_q + \tilde{v}_q) \tag{2.33}$$

Values of the steady state signal form can be removed from both side of the equation since the perturbation signal has a small value, also multiplication of the two perturbation signals will be very small and can be removed from the equation as it is shown in Eqn. (2.34).

$$\cancel{\frac{d(I_q)}{dt}} + \frac{d(\tilde{\imath}_q)}{dt} = \cancel{-\frac{R_s}{L_q} I_q} - \frac{R_s}{L_q}\tilde{\imath}_q - \cancel{\frac{L_d p}{L_q} W I_d} - \frac{L_d p}{L_q} I_d \tilde{\omega} - \frac{L_d p}{L_q}\tilde{\imath}_d W \cancel{- \frac{L_d p}{L_q}\tilde{\imath}_d \tilde{\omega}} \cancel{- \frac{p\psi_f}{L_q} W} - \frac{p\psi_f}{L_q}\tilde{\omega} \cancel{+ \frac{1}{L_q} V_q} + \frac{1}{L_q}\tilde{v}_q \tag{2.34}$$

Resulting small signal equation for the *q-axis* can be shown as Eqn. (2.35).

$$\frac{d\tilde{\imath}_q}{dt} = -\frac{R_s}{L_q}\tilde{\imath}_q - \frac{L_d p}{L_q} I_d \tilde{\omega} - \frac{L_d p}{L_q}\tilde{\imath}_d W - \frac{p\psi_f}{L_q}\tilde{\omega} + \frac{1}{L_q}\tilde{v}_q \tag{2.35}$$

Similarly, this derivation can be developed for the equation that represent the speed of the machine. Equation related to the speed can be also expanded as Eqn. (2.36).

$$\frac{d(W+\tilde{\omega})}{dt} = \frac{1}{J}\left[\frac{3p}{2}\left(\psi_f(I_q+\tilde{\imath}_q)+\left(L_d-L_q\right)(I_dI_q+\tilde{\imath}_dI_q + I_d\tilde{\imath}_q+\tilde{\imath}_d\tilde{\imath}_q)\right)-BW-B\tilde{\omega}-T-\tilde{t}\right] \tag{2.36}$$

Values of the steady state signal form can be removed from both side of this equation as it is shown in Eqn. (2.37).

$$\cancel{\frac{d(W)}{dt}}+\frac{d(\tilde{\omega})}{dt} = \frac{1}{J}\left[\frac{3p}{2}\left(\psi_f(I_q+\tilde{\imath}_q)+\left(L_d-L_q\right)(\cancel{I_dI_q}+\tilde{\imath}_dI_q + I_d\tilde{\imath}_q+\tilde{\imath}_d\tilde{\imath}_q)\right)-\cancel{BW}-B\tilde{\omega}\cancel{-T}-\tilde{t}\right] \tag{2.37}$$

Since the perturbation signal has a small value, multiplication of the two perturbation signals will be very small and can be removed from the equation. Resulting small signal equation for the speed can be shown as Eqn. (2.38).

$$\frac{d(\tilde{\omega})}{dt} = \frac{1}{J}\left[\frac{3p}{2}\left(\psi_f(\tilde{\imath}_q)+\left(L_d-L_q\right)(\tilde{\imath}_dI_q+I_d\tilde{\imath}_q)\right)-B\tilde{\omega}-\tilde{t}\right] \tag{2.38}$$

Resulting small signal equations are summarized in to from a matrix form. This equation set can be shown in the matrix form (2.39) to make it easier to be compared with the state space model.

$$\begin{bmatrix} \frac{d\tilde{\imath}_d}{dt} \\ \frac{d\tilde{\imath}_q}{dt} \\ \frac{d\tilde{\omega}}{dt} \end{bmatrix} = \begin{bmatrix} -\frac{R_s}{L_d} & \frac{L_q p}{L_d} W & \frac{L_q p}{L_d} I_q \\ -\frac{L_d p}{L_q} W & -\frac{R_s}{L_q} & -\frac{L_d p}{L_q} I_d - \frac{p\psi_f}{L_q} \\ \frac{3p}{2J}(L_d - L_q) I_q & \frac{3p}{2J}(\psi_f + (L_d - L_q) I_d) & -\frac{B}{J} \end{bmatrix} \begin{bmatrix} \tilde{\imath}_d \\ \tilde{\imath}_q \\ \tilde{\omega} \end{bmatrix} + \begin{bmatrix} \frac{1}{Ld} & 0 & 0 \\ 0 & \frac{1}{Lq} & 0 \\ 0 & 0 & -\frac{1}{J} \end{bmatrix} \begin{bmatrix} \tilde{v}_d \\ \tilde{v}_q \\ \tilde{t} \end{bmatrix} \tag{2.39}$$

It can be seen that the matrix of small signal equations is identical to the state space model in A and B matrix, however, in the small signal model the values of the operating point for the state variables are removed from both sides of the equations. By looking at the developed small signal model and state space model represent, it is clear that this model relies on the internal parameters of the machine as well as the operating point condition of the machine. This is a very important aspect of the developed model since it shows that the dynamics observed from such model can be different at non-similar operating point condition. In fact, as it is demonstrated in chapter 3, in order to compare the results of TBM modeling method with linearized models such as state space model, it is necessary to perform the TBM frequency response calculations and state space linearization at the same operating point otherwise different dynamics are expected to be observed.

2.5 Modeling of Induction Machine

Induction machines are the majority type of machines used in low power applications in the industries. Simplicity of operation and robust structure as well as simpler production process are the reasons for wide application of this type of machine. Different types of induction machines are developed for different applications. Induction machines are usually divided into two different categories on the basis of the rotor structure. Majority of the induction machines used in the industry are the type of squirrel cage. Conductive rotor bars are made of injected aluminum casting which provides both electrical paths required for the motor operation as well as holding the structural integrity

of the rotor. Wound rotor is another type of induction machines which is usually used for higher power applications. In the case of wound rotor, it is possible to change the resistance of the rotor circuit which is used to increase the startup torque in case the machine is operated without a variable frequency drive. Modeling and simulation of the induction machine is essential in this thesis since it plays the role of the mechanical load for the permanent magnet machine. The necessity of having the model and control for this machine is the motivation for detailed description of the models related to this type of machine. Models of the induction machine have been thoroughly studied in past surveys. In this thesis a simple model of the induction machine known as the dynamic model of the machine is represented. This model describes the induction machine with a limited number of equations that are required for a simple representation of the machine. Equations related to a three-phase induction machine can be represented as Eqn. (2.40)-(2.41).

$$v_{abcs} = r_s i_{abcs} + s\lambda_{abcs} \tag{2.40}$$

$$v_{abcr} = r_r i_{abcr} + s\lambda_{abcr} \tag{2.41}$$

v_{abcs} and v_{abcr} represent the matrixes of the three voltages of the stator and the rotor of the machine. In the case of squirl cage induction machine, the voltage on the rotor of the machine is zero since the rotor bars are shorted at the rotor structure. Also r_s and r_r represent the resistances of the stator and rotor in each phase. λ_{abcs} and λ_{abcr} represent the matrixes of the flux linkage for the stator and the rotor of the machine. s is associated with the derivation of the term. λ_{abcs} and λ_{abcr} can be represented in detailed form as Eqn. (2.42).

$$\begin{bmatrix} \lambda_{abcs} \\ \lambda_{abcr} \end{bmatrix} = \begin{bmatrix} L_s & L_{sr} \\ L_{sr}T & L_r \end{bmatrix} \begin{bmatrix} i_{abcs} \\ i_{abcr} \end{bmatrix} \tag{2.42}$$

Inductances represented in the Eqn. (2.42) can be shown in details in the form of Eqn. (2.43)- (2.45).

$$L_s = \begin{bmatrix} L_{ls} + L_{ms} & -\frac{1}{2}L_{ms} & -\frac{1}{2}L_{ms} \\ -\frac{1}{2}L_{ms} & L_{ls} + L_{ms} & -\frac{1}{2}L_{ms} \\ -\frac{1}{2}L_{ms} & -\frac{1}{2}L_{ms} & L_{ls} + L_{ms} \end{bmatrix} \quad (2.43)$$

$$L_{\boldsymbol{r}} = \begin{bmatrix} L_{lr} + L_{mr} & -\frac{1}{2}L_{mr} & -\frac{1}{2}L_{mr} \\ -\frac{1}{2}L_{mr} & L_{lr} + L_{mr} & -\frac{1}{2}L_{mr} \\ -\frac{1}{2}L_{mr} & -\frac{1}{2}L_{mr} & L_{lr} + L_{mr} \end{bmatrix} \quad (2.44)$$

$$L_{sr} = L_{sr}\begin{bmatrix} cos\,(\theta_r) & cos\left(\theta_r + \frac{2\pi}{3}\right) & cos\left(\theta_r - \frac{2\pi}{3}\right) \\ cos\left(\theta_r - \frac{2\pi}{3}\right) & cos\,(\theta_r) & cos\left(\theta_r + \frac{2\pi}{3}\right) \\ cos\left(\theta_r + \frac{2\pi}{3}\right) & cos\left(\theta_r - \frac{2\pi}{3}\right) & cos\,(\theta_r) \end{bmatrix} \quad (2.45)$$

In the equations, leakage magnetizing inductance of the rotor is represented as Eqn. (2.45) while leakage inductance of the stator is represented as Eqn. (2.44). Similar to the effort that was represented in the previous part for preparing the equations of the machine in the arbitrary reference frame, same derivation is represented in this section. By applying the Park-Clarke transformation to the original equations of the machine it is possible to represent the machine in the standard DQ representation. Using this transformation, equations of the machine are transformed to the stationary form as it is presented in Eqn. (2.46)- (2.49).

(2.46)

$$V_{ds} = R_s i_{ds} - \omega\left[L_{ss} i_{q_s} + L_m i_{q_r}\right] + L_{ss}\frac{d(i_{ds})}{dt} + L_m\frac{d(i_{dr})}{dt}$$

(2.47)

$$V_{qs} = R_s i_{qs} + \omega\left[L_{ss} i_{d_s} + L_m i_{d_r}\right] + L_{ss}\frac{d(i_{qs})}{dt} + L_m\frac{d(i_{qr})}{dt}$$

(2.48)

$$V_{dr} = R_r i_{dr} - (\omega - \omega_r)\left[L_{rr} i_{q_r} + L_m i_{q_s}\right] + L_{rr} \frac{d(i_{dr})}{dt} + L_m \frac{d(i_{ds})}{dt}$$

$$V_{q_r} = R_r i_{qr} + (\omega - \omega_r)\left[L_{rr} i_{d_r} + L_m i_{d_s}\right] + L_{rr} \frac{diqr}{dt} + L_m \frac{d(i_{qs})}{dt} \quad (2.49)$$

Equation related to the generated electromagnetic torque, torque on the shaft and bearing friction is also represented in Eqn. (2.50).

$$T_e = \left(\frac{3}{2}\right)\left(\frac{P}{2}\right) L_m\left(i_{qs} i_{dr} - i_{ds} i_{qr}\right) \quad (2.50)$$

$$\frac{d(\omega_m)}{dt} = \frac{1}{J}(T_e - T_m - B\omega_m) \quad (2.51)$$

In Eqn. (2.51) T_e and T_m represent the electromechanical torque generated by the motor and load torque. B represents the mechanical friction. ω_m represents the rotational speed of the rotor and J represents the inertia. Using above equations, the dynamic model of the IM can be developed in MATLAB Simulink to use as mechanical load connected to the PM machine.

2.6 Vector Control of Permanent Magnet Synchronous Machine

The motor control system applied to the Permanent Magnetic Synchronous Machine (PMSM) is created so that the machine is operated at the operating point of interest and controlled perturbations signals can be imposed on its mechanical and electrical interfaces. The final goal is to perform a dynamic characterization of the PM machine described earlier in the thesis. *d-q* control with rotor position sensing in PM machines conveniently decouples torque and flux. The direct, or d-axis, and quadrature, or q-axis, currents are controlled by the drive system. Fig. 2.3 shows the applied drive system

scheme for the PMSM machine. The block represented as Power Amplifier is representing the Power-Hardware-In-The-Loop that was used in this implementation. By providing the reference voltages in *abc* frame to the PHIL the same voltage is generated in the output terminal of the PHIL. For applying the control strategy that is represented in this thesis, having the rotor position is essential. The resolver installed on the PM machine shaft is used to estimate the position of the rotor. It generates two modulated sinusoidal waveforms that are fed to the control HIL to estimate the position and the speed of the rotor using an estimation algorithm. Details related to this block are represented in chapter 4. In this drive system, a controller controls the rotor speed through an outer loop that provides a reference for an inner control loop of the quadrature current. This current is proportional to the electromagnetic torque applied to the rotor, assuming the direct current is null. The drive is based on the Park transformation (and its inverse). The idea is taking advantage of the fact that balanced three-phase quantities can be represented by a vector spinning with a constant angular speed in a complex plane and that this vector can be decomposed into two axes spinning with the same speed.

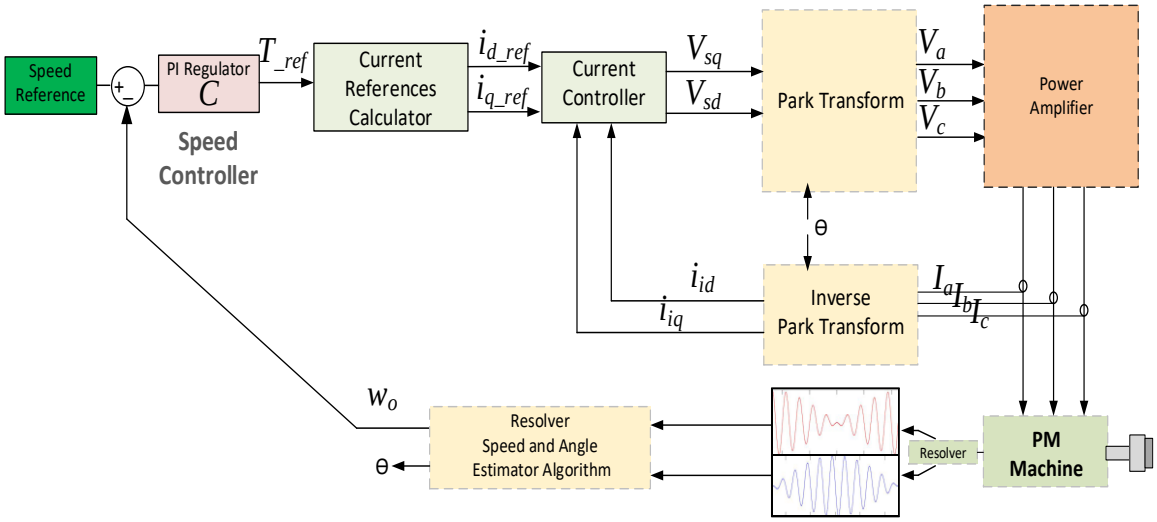

Figure 2.3: Field oriented control applied for the PMSM.

By setting the reference value for the direct component of current to be zero the torque equation related to the machine is simplified to the *q-axis* current based as it is shown in Eqn. (2.52).

$$T_e = 1.5P\left[\lambda_{pm} i_q + \left(L_d - L_q\right) i_d i_q\right] \tag{2.52}$$

where L_d and L_q are the quadrature and direct inductances. P is the number of pairs of poles and λ_{pm} is the permanent magnet flux of the machine. Fig. (2.4) shows the open form of the current controller that was previously presented in Fig (2.3). Using the decoupling strategy used in this control method, the dynamics of the *d* axis current are decoupled and the resulting torque equation is just a function of the *q-axis* current. This method simplifies the controller design significantly and makes it possible to use known control design procedures to be used for the machine as it is presented in the following parts of this chapter.

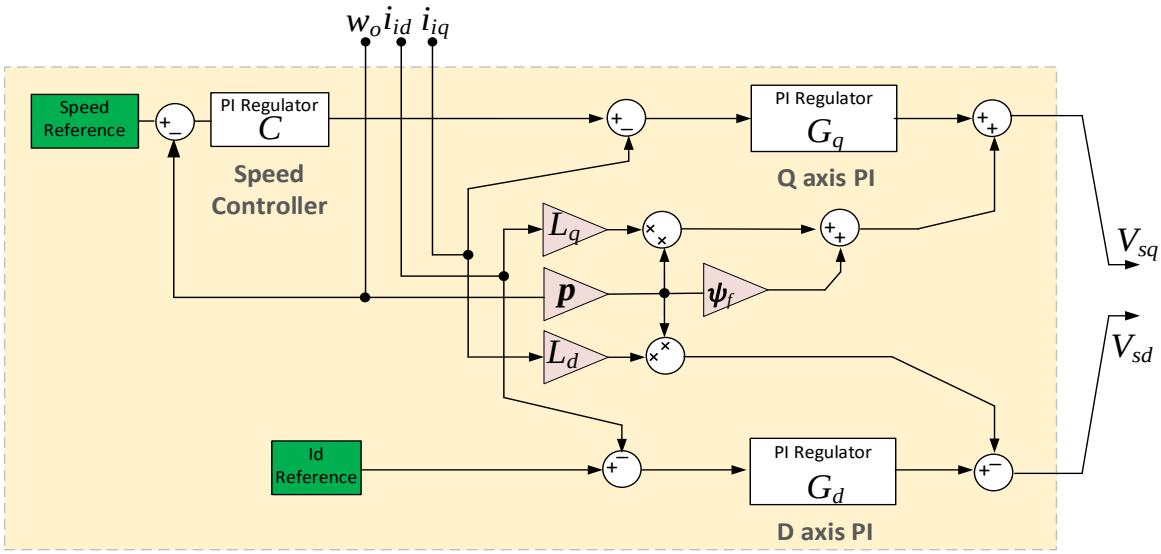

Figure 2.4: Detailed representation of the PMSM controller

For realization of the decoupled current control strategy, the details of this method are represented in Fig (2.5). This figure shows the controller decoupling terms and the PM machine as the plant that is being controlled.

As it is shown in Fig (2.5) decoupling branches that are included into the controller are selected in such a way that they can contradict the coupling branches that are shown in the PMSM model.

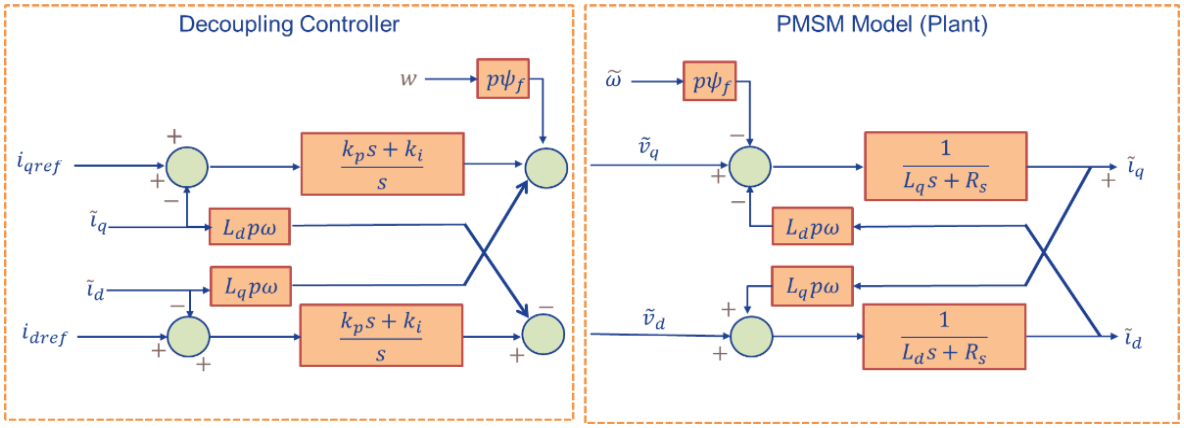

Figure 2.5: Decoupling terms and the PM machine representation

These coupling terms are representing the coupled dynamics that are inherent to the PMSM, however using the decoupling design structure it is possible to eliminate the coupling between the d and q axis dynamics. By simplifying the block diagrams represented in the Fig (2.5) it is possible to show the simplified model of the controller and the PMSM model as the it is shown in Fig. (2.6). These two representations are equivalent. As it can be seen from the simplified representation, the *d* axis and *q* axis dynamics are separated and can be controlled independently.

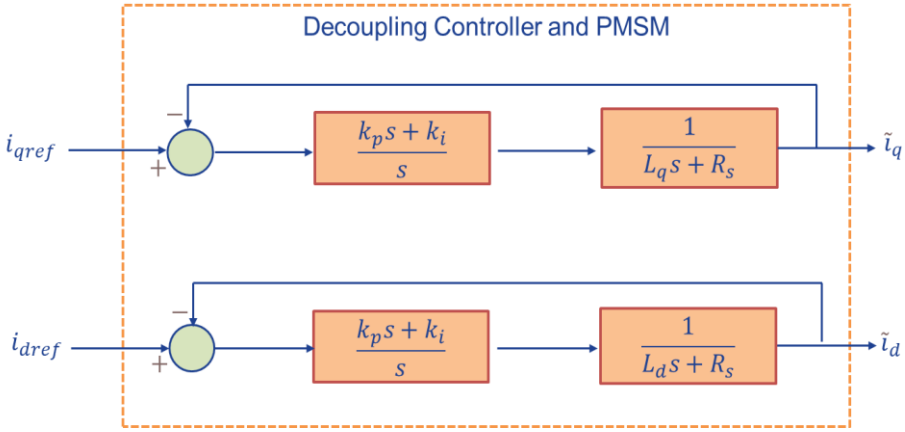

Figure 2.6: Simplified form of the current controller and PM machine

Considering the simplified block diagram to control i_q and i_q the controller is chosen to be a PI, with proportional gain of K_p and integral gain of K_i. The close-loop transfer function related to i_q and i_d in the case that $L_d = L_q = L_s$ could be calculated. By calculating the relating transfer function of d and q current to the reference current in *d and q* axis we can write Eqn. (2.53).

$$\frac{i_q}{i_{qref}} = \frac{i_d}{i_{dref}} = \frac{\frac{K_p s + K_i}{s}\frac{1}{R_s + sL_s}}{1 + \frac{K_p s + K_i}{s}\frac{1}{R_s + sL_s}} = \frac{\omega_c}{s + \omega_c} \tag{2.53}$$

As it was previously discussed on Eqn. (2.52) the generated electromagnetic torque equation related to PMSM is simplified to include just the *q* axis current in the case that the *d* and *q* inductances of the machine are equal. This is the case in the machine that is used for hardware implementation of this project. In that case the reference of the *d* axis current is set to zero and the *q* axis current is used to control the torque of the machine. Fig. 2.7 shows the block diagram related to the mechanical model of PM machine and the control representation of the *q* axis current.

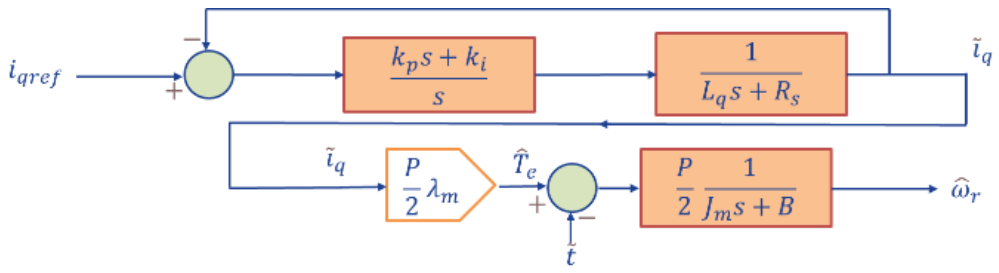

Figure 2.7: *q-axis* current to PMSM output speed

Base on Eqn. (2.53) this model can be simplified to the model represented in Fig (2.8).

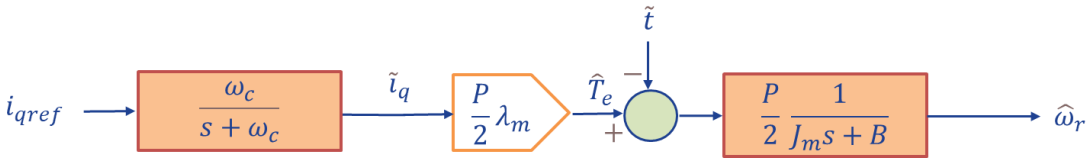

Figure 2.8: Simplified form of *q-axis* current to PMSM speed

Since the current controller is usually designed to be much faster than the mechanical dynamics off the machine, it can be assumed that the current value follows the current reference quick enough that we can assume $i_{qref} \approx i_q$. In that case the block diagram in Fig (2.8) can be more simplified to the form of block diagram shown in Fig (2.9).

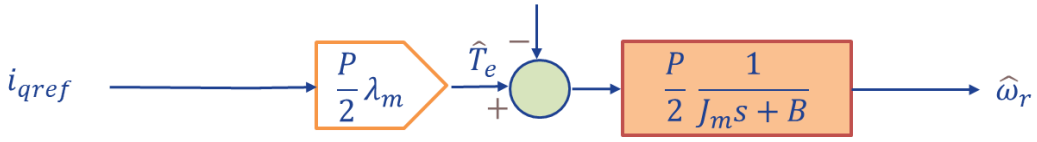

Figure 2.9: *q-axis* current to PMSM speed simplification

Using the feedback signal form, the output speed that is available from the mechanical model, it is possible to form the speed controller loop as it is presented in Fig 2.10. In addition to the speed controller a pre-compensator is also added to form the overall controller representation as Fig 2.10 where K_i and K_p are the integral and proportional gains for the PI controller used to control the rotor speed, and J_m is moment of inertia.

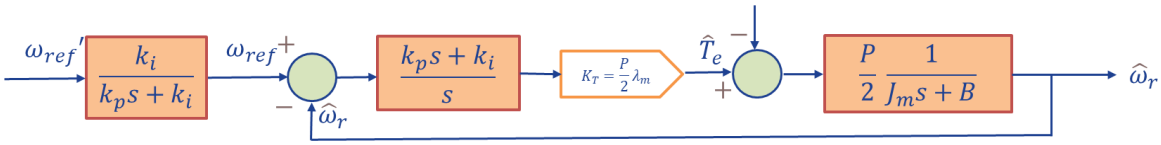

Figure 2.10: Overall speed reference to PMSM speed diagram

Calculating the overall transfer function of the presented model can be shown as Eqn. (2.54). this is representation of the transfer function that relates the output speed of the machine to the speed reference of the controller.

$$\frac{\hat{\omega}_r}{\omega_{ref}'} = K_T \frac{P}{2} \cdot \frac{k_i}{J_m s^2 + K_T \frac{P}{2}(k_p s + k_i)} \tag{2.54}$$

This transfer function can be compared with the standard form of a second order system as it is shown in Eqn. (2.55).

$$T = \frac{\omega_s^2}{s^2 + 2\zeta\omega_s s + \omega_s^2} \tag{2.55}$$

In this expression, ω_s is the system's natural frequency and ζ is the damping. The control gains and these parameters are related through Eqn. (2.56), (2.57).

$$k_i = \omega_s^2 \frac{2J_m}{K_T P} \tag{2.56}$$

$$k_p = \omega_s 2\zeta \frac{2J_m}{K_T P} \tag{2.57}$$

The natural frequency is selected to be much lower than ω_c. The damping is set to $1/\sqrt{2}$ which provides a good tradeoff between overshoot and speed. With having this analytical approach, the controller's coefficients are calculated based on the relating internal parameters of the machine to achieved desired response characteristics.

2.7 Controller for the Induction Machine

In this thesis, the induction machine is used to put mechanical load on the shaft of the PM machine. In order to do that this machine is driven in generator operation mode. In this case the supply frequency of the machine should be less than the mechanical speed of the machine with number of poles considered. In the case that the speed of the rotor is equal to the speed of the electrical current of the stator, no torque is generated by the machine since the current in the rotor bars is equal to zero. Difference in the speed of the rotor and the stator current is the reason for induction of current in the rotor circuit and generation of torque. While different control strategies such as field-oriented control, direct torque control and model predictive control are available for controlling the induction machine, the open-loop V/F strategy is selected and implemented for this implementation due to the simplicity of deployment and computational benefits in real-time implementation in HIL. V/F stands for voltage over frequency and is associated with a control strategy that keeps the ratio of the voltage and frequency to be a defined constant. By keeping this ratio constant, the value of the flux is also roughly kept constant ensuring that saturation would not happen in the stator core of the machine. Using the nominal values of the supply voltage and operating frequency that are mentioned on the plate of the machine, the ratio of V/F is calculated, and using proper Simulink blocks controller is implemented as shown in Fig 2.11. By putting the value of the speed reference, this controller generates the three-phase voltages required for the machine that satisfies the predefined ratio. In the case that the

induction machine is coupled through the torque sensor with the PM machine as the test setup developed in this Theis, it is possible to change the reference speed for the induction machine to reach the satisfactory torque value on the mechanical shaft. This will be used to put the PM machine at the load operating point of interest.

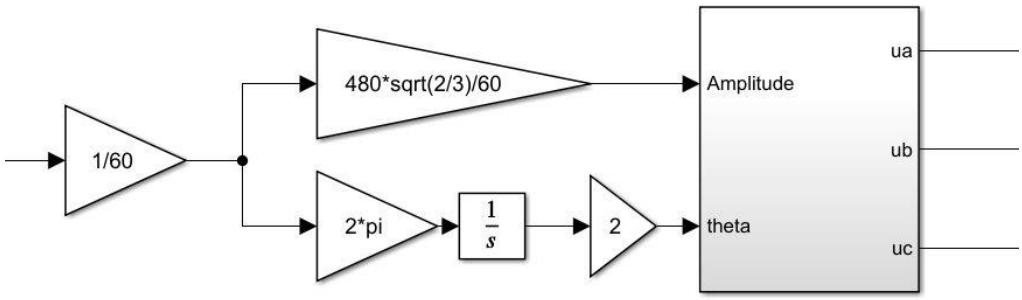

Figure 2.11: Induction machine V/F control implementation in Simulink

2.8 PMSM Simulation Results

The PMSM simulated in this section has its specifications provided by POWERTECH industrial motors, Inc. It is a 230 V motor of 3 HP, with 3 pair of poles, 5000 RPM, nominal torque of 4.27 Nm, maximum (momentary) torque of 48.46 Nm, nominal current of 9 A, maximum (momentary) current of 313 A. It is not provided the maximum periods for sustaining maximum torque and current. Fig. 2.12 shows the curves of speed, torque and currents obtained when the vector control drive is applied to the PMSM. From the curves, to keep the motor under its nominal conditions for torque and current, the start procedure must last no less than 0.36 seconds. The PWM frequency was first set to 80 kHz.

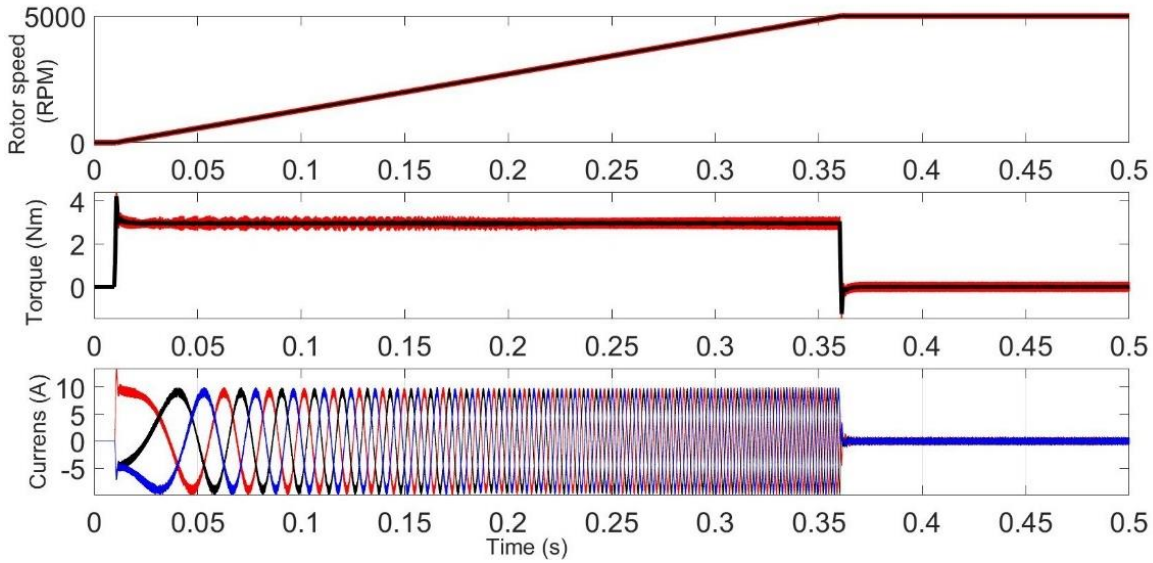

Figure 2.12: Speed, torque and currents obtained from PMSM FOC drive system.

Developed controller that was demonstrated in this section is used for two reasons. First it is used in chapter 3 to control the model of coupled PM and IM and apply the TBM characterization and demonstrate the TBM methodology in simulation. Secondly the same developed controller is used inside HIL alongside additional sensor and calibration blocks to control the real machines in experiments that have been performed in this study.

2.9 Converting State Space Model to Transfer Function Matrix

As it was shown in the previous part, state space model of PMSM is developed. This model is achieved by linearizing the original equations that include the dynamics of the machine at a specific operating point. Solving this state space model equations with proper timestep can show the time domain response of the PM machine for the fundamental component of the system as the original d-q represented equations are focusing on representing the fundamental component. In the case that having the response of other additional harmonics of the system and potential harmonic interactions in the nonlinear components of the system such as PWM modulator are of significant interest Generalized State Space model or Dynamic Phasor modeling method can be used to study and model the desired system. Example of such an implementation to study the model of

interconnected voltage source inverters is represented in [4],[6]. In this thesis the focus of the study is more on the transfer function representation of the input output dynamic ratio of the terminals of the system rather than the time domain representation of these quantities. Such an input output transfer function representation of the PM machine is achievable by converting the state space model of the machine into the Laplace domain. This transformation is demonstrated in this section. The standard form of state-space model for a system is shown in Eqn. (2.58).

$$\begin{aligned} \dot{X} &= AX + BU \\ Y &= CX + DU \end{aligned} \tag{2.58}$$

We can write the following Laplace form of the state space model as Eqn. (2.59)

$$\begin{aligned} sX(s) &= AX(s) + BU(s) \\ Y(s) &= CX(s) + DU(s) \end{aligned} \tag{2.59}$$

By moving the state variable matrix to the left side, we can write Eqn. (2.60)

$$(sI - A)X(s) = BU(s) \tag{2.60}$$

By multiplying both side of the previous equation with $(sI - A)^{-1}$ we can have Eqn. (2.60).

$$X(s) = (sI - A)^{-1}BU(s) \tag{2.60}$$

Finally, we can write $Y(s)$ as Eqn. (2.61).

$$Y(s) = \underbrace{[C(sI - A)^{-1}B + D]}_{\text{Transfer Function Matrix } T(s)}\ U(s) \tag{2.61}$$

Resulting set of transfer functions are SISO transfer functions of the system. Terminal behavioral modeling method can achieve SISO transfer functions with a series of measurement and a related mathematical calculation. Since both decoupled TBM model of the PM machine and the SISO transfer function representation of the PM machine are only representing the dynamics of the machine by focusing in similar input-output representation of the transfer functions, the SISO model derived from the original equations

that describe the dynamics of the PM machine can be used as a reference to validate the capability of the TBM decoupling procedure to eliminate the dynamics of the load and source. This comparison will be elaborated in more details in Chapter 3 which discusses the capability of the decoupling procedure to eliminate the effects of the dynamics of the load and source on the expected linearized input-output transfer functions related to the permanent magnet machine.

Chapter 3

Introduction

Ever increasing trends in the application of power converters and electrical machines and the stability assessment aspects are the incentive to explore different fundamental approaches for modeling and simulation. Having high fidelity models of different components of a system enables detailed studies that ensures the robust operation of the system. Analyses of small-signal based methods for DC distributed systems and AC distributed systems have been thoroughly demonstrated in the literature [38]–[41]. Characterization of the system on the basis of a series of mathematically driven or experimentally measured frequency responses and applying general Nyquist criteria is a major method commonly used for this type of stability assessment [42]–[45]. This chapter initiates demonstration of the terminal behavioral modeling approach in details for three-phase active rectifier and continues to develop this modeling approach for permanent magnet synchronous machine by describing the similarities between the small signal representations of the two models. Using the decoupling procedure, it is demonstrated that the dynamics of the subsystems that are connected to the terminals of the model under study can be eliminated leaving the true dynamics of the standalone system.

3.1 Terminal-Behavioral Modeling of an Active Rectifier

In order to understand Terminal-Behavioral Modeling (TBM) of electric machines it is important to understand some background work on the TBM approach for power electronics converters. In this case, three-phase active rectifiers are represented, and using the TBM modeling method unterminated model of the converter is developed. Behavioral models related to DC-DC converters and active rectifiers are discussed in the literature [11], [26], [40], [46]. Similarity between TBM of active rectifier and PMSM is the incentive for detailed study of TBM method for active rectifiers. Fig. 3.1 shows the small signal model of active rectifier.

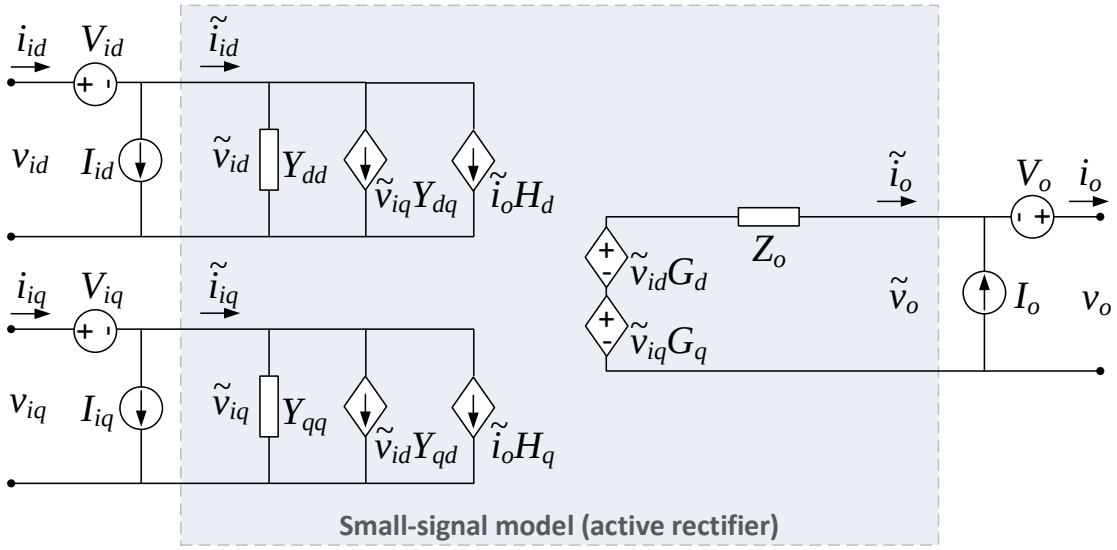

Figure 3.1: Small signal representation of an active rectifier

Input-output relations that describe the operation of active rectifier are represented in the following part. Transfer functions included in here are unterminated transfer functions of the converter and represent the active rectifier without the effect of the load and the source. In the case of real-world application converters are often connected to a source that is not a simple ideal voltage source and might include internal impedance or controllers that have their associated dynamics. Using decoupling procedure similar to what is represented in [33] it is possible to decouple the effect of the dynamics that are related to the source and load and obtain the single input signal output transfer functions that only include the dynamics that are related to the converter and is decoupled from the source and load.

$$\begin{bmatrix} \tilde{v}_o \\ \tilde{\imath}_{id} \\ \tilde{\imath}_{iq} \end{bmatrix} = \begin{bmatrix} G_d & G_q & Z_o \\ Y_{dd} & Y_{dq} & H_d \\ Y_{qd} & Y_{qq} & H_q \end{bmatrix} . \begin{bmatrix} \tilde{v}_{id} \\ \tilde{v}_{iq} \\ \tilde{\imath}_O \end{bmatrix} \tag{3.1}$$

In order to obtain the TBM of active rectifier three sets of measurements are required. In each test one of the three terminals of the model is perturbed and the effect of that perturbation on specific terminals of the system is recorded to form specific transfer functions that are used to decouple the effect of the load and source and obtain the

decoupled model of the system. First measurement set is related to perturbing the input voltage in *d* axis. Fig. 3.2 is associated with this measurement and Eqn. (3.2)- (3.4) are showing the transfer functions that should be measured in this experiment.

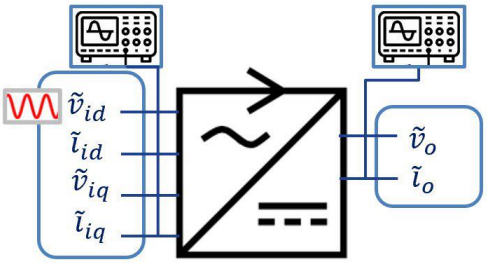

Figure 3.2: First measurement set perturbation for active rectifier TBM

$$\frac{\tilde{v}_o}{\tilde{v}_{id}} = G_d + G_q \frac{\tilde{v}_{iq}}{\tilde{v}_{id}} + Z_o \frac{\tilde{\imath}_O}{\tilde{v}_{id}} \tag{3.2}$$

$$\frac{\tilde{\imath}_{id}}{\tilde{v}_{id}} = Y_{dd} + Y_{dq} \frac{\tilde{v}_{iq}}{\tilde{v}_{id}} + H_d \frac{\tilde{\imath}_O}{\tilde{v}_{id}} \tag{3.3}$$

$$\frac{\tilde{\imath}_{iq}}{\tilde{v}_{id}} = Y_{qd} + Y_{qq} \frac{\tilde{v}_{iq}}{\tilde{v}_{id}} + H_q \frac{\tilde{\imath}_O}{\tilde{v}_{id}} \tag{3.4}$$

Second measurement and perturbation set is related to perturbing the input voltage in *q* axis. Fig. 3.3 is associated with this measurement and Eqn. 33 are showing the transfer functions that should be measured in this experiment.

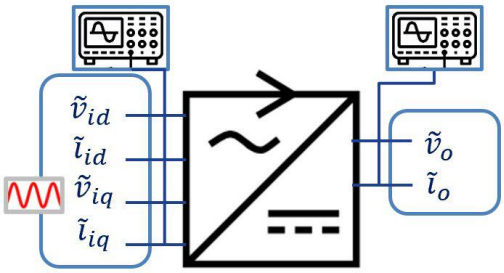

Figure 3.3: Second measurement set perturbation for active rectifier TBM

$$\frac{\tilde{v}_o}{\tilde{v}_{iq}} = G_d \frac{\tilde{v}_{id}}{\tilde{v}_{iq}} + G_q + Z_0 \frac{\tilde{\imath}_O}{\tilde{v}_{iq}} \tag{3.5}$$

$$\frac{\tilde{\imath}_{id}}{\tilde{v}_{iq}} = Y_{dd} \frac{\tilde{v}_{id}}{\tilde{v}_{iq}} + Y_{dq} + H_d \frac{\tilde{\imath}_O}{\tilde{v}_{iq}} \tag{3.6}$$

$$\frac{\tilde{\imath}_{iq}}{\tilde{v}_{iq}} = Y_{qd} \frac{\tilde{v}_{id}}{\tilde{v}_{iq}} + Y_{qq} + H_q \frac{\tilde{\imath}_o}{\tilde{v}_{iq}} \tag{3.7}$$

Third measurement and perturbation set are related to perturbing output current of the active rectifier. Fig. 3.4 is associated with this measurement and following equations shown in (3.5)- (3.7) are showing the transfer functions that should be measured in this experiment.

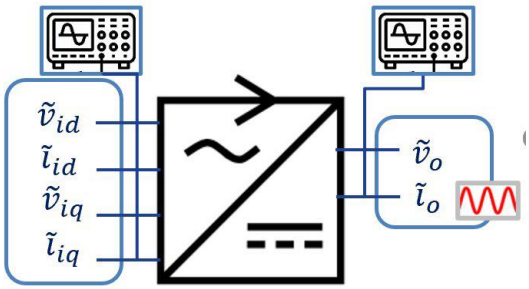

Figure 3.4: Third measurement set perturbation for active rectifier TBM

$$\frac{\tilde{v}_o}{\tilde{\imath}_o} = G_d \frac{\tilde{v}_{id}}{\tilde{\imath}_o} + G_q \frac{\tilde{v}_{iq}}{\tilde{\imath}_o} + Z_o \tag{3.5}$$

$$\frac{\tilde{\imath}_{id}}{\tilde{\imath}_O} = Y_{dd} . \frac{\tilde{v}_{id}}{\tilde{\imath}_O} + Y_{dq} . \frac{\tilde{v}_{iq}}{\tilde{\imath}_O} + H_d \tag{3.6}$$

$$\frac{\tilde{\imath}_{iq}}{\tilde{\imath}_o} = Y_{qd} \cdot \frac{\tilde{v}_{id}}{\tilde{\imath}_o} + Y_{qq} \cdot \frac{\tilde{v}_{iq}}{\tilde{\imath}_o} + H_q \tag{3.7}$$

All 9 equations that were described in the previous part can be summarized in the form of Eqn. (3.10). This matrix form is formed to facilitate the calculation of unterminated model using mathematical manipulation on the formed set of equations.

$$\begin{bmatrix} \frac{\tilde{v}_o}{\tilde{v}_{id}} & \frac{\tilde{v}_o}{\tilde{v}_{iq}} & \frac{\tilde{v}_o}{\tilde{\imath}_o} \\ \frac{\tilde{\imath}_{id}}{\tilde{v}_{id}} & \frac{\tilde{\imath}_{id}}{\tilde{v}_{iq}} & \frac{\tilde{\imath}_{id}}{\tilde{\imath}_o} \\ \frac{\tilde{\imath}_{iq}}{\tilde{v}_{id}} & \frac{\tilde{\imath}_{iq}}{\tilde{v}_{iq}} & \frac{\tilde{\imath}_{iq}}{\tilde{\imath}_o} \end{bmatrix} = \begin{bmatrix} G_d & G_q & Z_o \\ Y_{dd} & Y_{dq} & H_d \\ Y_{qd} & Y_{qq} & H_q \end{bmatrix} \begin{bmatrix} 1 & \frac{\tilde{v}_{id}}{\tilde{v}_{iq}} & \frac{\tilde{v}_{id}}{\tilde{\imath}_O} \\ \frac{\tilde{v}_{iq}}{\tilde{v}_{id}} & 1 & \frac{\tilde{v}_{iq}}{\tilde{\imath}_o} \\ \frac{\tilde{\imath}_O}{\tilde{v}_{id}} & \frac{\tilde{\imath}_O}{\tilde{v}_{iq}} & 1 \end{bmatrix} \tag{3.10}$$

By multiplying both sides of the equation by the inverse matrix it is possible to remove the measurement related matrices from one side of the equations and achieve the unterminated set of transfer functions as it is shown in Eqn. (3.11).

$$\begin{bmatrix} \frac{\tilde{v}_o}{\tilde{v}_{id}} & \frac{\tilde{v}_o}{\tilde{v}_{iq}} & \frac{\tilde{v}_o}{\tilde{\imath}_o} \\ \frac{\tilde{\imath}_{id}}{\tilde{v}_{id}} & \frac{\tilde{\imath}_{id}}{\tilde{v}_{iq}} & \frac{\tilde{\imath}_{id}}{\tilde{\imath}_o} \\ \frac{\tilde{\imath}_{iq}}{\tilde{v}_{id}} & \frac{\tilde{\imath}_{iq}}{\tilde{v}_{iq}} & \frac{\tilde{\imath}_{iq}}{\tilde{\imath}_o} \end{bmatrix} \begin{bmatrix} 1 & \frac{\tilde{v}_{id}}{\tilde{v}_{iq}} & \frac{\tilde{v}_{id}}{\tilde{\imath}_O} \\ \frac{\tilde{v}_{iq}}{\tilde{v}_{id}} & 1 & \frac{\tilde{v}_{iq}}{\tilde{\imath}_o} \\ \frac{\tilde{\imath}_O}{\tilde{v}_{id}} & \frac{\tilde{\imath}_O}{\tilde{v}_{iq}} & 1 \end{bmatrix}^{-1} = \begin{bmatrix} G_d & G_q & Z_o \\ Y_{dd} & Y_{dq} & H_d \\ Y_{qd} & Y_{qq} & H_q \end{bmatrix} \begin{bmatrix} 1 & \frac{\tilde{v}_{id}}{\tilde{v}_{iq}} & \frac{\tilde{v}_{id}}{\tilde{\imath}_O} \\ \frac{\tilde{v}_{iq}}{\tilde{v}_{id}} & 1 & \frac{\tilde{v}_{iq}}{\tilde{\imath}_o} \\ \frac{\tilde{\imath}_O}{\tilde{v}_{id}} & \frac{\tilde{\imath}_O}{\tilde{v}_{iq}} & 1 \end{bmatrix} * \begin{bmatrix} 1 & \frac{\tilde{v}_{id}}{\tilde{v}_{iq}} & \frac{\tilde{v}_{id}}{\tilde{\imath}_O} \\ \frac{\tilde{v}_{iq}}{\tilde{v}_{id}} & 1 & \frac{\tilde{v}_{iq}}{\tilde{\imath}_o} \\ \frac{\tilde{\imath}_O}{\tilde{v}_{id}} & \frac{\tilde{\imath}_O}{\tilde{v}_{iq}} & 1 \end{bmatrix}^{-1} \tag{3.11}$$

Right side of the Eqn. (3.11) can be simplified to form equation (3.12). Calculation of transfer functions on the left side which is not necessarily decoupled from additional dynamics of the load and source, results in the matrix on the right side which only includes the dynamics related to the system under study and excludes the dynamics couplings of the load and source.

$$\underbrace{\begin{bmatrix} \frac{\tilde{v}_o}{\tilde{v}_{id}} & \frac{\tilde{v}_o}{\tilde{v}_{iq}} & \frac{\tilde{v}_o}{\tilde{\imath}_o} \\ \frac{\tilde{\imath}_{id}}{\tilde{v}_{id}} & \frac{\tilde{\imath}_{id}}{\tilde{v}_{iq}} & \frac{\tilde{\imath}_{id}}{\tilde{\imath}_o} \\ \frac{\tilde{\imath}_{iq}}{\tilde{v}_{id}} & \frac{\tilde{\imath}_{iq}}{\tilde{v}_{iq}} & \frac{\tilde{\imath}_{iq}}{\tilde{\imath}_o} \end{bmatrix} \begin{bmatrix} 1 & \frac{\tilde{v}_{id}}{\tilde{v}_{iq}} & \frac{\tilde{v}_{id}}{\tilde{\imath}_O} \\ \frac{\tilde{v}_{iq}}{\tilde{v}_{id}} & 1 & \frac{\tilde{v}_{iq}}{\tilde{\imath}_o} \\ \frac{\tilde{\imath}_O}{\tilde{v}_{id}} & \frac{\tilde{\imath}_O}{\tilde{v}_{iq}} & 1 \end{bmatrix}^{-1}}_{measurements} = \underbrace{\begin{bmatrix} G_d & G_q & Z_o \\ Y_{dd} & Y_{dq} & H_d \\ Y_{qd} & Y_{qq} & H_q \end{bmatrix}}_{Unterminated} \tag{3.12}$$

The first and the second matrices on the left side of the Eqn. (3.12) include the matrix of transfer functions that are based on the measurements and obtaining the measurements and calculating the mathematical result of the left side of the equation results in the unterminated SISO transfer functions that are shown in the right side of the equation.

3.2 Terminal-Behavioral Modeling of PMSM

In this section TBM of PMSM is calculated using similar approach that was used for obtaining the TBM of active rectifier. It will be shown that TBM of the two models are very similar to each other. Transfer functions included in TBM are unterminated transfer functions of the PMSM and represent the operation of the motor without the effect of the load and the source. In the case of real-world applications, the motor is often connected to a source which is not a simple ideal voltage source and might include internal impedance or controllers that have their associated dynamics. In this part it will be shown that using the TBM decoupling procedure is possible to decouple the effect of the dynamics that are related to the source and load and obtain the single input signal output transfer functions that only include the dynamics that are related to the motor and is decoupled from the source and load. Small-signal model of PM machine can be shown as Fig. 3.5.

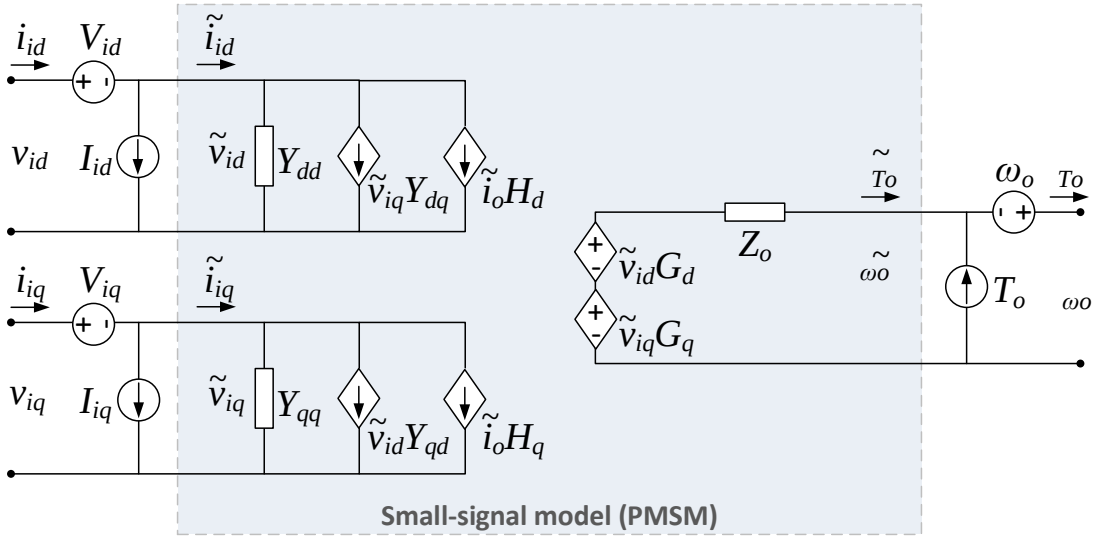

Figure 3.5. Small signal representation of a PMSM

In order to obtain the TBM of PMSM three set of measurements are required. In each test one of the three outputs of the model is perturbed and the effect of that perturbation on specific terminals of the system is recorded to form specific transfer functions that are used to decouple the effect of the load and source and obtain the decoupled model of the motor. The first measurement/perturbation set is related to perturbing the input voltage in d axis. Fig. 3.6 is associated with this measurement and following equations (3.13)-(3.15) are showing the transfer functions that should be measured in this experiment.

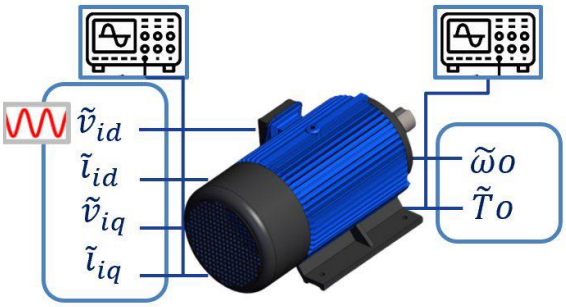

Figure 3.6: First measurement set perturbation for PMSM TBM

$$\frac{\tilde{\omega}o}{\tilde{v}_{id}} = G_d + G_q \frac{\tilde{v}_{iq}}{\tilde{v}_{id}} + Z_o \frac{\tilde{T}o}{\tilde{v}_{id}} \tag{3.13}$$

$$\frac{\tilde{\imath}_{id}}{\tilde{v}_{id}} = Y_{dd} + Y_{dq} \frac{\tilde{v}_{iq}}{\tilde{v}_{id}} + H_d \frac{\tilde{T}o}{\tilde{v}_{id}} \tag{3.14}$$

$$\frac{\tilde{\imath}_{iq}}{\tilde{v}_{id}} = Y_{qd} + Y_{qq} \frac{\tilde{v}_{iq}}{\tilde{v}_{id}} + H_q \frac{\tilde{T}o}{\tilde{v}_{id}} \tag{3.15}$$

Second measurement/perturbation set is related to perturbing the input voltage in *q* axis. Fig. 3.7 is associated with this measurement and Eqn. (3.16)-(3.18) are showing the transfer functions that should be measured in this experiment.

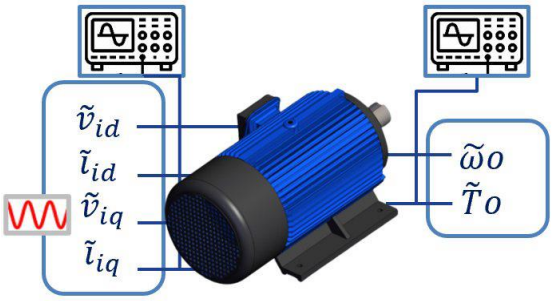

Figure 3.7: Second measurement set perturbation for PMSM TBM

$$\frac{\tilde{\omega}o}{\tilde{v}_{iq}} = G_d \frac{\tilde{v}_{id}}{\tilde{v}_{iq}} + G_q + Z_0 \frac{\tilde{T}o}{\tilde{v}_{iq}} \tag{3.16}$$

$$\frac{\tilde{\imath}_{id}}{\tilde{v}_{iq}} = Y_{dd} \frac{\tilde{v}_{id}}{\tilde{v}_{iq}} + Y_{dq} + H_d \frac{\tilde{T}o}{\tilde{v}_{iq}} \tag{3.17}$$

$$\frac{\tilde{\imath}_{iq}}{\tilde{v}_{iq}} = Y_{qd} \frac{\tilde{v}_{id}}{\tilde{v}_{iq}} + Y_{qq} + H_q \frac{\tilde{T}o}{\tilde{v}_{iq}} \tag{3.18}$$

Third measurement set is related to perturbing the torque imposed on machine's shaft. Fig. 3.8 is associated with this measurement and Eqn. (3.19)-(3.21) are showing the transfer functions that should be measured in this experiment.

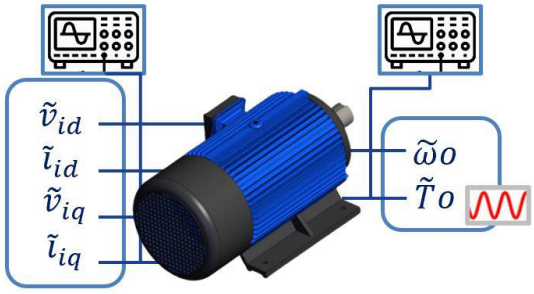

Figure 3.8: Third measurement set perturbation for PMSM TBM

$$\frac{\tilde{\omega}o}{\tilde{T}o} = G_d \frac{\tilde{v}_{id}}{\tilde{T}o} + G_q \frac{\tilde{v}_{iq}}{\tilde{T}o} + Z_o \tag{3.19}$$

$$\frac{\tilde{\imath}_{id}}{\tilde{T}o} = Y_{dd} \cdot \frac{\tilde{v}_{id}}{\tilde{T}o} + Y_{dq} \cdot \frac{\tilde{v}_{iq}}{\tilde{T}o} + H_d \tag{3.20}$$

$$\frac{\tilde{l}_{iq}}{\tilde{T}o} = Y_{qd} \cdot \frac{\tilde{v}_{id}}{\tilde{T}o} + Y_{qq} \cdot \frac{\tilde{v}_{iq}}{\tilde{T}o} + H_q \tag{3.21}$$

All nine equations that relate the input output dynamic relationships described in Eqn. (3.13)-(3.21) can be summarized in the form of Eqn. (3.22). This form of writing the equations simplifies the future mathematical operation using the matrix representation of the equations.

$$\begin{bmatrix} \frac{\tilde{\omega}o}{\tilde{v}_{id}} & \frac{\tilde{\omega}o}{\tilde{v}_{iq}} & \frac{\tilde{\omega}o}{\tilde{T}o} \\ \frac{\tilde{l}_{id}}{\tilde{v}_{id}} & \frac{\tilde{l}_{id}}{\tilde{v}_{iq}} & \frac{\tilde{l}_{id}}{\tilde{T}o} \\ \frac{\tilde{l}_{iq}}{\tilde{v}_{id}} & \frac{\tilde{l}_{iq}}{\tilde{v}_{iq}} & \frac{\tilde{l}_{iq}}{\tilde{T}o} \end{bmatrix} = \begin{bmatrix} G_d & G_q & Z_o \\ Y_{dd} & Y_{dq} & H_d \\ Y_{qd} & Y_{qq} & H_q \end{bmatrix} \begin{bmatrix} 1 & \frac{\tilde{v}_{id}}{\tilde{v}_{iq}} & \frac{\tilde{v}_{id}}{\tilde{T}o} \\ \frac{\tilde{v}_{iq}}{\tilde{v}_{id}} & 1 & \frac{\tilde{v}_{iq}}{\tilde{T}o} \\ \frac{\tilde{T}o}{\tilde{v}_{id}} & \frac{\tilde{T}o}{\tilde{v}_{iq}} & 1 \end{bmatrix} \tag{3.22}$$

By multiplying both sides of the equation (3.22) by the inverse matrix it is possible to remove the measurement related matrices from one side of the equations and achieve the unterminated set of transfer functions as it is shown in Eqn. (3.23).

$$\begin{bmatrix} \frac{\tilde{\omega}o}{\tilde{v}_{id}} & \frac{\tilde{\omega}o}{\tilde{v}_{iq}} & \frac{\tilde{\omega}o}{\tilde{T}o} \\ \frac{\tilde{l}_{id}}{\tilde{v}_{id}} & \frac{\tilde{l}_{id}}{\tilde{v}_{iq}} & \frac{\tilde{l}_{id}}{\tilde{T}o} \\ \frac{\tilde{l}_{iq}}{\tilde{v}_{id}} & \frac{\tilde{l}_{iq}}{\tilde{v}_{iq}} & \frac{\tilde{l}_{iq}}{\tilde{T}o} \end{bmatrix} \begin{bmatrix} 1 & \frac{\tilde{v}_{id}}{\tilde{v}_{iq}} & \frac{\tilde{v}_{id}}{\tilde{T}o} \\ \frac{\tilde{v}_{iq}}{\tilde{v}_{id}} & 1 & \frac{\tilde{v}_{iq}}{\tilde{T}o} \\ \frac{\tilde{T}o}{\tilde{v}_{id}} & \frac{\tilde{T}o}{\tilde{v}_{iq}} & 1 \end{bmatrix}^{-1} = \begin{bmatrix} G_d & G_q & Z_o \\ Y_{dd} & Y_{dq} & H_d \\ Y_{qd} & Y_{qq} & H_q \end{bmatrix} * \tag{3.23}$$

$$\begin{bmatrix} 1 & \frac{\tilde{v}_{id}}{\tilde{v}_{iq}} & \frac{\tilde{v}_{id}}{\tilde{T}o} \\ \frac{\tilde{v}_{iq}}{\tilde{v}_{id}} & 1 & \frac{\tilde{v}_{iq}}{\tilde{T}o} \\ \frac{\tilde{T}o}{\tilde{v}_{id}} & \frac{\tilde{T}o}{\tilde{v}_{iq}} & 1 \end{bmatrix} \begin{bmatrix} 1 & \frac{\tilde{v}_{id}}{\tilde{v}_{iq}} & \frac{\tilde{v}_{id}}{\tilde{T}o} \\ \frac{\tilde{v}_{iq}}{\tilde{v}_{id}} & 1 & \frac{\tilde{v}_{iq}}{\tilde{T}o} \\ \frac{\tilde{T}o}{\tilde{v}_{id}} & \frac{\tilde{T}o}{\tilde{v}_{iq}} & 1 \end{bmatrix}^{-1}$$

This equation can be simplified to form (3.24). In this equation, transfer functions that are presented on the left side could include the dynamics of the controller as well as the dynamics of the mechanical load connected through the shaft. However by calculating the result of the left side matrices, decoupled transfer functions on the right side are formed that exclude dynamics of the load and source.

$$\begin{bmatrix} \frac{\tilde{\omega}o}{\tilde{v}_{id}} & \frac{\tilde{\omega}o}{\tilde{v}_{iq}} & \frac{\tilde{\omega}o}{\tilde{T}o} \\ \frac{\tilde{\imath}_{id}}{\tilde{v}_{id}} & \frac{\tilde{\imath}_{id}}{\tilde{v}_{iq}} & \frac{\tilde{\imath}_{id}}{\tilde{T}o} \\ \frac{\tilde{\imath}_{iq}}{\tilde{v}_{id}} & \frac{\tilde{\imath}_{iq}}{\tilde{v}_{iq}} & \frac{\tilde{\imath}_{iq}}{\tilde{T}o} \end{bmatrix} \begin{bmatrix} 1 & \frac{\tilde{v}_{id}}{\tilde{v}_{iq}} & \frac{\tilde{v}_{id}}{\tilde{T}o} \\ \frac{\tilde{v}_{iq}}{\tilde{v}_{id}} & 1 & \frac{\tilde{v}_{iq}}{\tilde{T}o} \\ \frac{\tilde{T}o}{\tilde{v}_{id}} & \frac{\tilde{T}o}{\tilde{v}_{iq}} & 1 \end{bmatrix}^{-1} = \begin{bmatrix} G_d & G_q & Z_o \\ Y_{dd} & Y_{dq} & H_d \\ Y_{qd} & Y_{qq} & H_q \end{bmatrix} \quad (3.24)$$

The first and the second matrices on the left side of the equation include the matrix of transfer functions that are based on the measurements and obtaining the measurements and calculating the mathematical result of the left side of equation results in the unterminated SISO transfer functions that are shown in the right side of the equations.

3.3 TBM For Decoupling Load And Source Dynamics of Active Rectifier

In this part an example of the applying the decoupling procedure to decouple the dynamics of the load and source for an active rectifier is presented. As it is shown in Fig 3.9, the active rectifier is connected to a voltage source with internal impedance in d axis. This means that the d-axis voltage in the input terminal of the rectifier is affected by the value of the current in this axis. Input terminal voltage on the q-axis however is connected to an ideal voltage source meaning that the value of the q-axis voltage is not affected by the operation of the rectifier. On the load side, the load consists of an ideal current sync and a parallel admittance branch. In this case the load side also has additional dynamics.

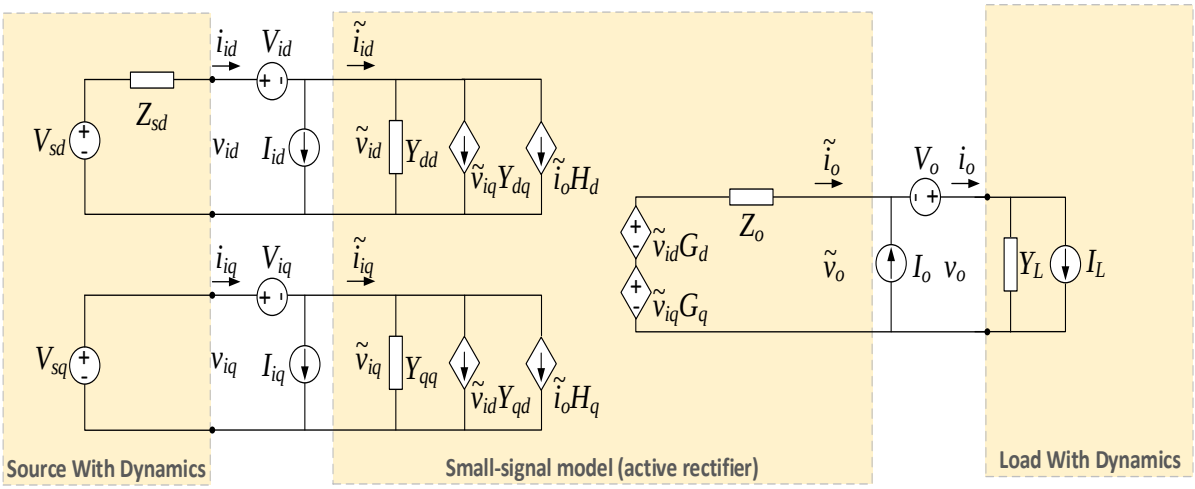

Figure 3.9: Small signal model of active rectifier with non-ideal source and loads

In the case of dynamics from the load and source, directly measured transfer functions that are demonstrated in the previous part are computed mathematically, and the capability of the described method is shown. Equivalent small signal block diagram of Fig 3.9 is demonstrated in Fig 3.10. Using Fig 3.10, the mathematical expression for transfer functions required to perform the decoupling are calculated easily using the simple form of calculating a transfer function of direct and loop path or by using Mason's rule[47] for calculation of transfer functions. Representing the dynamics of the system of active rectifier and load and source in the form of Fig. 3.10, facilitates the calculation of various input-output transfer functions. In this representation, the dynamics of the source voltage are represented as a series impedance in the d-axis with ideal voltage source. On the other hand, the dynamics of the load are modeled as a combination of an ideal current sink and a parallel admittance branch. The additional dynamics defined in this instance are implemented to demonstrate the process of decoupling the load and source dynamics

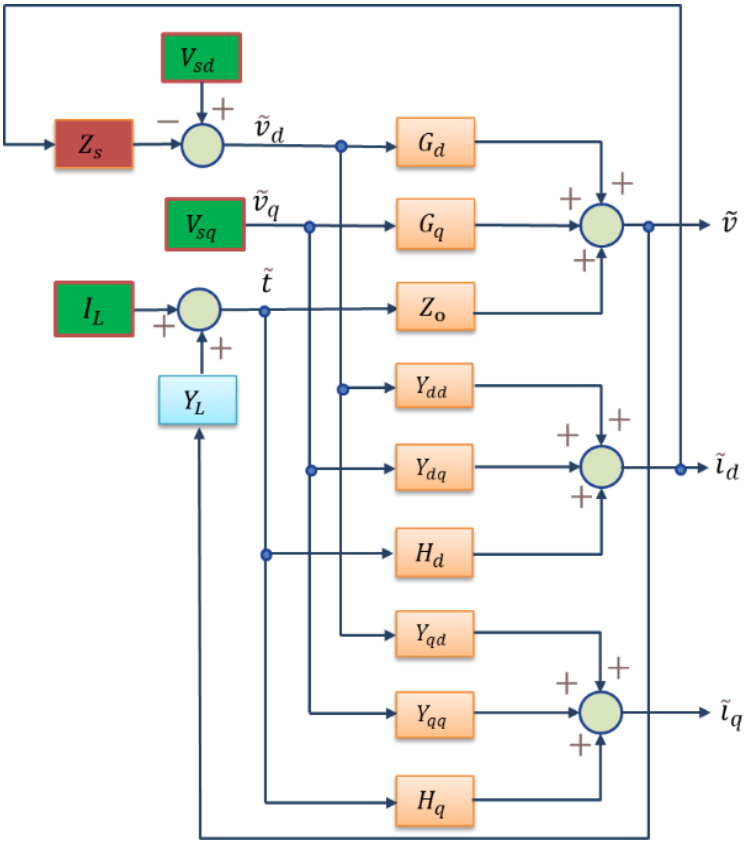

Figure 3.10: Small signal model of active rectifier with load and source dynamics

As an example of this calculation by showing the mathematical expression for the direct path and loop path we can calculate the transfer function $\frac{\tilde{v}}{\tilde{v}_{id}}$ as Fig 3.11. This transfer function is relatively simple to calculate by identifying the direct path and the loop path. Highlighted paths related to this calculation are represented. Calculation of the desired transfer functions for cases that involve multiple interconnected direct and loop paths are more complicated to be achievable by this method however it is possible to conveniently use Mason's rule formulation to calculate the required transfer functions.

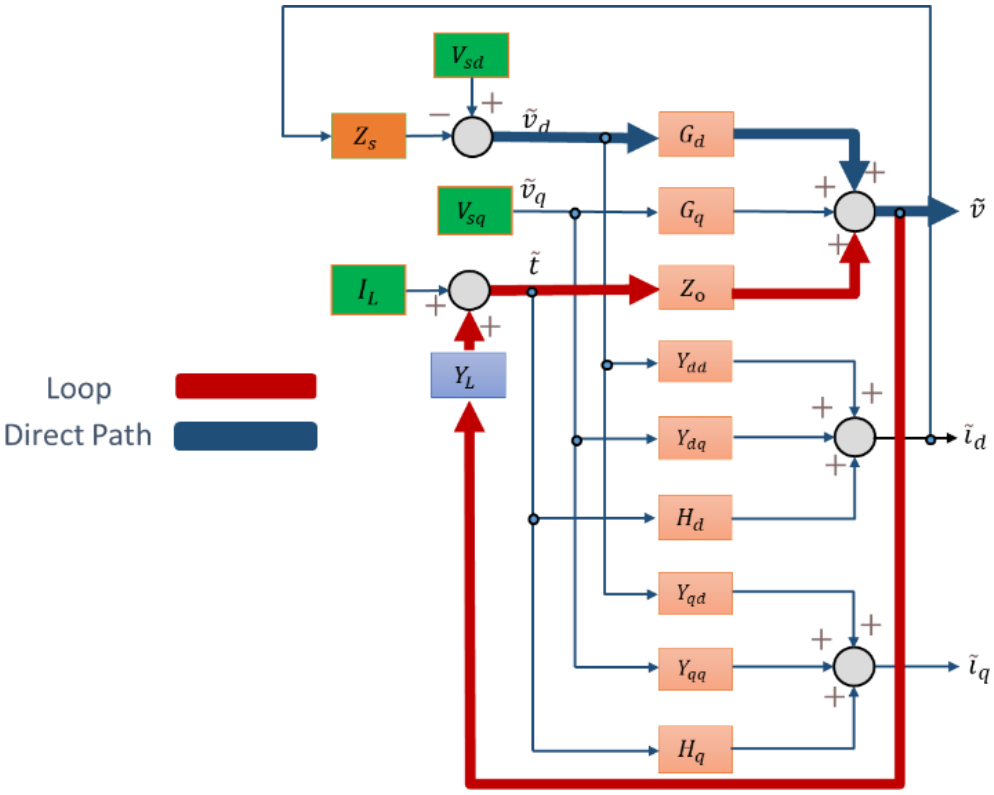

Figure 3.11: Calculation of a transfer function by direct and feedback loops

By considering the direct path and the loop path we can calculate the transfer function related to Fig 3.11 as equation (3.25)

(3.25)

$$\frac{\tilde{v}}{\tilde{v}_{id}} = \frac{G_d}{1 - Y_L Z_o}$$

Similarly, all transfer functions required for the decoupling procedure are calculated as Eqn. (3.26)-(3.39).

(3.26)

$$\frac{\tilde{v}_o}{\tilde{v}_{iq}} = \frac{G_q - \frac{Y_{dq} Z_s G_d}{1 + Z_s Y_{dd}}}{1 - Y_L Z_o + \frac{Y_L H_d Z_s G_d}{1 + Z_s Y_{dd}}}$$

(3.27)

$$\frac{\tilde{v}_o}{\tilde{\imath}_o} = Z_o - \frac{H_d Z_s G_d}{1 + Z_s Y_{dd}}$$

(3.28)

$$\frac{\tilde{\imath}_{id}}{\tilde{v}_{id}} = Y_{dd} + \frac{G_d Y_L H_d}{1 - Y_L Z_o}$$

(3.29)

$$\frac{\tilde{\imath}_{id}}{\tilde{v}_{iq}} = \frac{Y_{dq} + \frac{G_q Y_L H_d}{1 - Y_L Z_o}}{1 + Z_s Y_{dd} + \frac{Y_L H_d Z_s G_d}{1 - Y_L Z_o}}$$

(3.30)

$$\frac{\tilde{\imath}_{id}}{\tilde{\imath}_o} = \frac{H_d}{1 + Z_s Y_{dd}}$$

(3.31)

$$\frac{\tilde{\imath}_{iq}}{\tilde{v}_{id}} = Y_{qd} + \frac{G_d Y_L H_q}{1 - Y_L Z_o}$$

(3.32)

$$\frac{\tilde{\imath}_{iq}}{\tilde{v}_{iq}} = Y_{qq} + \frac{\frac{-Y_{dq}Z_sY_{qd}}{1+Z_sY_{dd}} + \frac{G_qY_LH_q}{1-Y_LZ_o} - \frac{G_qY_LH_dZ_sY_{qd} + Y_{dq}Z_sG_dY_LH_q}{(1-Y_LZ_o)(1+Z_sY_{dd})}}{1 + \frac{Y_LH_dZ_sG_d}{(1-Y_LZ_o)(1+Z_sY_{dd})}}$$

(3.33)

$$\frac{\tilde{\imath}_{iq}}{\tilde{\imath}_o} = H_q - \frac{H_dZ_sY_{qd}}{1+Z_sY_{dd}}$$

(3.34)

$$\frac{\tilde{v}_{id}}{\tilde{v}_{iq}} = \frac{-Y_{dq}Z_s - \frac{G_qY_LH_dZ_s}{1-Y_LZ_o}}{1+Z_sY_{dd} + \frac{Y_LH_dZ_sG_d}{1-Y_LZ_o}}$$

(3.35)

$$\frac{\tilde{v}_{id}}{\tilde{\imath}_O} = \frac{-Z_sH_d}{1+Z_sY_{dd}}$$

(3.36)

$$\frac{\tilde{v}_{iq}}{\tilde{v}_{id}} = 0$$

(3.37)

$$\frac{\tilde{v}_{iq}}{\tilde{\imath}_o} = 0$$

(3.38)

$$\frac{\tilde{\imath}_O}{\tilde{v}_{id}} = \frac{Y_L G_d}{1 - Y_L Z_o}$$

(3.39)

$$\frac{\tilde{\imath}_O}{\tilde{v}_{iq}} = \frac{Y_L G_q - \frac{Y_{dq} Z_s G_d Y_L}{1 + Z_s Y_{dd}}}{1 - Y_L Z_o + \frac{Y_L H_d Z_s G_d}{1 + Z_s Y_{dd}}}$$

As it is observed form Eqn. (3.26) the unterminated transfer function of $\frac{\tilde{v}_o}{\tilde{v}_{iq}}$ is G_q however this transfer function is affected by terms related to the dynamics of the load and source as Y_L and Z_s as well as other internal dynamics of the active rectifier as Y_{dq} , Y_{dd}, H_d and G_d . This observation is useful for understanding the reasoning for decoupling procedure that is elaborated in this chapter. Since the model of that is calculated from the active rectifier should only reflect the dynamics of this system and exclude all additional dynamic couplings with other elements of the experiment. If this decoupling is performed successfully, then the unterminated model can be used in different environments as a component to study the dynamics interactions of given integrated systems. Similar dynamic coupling is also observed on other calculated terminal transfer functions as it is shown in Eqn. (3.27)-(3.39). After calculating the mathematical expression for all the required transfer functions, based on what was demonstrated earlier in the chapter, we can apply the decoupling procedure by substituting all the individual transfer functions into the matrices shown in Eqn. (3.40)- (3.41)

(3.40)

$$\underbrace{\begin{bmatrix} \frac{G_d}{1-Y_L Z_o} & \frac{G_q-\frac{Y_{dq} Z_s G_d}{1+Z_s Y_{dd}}}{1-Y_L Z_o+\frac{Y_L H_d Z_s G_d}{1+Z_s Y_{dd}}} & Z_o-\frac{H_d Z_s G_d}{1+Z_s Y_{dd}} \\ Y_{dd}+\frac{G_d Y_L H_d}{1-Y_L Z_o} & \frac{Y_{dq}+\frac{G_q Y_L H_d}{1-Y_L Z_o}}{1+Z_s Y_{dd}+\frac{Y_L H_d Z_s G_d}{1-Y_L Z_o}} & \frac{H_d}{1+Z_s Y_{dd}} \\ Y_{qd}+\frac{G_d Y_L H_q}{1-Y_L Z_o} & Y_{qq}+\frac{\frac{-Y_{dq} Z_s Y_{qd}}{1+Z_s Y_{dd}}+\frac{G_q Y_L H_q}{1-Y_L Z_o}-\frac{G_q Y_L H_d Z_s Y_{qd}+Y_{dq} Z_s G_d Y_L H_q}{(1-Y_L Z_o)(1+Z_s Y_{dd})}}{1+\frac{Y_L H_d Z_s G_d}{(1-Y_L Z_o)(1+Z_s Y_{dd})}} & H_q-\frac{H_d Z_s Y_{qd}}{1+Z_s Y_{dd}} \end{bmatrix}}_{\mathrm{T}_1}$$

$$\underbrace{\begin{bmatrix} 1 & \frac{-Y_{dq} Z_s-\frac{G_q Y_L H_d Z_s}{1-Y_L Z_o}}{1+Z_s Y_{dd}+\frac{Y_L H_d Z_s G_d}{1-Y_L Z_o}} & \frac{-Z_s H_d}{1+Z_s Y_{dd}} \\ 0 & 1 & 0 \\ \frac{Y_L G_d}{1-Y_L Z_o} & \frac{Y_L G_q-\frac{Y_{dq} Z_s G_d Y_L}{1+Z_s Y_{dd}}}{1-Y_L Z_o+\frac{Y_L H_d Z_s G_d}{1+Z_s Y_{dd}}} & 1 \end{bmatrix}^{-1}}_{\mathrm{T}_2} \tag{3.41}$$

By multiplying the resulting matrices, we can see that all the additional dynamics are mathematically cancelled and the resulting matrix of transfer functions has just the unterminated small signal transfer functions related to the active rectifier. This example confirms the capability of this methodology for decoupling the dynamics of the load and source. As it is shown in the Eqn. (3.42) dynamics of the source and load Z_s and Y_L and other dynamic couplings are not part of the represented resulting model and this model represents the dynamics of the unterminated model.

$$\mathrm{T}_1.\mathrm{T}_2 = \begin{bmatrix} G_d & G_q & Z_o \\ Y_{dd} & Y_{dq} & H_d \\ Y_{qd} & Y_{qq} & H_q \end{bmatrix} \tag{3.42}$$

3.4 Using TBM For Decoupling Load and Source Dynamics for PMSM Drive System

Having unterminated models of the machine is essential for performing the stability assessments of the system of interconnected power converters and machines. Small signal models of the induction machine have been used in for stability assessment in the literature[48], [49]. Without proper development and demonstration of an intuitive mathematical derivation, resulting models from direct frequency response measurements of the machines are not accurately demonstrating the dynamics of the machine as they are highly coupled with the dynamics of the controller and the mechanical load. In this section mathematical representation of the terminal behavioral decoupling procedure is applied on a permanent magnet synchronous machine. In this case, mechanical load also contributes to the dynamics of the system. In addition to the dynamics related to the mechanical load side, speed controller in the source also adds to the dynamics observed on terminals of the machine. It should be mentioned that in this part the controller of the PM machine is simplified to simplify derivation of the transfer functions related to the TBM decoupling procedure. Fig 3.12 demonstrates the small signal model of the PMSM, controller, and the dynamics of the load side. In this representation, the dynamics of the load is demonstrated as a mechanical admittance which in combination with a constant torque sink is connected to the output of the small signal model of the machine.

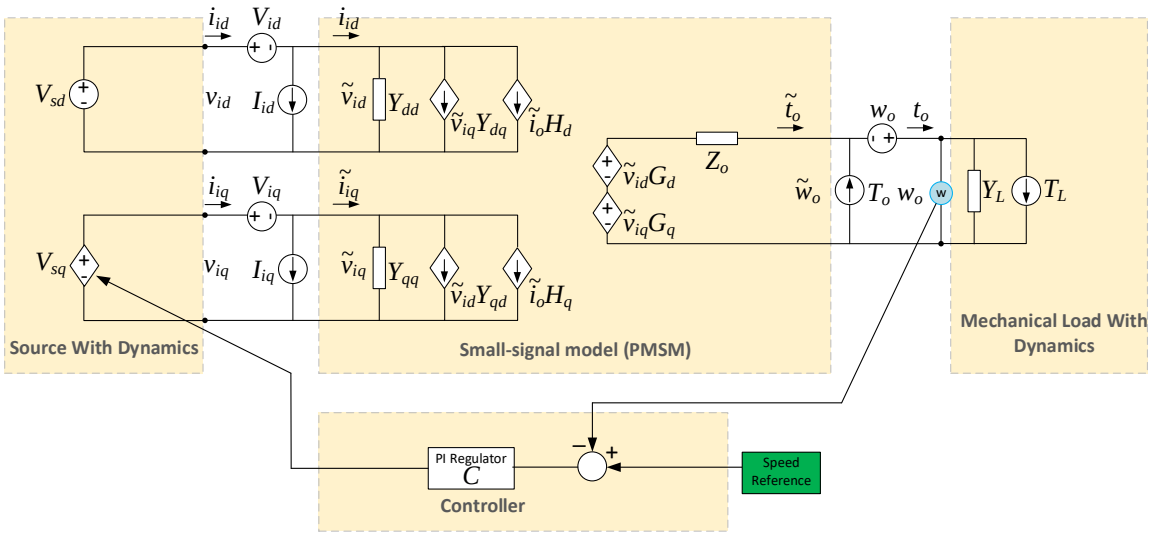

Figure 3.12: Demonstration of TBM of PM machine and simple Speed controller

In Fig. 3.13 transfer functions required by TBM decoupling procedure is calculated by showing the direct and loop paths on the equivalent small signal model of the system. Fig. 3.13 shows the small signal model of the system comprising the PM machine, controller and the load. Eqn. (3.43) shows the required transfer functions related to the decoupling procedure for PMSM machine.

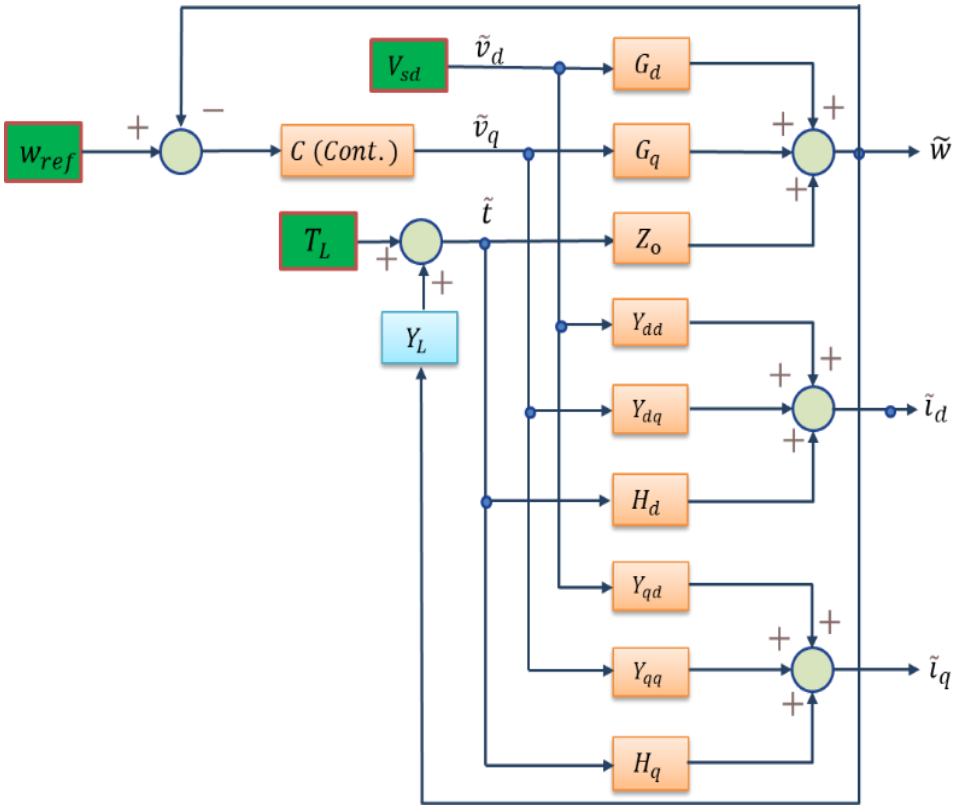

Figure 3.13: Simplified representation of the system of PMSM and controller

$$\begin{bmatrix} \frac{\tilde{\omega}}{\tilde{v}_d} & \frac{\tilde{\omega}}{\tilde{v}_q} & \frac{\tilde{\omega}}{\tilde{t}} \\ \frac{\tilde{\imath}_d}{\tilde{v}_d} & \frac{\tilde{\imath}_d}{\tilde{v}_q} & \frac{\tilde{\imath}_d}{\tilde{t}} \\ \frac{\tilde{\imath}_q}{\tilde{v}_d} & \frac{\tilde{\imath}_q}{\tilde{v}_{iq}} & \frac{\tilde{\imath}_q}{\tilde{t}} \end{bmatrix} \begin{bmatrix} 1 & \frac{\tilde{v}_d}{\tilde{v}_q} & \frac{\tilde{v}_d}{\tilde{t}} \\ \frac{\tilde{v}_q}{\tilde{v}_d} & 1 & \frac{\tilde{v}_q}{\tilde{t}} \\ \frac{\tilde{t}}{\tilde{v}_d} & \frac{\tilde{t}}{\tilde{v}_q} & 1 \end{bmatrix}^{-1} \tag{3.43}$$

Similar to the procedure that was presented in details for active rectifier, required transfer functions for decoupling procedure based on Eqn. (3.43) are calculated one by one using the block diagram plot represented in Fig 3.13. by finding the direct and loop paths and formulizing the transfer function into standard form of a feedback system or by using the Mason's rule [47]. Resulting transfer functions are represented in the form of matrix T_1 and T_2 in Eqn. (3.44), (3.45). As it is shown, the dynamics of the controller C and dynamics of the mechanical load Y_L are coupled with the unterminated dynamics of the machine and are presented in matrices T_1 and T_2. However, by calculating the inverse matrix and multiplication of the two matrices the resulting matrix of transfer functions that is represented in Eqn. (3.46) excludes the dynamic couplings of the load and source and is just representing the dynamics of the PM machine itself. This is an important aspect of the study of the machine since in the case when the machine is operated with a controller on electrical side and load on the mechanical shaft, the dynamics of the load and source are inherently coupled with the dynamics of the machine and without applying the decoupling procedure the directly measured dynamics are not going to represent the true dynamics of the machine. However, after the decoupling is performed true dynamics of the device under test is calculated.

$$\mathrm{T}_1 = \begin{bmatrix} \frac{G_d}{CG_q - Y_L Z_c + 1} & -\frac{G_q}{Y_L Z_o - 1} & \frac{Z_o}{CG_q + 1} \\ Y_{\mathrm{dd}} + \frac{-CG_d Y_{\mathrm{dq}} + G_d H_d Y_L}{CG_q - Y_L Z_c + 1} & Y_{\mathrm{dq}} + \frac{-G_q H_d Y_L}{Y_L Z_o - 1} & H_d + \frac{-CY_{\mathrm{dq}} Z_o}{CG_q + 1} \\ Y_{\mathrm{qd}} + \frac{-CG_d Y_{\mathrm{qq}} + G_d H_q Y_L}{CG_q - Y_L Z_c + 1} & Y_{\mathrm{qq}} + \frac{-G_q H_q Y_L}{Y_L Z_o - 1} & H_q + \frac{-CY_{\mathrm{qq}} Z_o}{CG_q + 1} \end{bmatrix} \tag{3.44}$$

$$\mathrm{T}_2 = \begin{bmatrix} 1 & 0 & 0 \\ -\frac{CG_d}{CG_q - Y_L Z_o + 1} & 1 & -\frac{CZ_o}{CG_q + 1} \\ \frac{G_d Y_L}{CG_q - Y_L Z_o + 1} & -\frac{G_q Y_L}{Y_L Z_o - 1} & 1 \end{bmatrix}^{-1} \tag{3.45}$$

$$\mathrm{T}_1 . \mathrm{T}_2 = \begin{bmatrix} G_d & G_q & Z_o \\ Y_{dd} & Y_{dq} & H_d \\ Y_{qd} & Y_{qq} & H_q \end{bmatrix} \tag{3.46}$$

As it is shown in this part, dynamics related to the controller and the mechanical load, appear in the calculated transfer functions of system, however, all the dynamics of the load and source controller are successfully decoupled. These unterminated transfer functions carry a lot of useful information that can be incorporated to study the stability of the system in both electrical and mechanical terminals or for proper design of the system's controller. Similar studies have been demonstrated on power converters in the past [50]–[52] however intuitive experimental implementation of the study on electrical machines requires to be discovered.

3.5 Time-Domain Verification of TBM Model

In order to demonstrate the example case of using this methodology in simulation, developed Terminal Behavioral Model is compared to the dynamic model of the machine and time domain comparison of the two models in the case of a mechanical load change is obtained. Simulink model for comparing the time domain response of the unterminated model and time domain response of the dynamic model has been prepared and used to validate the response of the TBM study. Results of this comparison is demonstrated in Fig. 3.15 -Fig. 3.17. PMSM Parameters used for this initial model verification Rs=0.4 Ω, Ld=0.0031 H, Lq=0.0032 H, J=0.0015 kg m^2, flux=0.170 Wb, p=2 (pole pairs), V_{rms} = 200 V, Tm = 1 Nm.

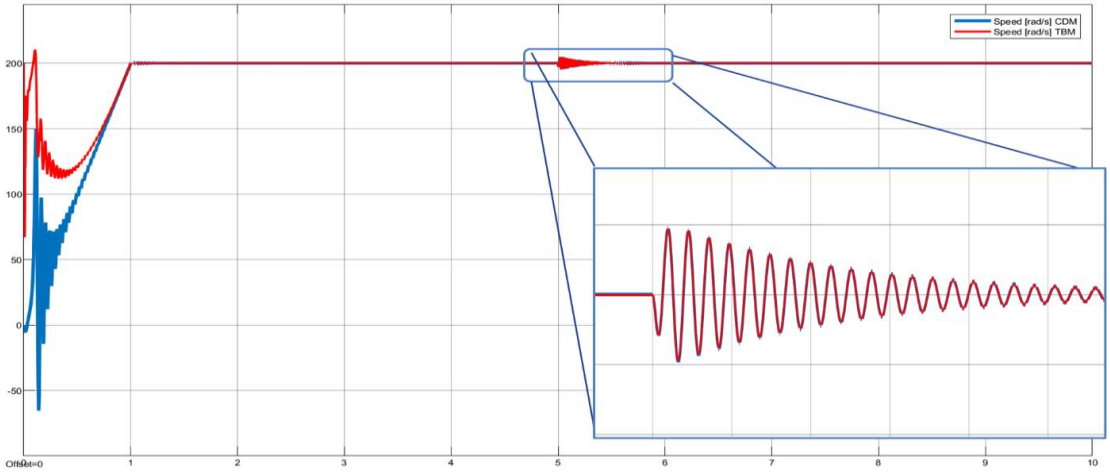

Figure 3.15: Speed response [rad/s] comparison between conventional dynamic and Terminal Behavioral Model

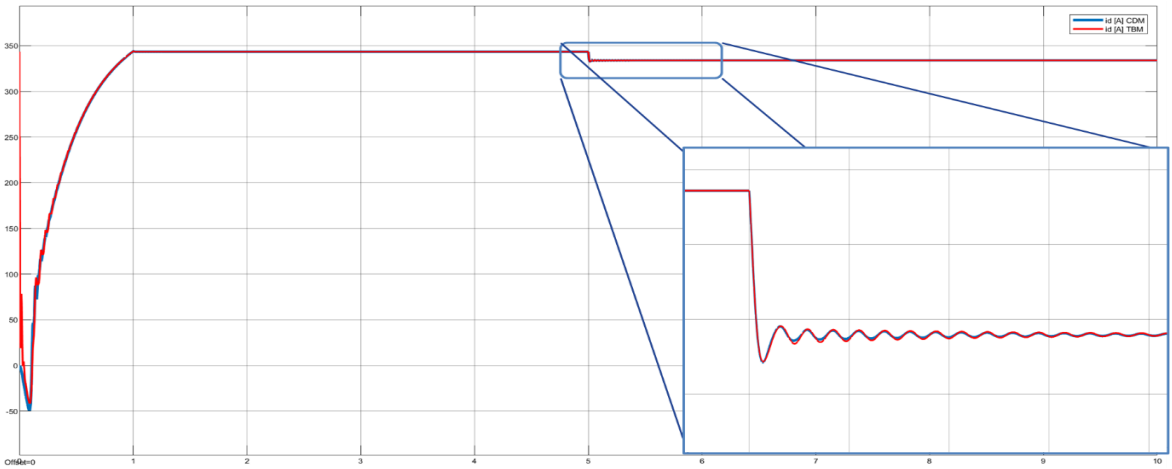

Figure 3.16: Id current response [A] comparison between conventional dynamic and Terminal Behavioral Model

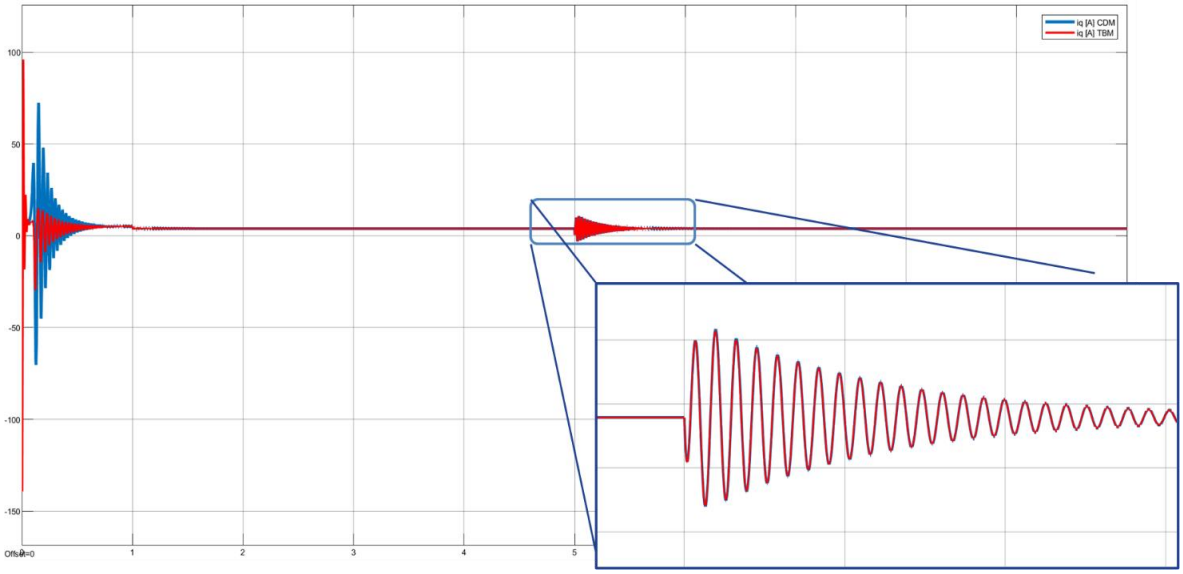

Figure 3.17: Iq current response comparison between conventional dynamic and Terminal Behavioral Model

As it is observed from the Fig. 3.15 -Fig. 3.17 the response of the dynamic model of the machine (CDM) in the case of step change in the mechanical load is very similar to the response of the resulting unterminated model of the machine at t=5sec. Since calculations related to the transfer functions required to TBM calculations are done at the same operating point as the CDM model at t=5sec, resulting responses from the models are similar however by comparing the response of the TBM and CDM model at the startup from Fig. 3.15 -Fig. 3.17 we can see that the results related it the TBM models doesn't not accurately describe the response of the machine. Reasoning for this phenomenon is the

nonlinear nature CDM of the model. Linearization of such nonlinear model at different operating point would result in different response of the model. This is why the resulting models have different response in the startup transient but are similar at t=5 sec transient.

3.6 Frequency-Domain TBM Model Validation

For TBM model frequency-domain validation, first the differential equations are linearized and the linearized form is used to develop the state space model of the machine similar to demonstration shown in Chapter 2. By transforming the state space model of the machine to the Laplace domain, SISO transfer functions of the machine is developed based on analysis performed in Chapter 2. This transfer functions can be used to validate the TBM in frequency domain since similar to TBM, this model also only includes the decoupled dynamics of the machine. Mathematical demonstration of these transfer functions is demonstrated in Eqn. (3.24). Following figures shows bode-plot comparison between the SISO transfer functions derived from the state space model and the decoupled transfer functions from TBM. Mathematical form of SISO transfer functions derived from state space model are represented in Eqn. 45-53.

$$Ydq = -\frac{2\left(3\,L_d\,i_{q0}\,{p_m}^2\,\phi_f - \sigma_5 + 3\,{L_d}^2\,i_{d0}\,i_{q0}\,{p_m}^2 - 4\,L_d\,R_m\,\omega_0\,p_m + 4\,J_m\,L_d\,\omega_0\,p_m\,s - \sigma_2\right)}{\sigma_1} \tag{3.47}$$

$$Gdd = -\frac{6\left(i_{d0}\,\omega_0\,{L_d}^2\,{p_m}^2 - i_{d0}\,\omega_0\,L_d\,L_q\,{p_m}^2 - 2\,i_{q0}\,s\,L_d\,L_q\,p_m + \omega_0\,\phi_f\,L_d\,{p_m}^2 - 2\,R_s\,i_{q0}\,L_d\,p_m + 2\,i_{q0}\,s\,{L_q}^2\,p_m + 2\,R_s\,i_{q0}\,L_q\,p_m\right)}{\sigma_1} \tag{3.48}$$

$$Ydq = \frac{2\left(\sigma_5 - 3\,{L_q}^2\,i_{d0}\,i_{q0}\,{p_m}^2 - 4\,L_q\,R_m\,\omega_0\,p_m + 4\,J_m\,L_q\,\omega_0\,p_m\,s + \sigma_2\right)}{\sigma_1} \tag{3.49}$$

$$Yqq = -\frac{2\left(8\,R_m\,R_s - 8\,J_m\,R_s\,s + 8\,L_d\,R_m\,s - 3\,{L_q}^2\,{i_{q0}}^2\,{p_m}^2 - 8\,J_m\,L_d\,s^2 + 3\,L_d\,L_q\,{i_{q0}}^2\,{p_m}^2\right)}{\sigma_1} \tag{3.50}$$

$$Gdq = \frac{6\left(2\,R_s\,p_m\,\phi_f + \sigma_4 - {L_q}^2\,i_{q0}\,\omega_0\,{p_m}^2 + \sigma_7 - 2\,L_q\,R_s\,i_{d0}\,p_m + \sigma_6 - 2\,L_d\,L_q\,i_{d0}\,p_m\,s + \sigma_3\right)}{\sigma_1} \tag{3.51}$$

$$Hdd = \frac{4\,L_q\left(\omega_0\,{p_m}^2\,\phi_f - 2\,R_s\,i_{q0}\,p_m + L_d\,i_{d0}\,\omega_0\,{p_m}^2 - 2\,L_q\,i_{q0}\,p_m\,s\right)}{\sigma_1} \tag{3.52}$$

$$Hqd = \frac{4\left(2\,R_s\,p_m\,\phi_f + \sigma_4 + \sigma_7 + \sigma_6 + \sigma_3\right)}{\sigma_1} \tag{3.53}$$

$$Zdd = -\frac{4\left(4\,{R_s}^2 + 4\,L_d\,R_s\,s + 4\,L_q\,R_s\,s + 4\,L_d\,L_q\,s^2 + L_d\,L_q\,{\omega_0}^2\,{p_m}^2\right)}{\sigma_1} \tag{3.54}$$

$$Ydd = \frac{2\left(3\,{p_m}^2\,{\phi_f}^2 - 8\,R_m\,R_s + 8\,J_m\,R_s\,s - 8\,L_q\,R_m\,s + 3\,L_d{}^2\,{i_{d0}}^2\,{p_m}^2 + 8\,J_m\,L_q\,s^2 + 6\,L_d\,i_{d0}\,{p_m}^2\,\phi_f - 3\,L_q\,i_{d0}\,{p_m}^2\,\phi_f - 3\,L_d\,L_q\,{i_{d0}}^2\,{p_m}^2\right)}{\sigma_1} \tag{3.55}$$

While $\sigma_1, \sigma_2, \sigma_3, \sigma_4, \sigma_5$ are defined as follow.

$$\begin{aligned}\sigma_1 = {} & 3\,{I_d}^2\,{L_d}^3\,p^2\,s - 3\,{I_d}^2\,{L_d}^2\,L_q\,p^2\,s + 3\,{I_d}^2\,{L_d}^2\,R_s\,p^2 - 3\,{I_d}^2\,L_d\,L_q\,R_s\,p^2 + 6\,I_d\,I_q\,{L_d}^2\,L_q\,\omega\,p^3 \\ & - 6\,I_d\,I_q\,L_d\,{L_q}^2\,\omega\,p^3 + 6\,I_d\,{L_d}^2\,p^2\,\phi_f\,s - 3\,I_d\,L_d\,L_q\,p^2\,\phi_f\,s + 6\,I_d\,L_d\,R_s\,p^2\,\phi_f \\ & - 3\,I_d\,L_q\,R_s\,p^2\,\phi_f - 3\,{I_q}^2\,L_d\,{L_q}^2\,p^2\,s - 3\,{I_q}^2\,L_d\,L_q\,R_s\,p^2 + 3\,{I_q}^2\,{L_q}^3\,p^2\,s \\ & + 3\,{I_q}^2\,{L_q}^2\,R_s\,p^2 + 6\,I_q\,L_d\,L_q\,\omega\,p^3\,\phi_f - 3\,I_q\,{L_q}^2\,\omega\,p^3\,\phi_f + 2\,J\,L_d\,L_q\,\omega^2\,p^2\,s \\ & + 2\,B_m\,L_d\,L_q\,\omega^2\,p^2 + 2\,J\,L_d\,L_q\,s^3 + 2\,B_m\,L_d\,L_q\,s^2 + 2\,J\,L_d\,R_s\,s^2 + 2\,B_m\,L_d\,R_s\,s \\ & + 3\,L_d\,p^2\,{\phi_f}^2\,s + 2\,J\,L_q\,R_s\,s^2 + 2\,B_m\,L_q\,R_s\,s + 2\,J\,{R_s}^2\,s + 2\,B_m\,{R_s}^2 + 3\,R_s\,p^2\,{\phi_f}^2\end{aligned}$$

$$\sigma_2 = 3 I_d I_q L_d L_q p^2$$

$$\sigma_3 = I_d L_d^2 p s$$

$$\sigma_4 = I_q L_d L_q \omega p^2$$

$$\sigma_5 = 3 I_q L_q p^2 \phi_f$$

It can be seen that SISO transfer functions derived from the state space model consists of many terms related to the internal parameters of the machine such as d and q axis inductance, stator resistance, inertia, flux, number of poles and operating point conditions for state variables. By substituting the internal parameter with their values and also substituting the values of the operating point of the machine, numerical form of SISO transfer functions is formed. These transfer functions can be compared with single input single output linear time invariant (SISO-LTI) transfer functions that are derived from the decoupling procedures of TBM method. As it was discussed in previous parts dynamics related to the controller can be completely eliminated from the TBM transfer functions resulting into the decoupled model that only includes the dynamics related to the PMSM machine. To demonstrate the effect of the controller's dynamics on the direct measurement frequency responses from the terminals of the machine a simulation example is prepared. In this example, the PM machine is simulated with different values for the speed

controller's proportional coefficient K_p. Fig. 3.18 shows the transfer functions related to this experiment. The difference in the direct dynamics in the case of difference in the controller can be observed in the corresponding transfer functions however regardless of the difference in the value of the controller, it is shown that with successful decoupling of the dynamics from the TBM transfer functions, resulting unterminated transfer functions (TBM Decoupled) are identical to the transfer functions related to the state space of the PM machine.

	$K_p = 10$	$K_p = 20$
Gdd	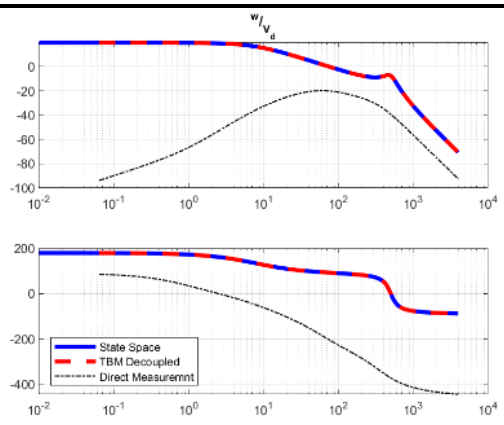 a.1	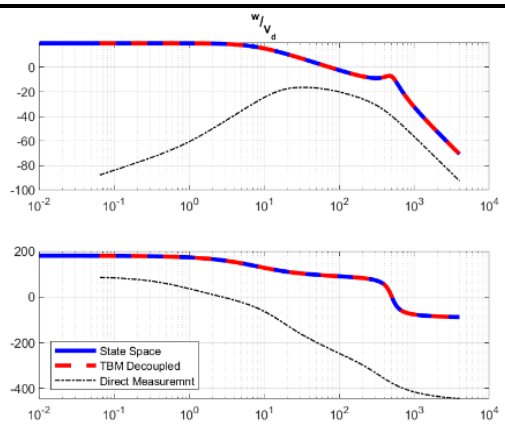 a.2
Gdq	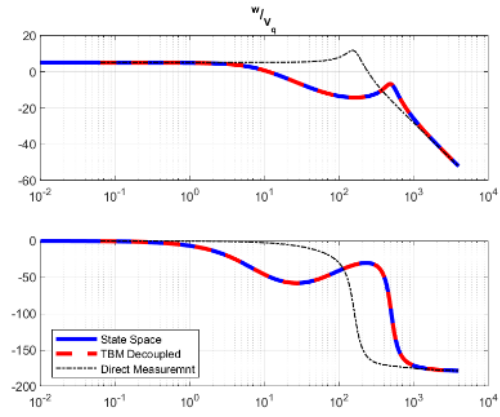 b.1	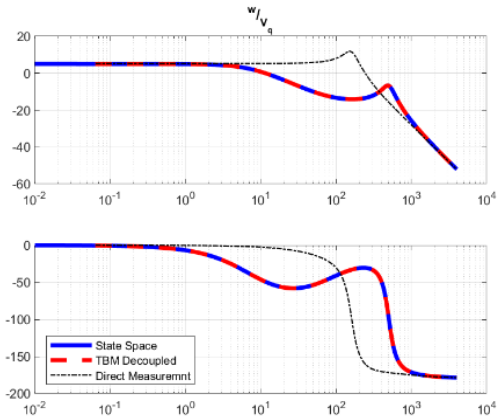 b.2

Hdd	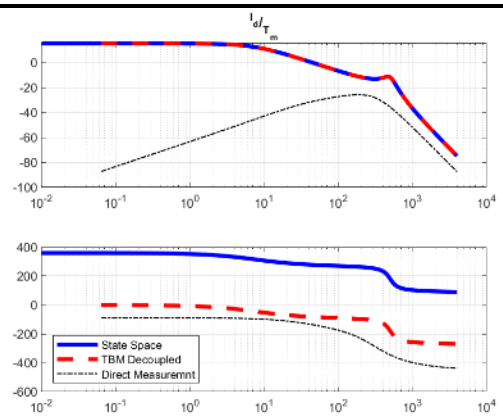 c.1	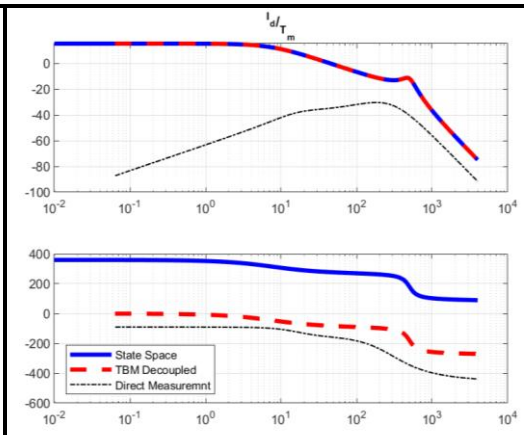 c.2
Hqd	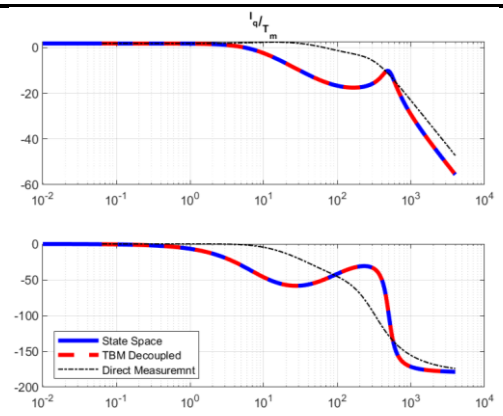 d.1	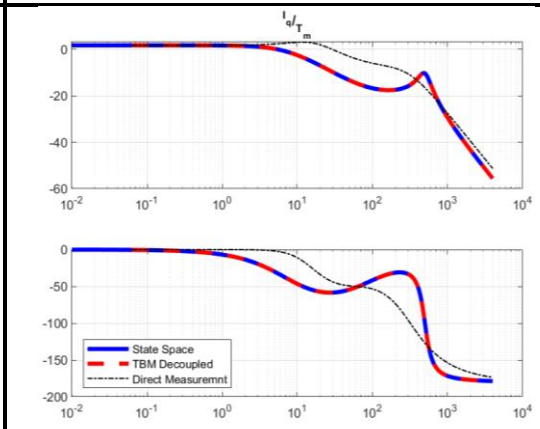 d.2
Ydd	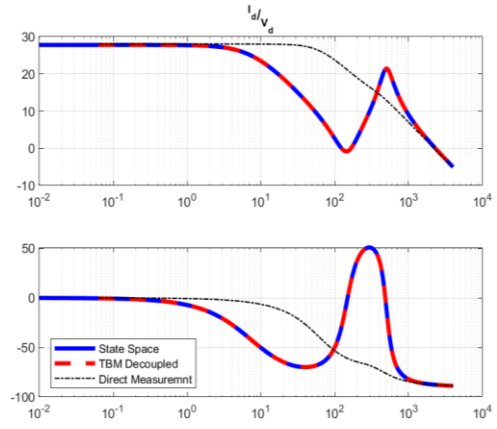 e.1	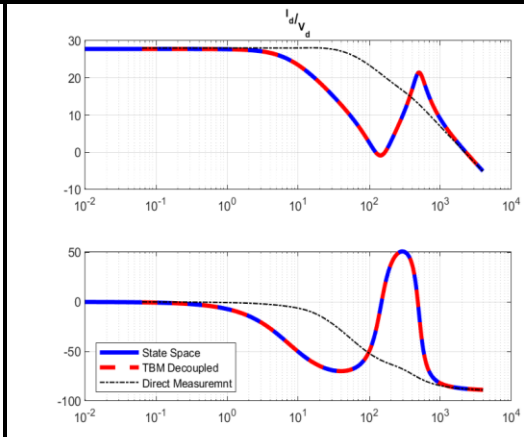 e.2

Yqd	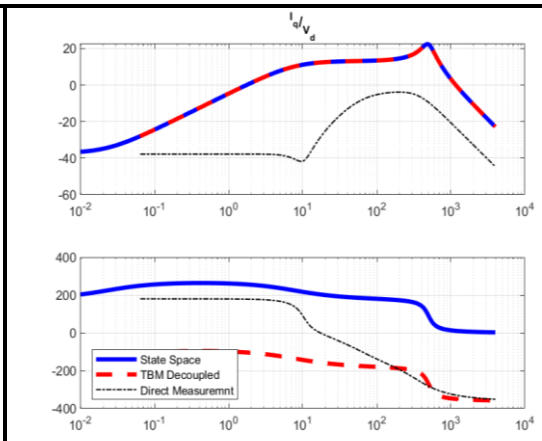 f.1	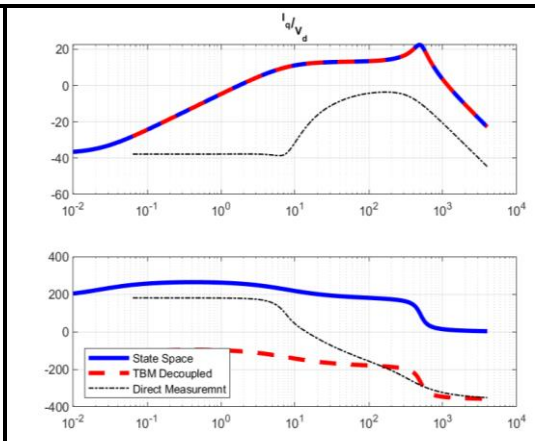 f.2
Ydq	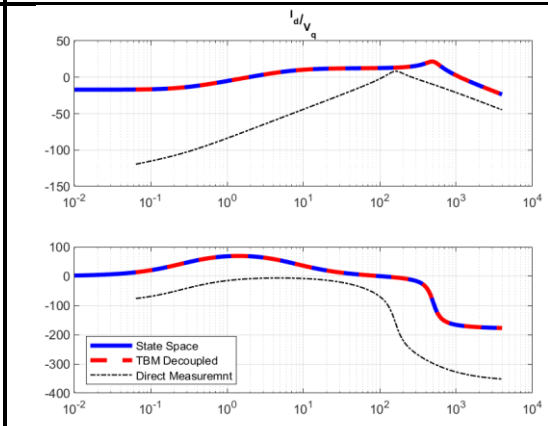 g.1	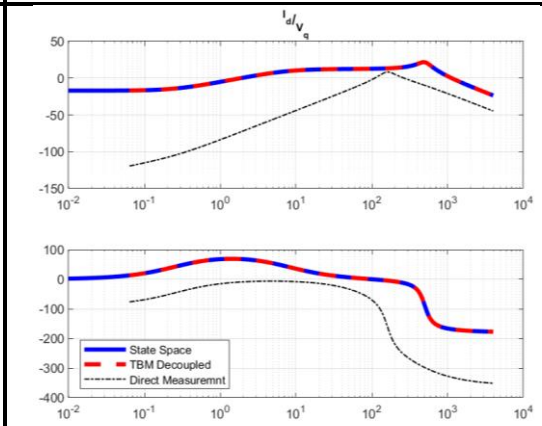 g.2
Yqq	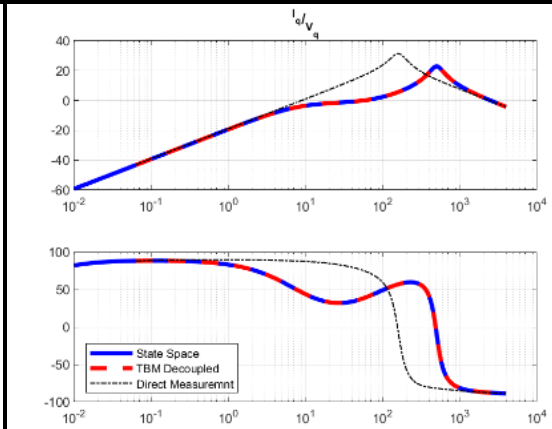 h.1	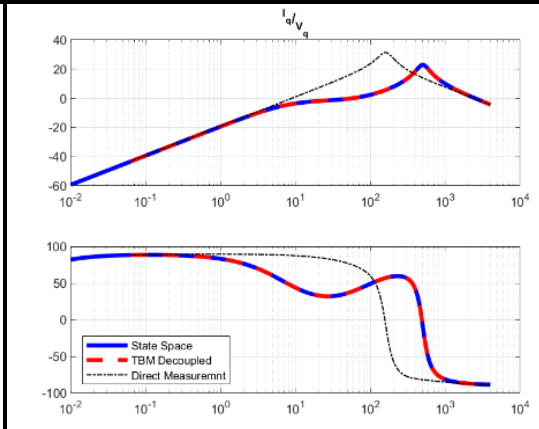 h.2

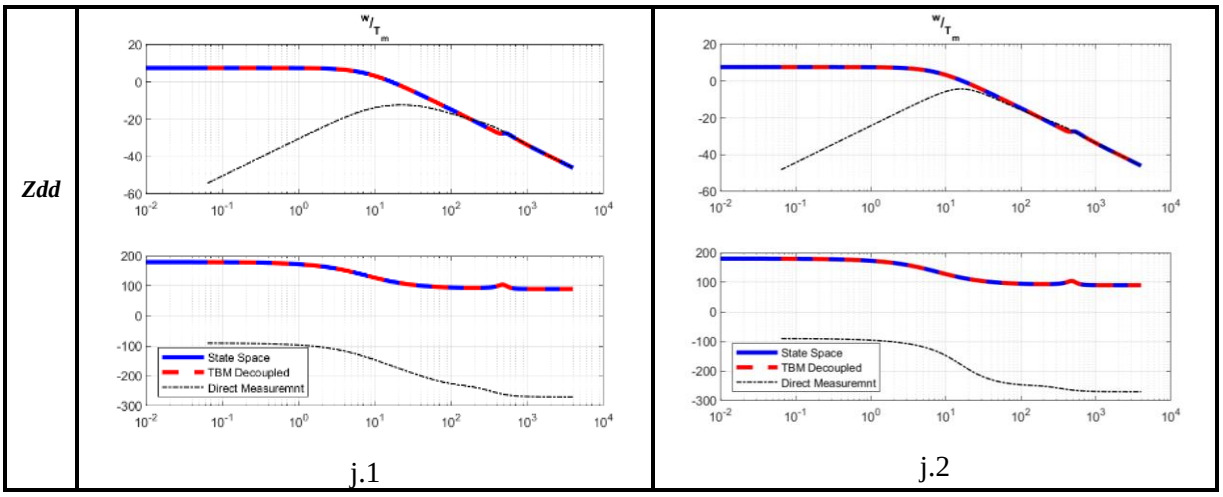

Figure 3.18: TBM transfer functions comparison with State Space and direct simulation measurements

In this chapter background knowledge about terminal behavioral models was demonstrated. Decoupling procedure was discussed in details and mathematical examples of this procedure for decoupling the dynamics of the load and source in the case of active rectifier and PM machine was demonstrated. Additionally, simulation examples showing the time domain comparison of the resulting TBM model and conventional dynamic models was shown. Finally, simulation results demonstrating the effect of the controller's coefficient on the observed dynamics and decoupled models was demonstrated. Using the intuitive mathematical demonstration discussed in this chapter, experimental verification of this modeling method is discussed in the next chapter.

Chapter 4

Introduction

In this section, the experimental implementation and verification of the terminal behavioral modeling of Permanent Magnet Synchronous Machine (PMSM) is presented. Using conventional standard test procedures, key parameters required for modeling and simulation are measured, and resulting parameters are then used to confirm the measurement capabilities of the developed test setup. Additionally, this chapter presents the implementation of the controller and measurement requirements by real-time emulators, Hardware-In-The-Loop and Power-Hardware-In-The-Loop. Revisions related to the mechanical shaft coupler and effect of this changes are also presented in this chapter.

4.1 Standstill Parameter Measurements for PMSM

4.1.1 Stator Resistance Measurement:

Different procedures for the measurement of Permanent Magnet (PM) machine parameters are demonstrated in the literature [53]–[56] among which simple standstill procedures are chosen to identify the key machine parameters needed for both simulation models and verification purposes. Value of stator resistance in the PMSM motor under study is very small in comparison to most of motors with the same power rating. Due to small values of the stator resistance simple measurement of the resistance using a multimeter is not possible. To measure the small values of stator winding resistance of PMSM, a current source was connected to terminals of the motor and an extra voltage sensing set of wires were soldered near the terminal of the motor to avoid the effect of voltage drop on probe's point of connection. Fig. 4.1 shows the configuration for one measurement set. Other measurements are repeated in similar manner by replacing connections to other phases of the machine. In this measurements Fluke 8808A was used that can cover up to 5 ½ digits of accuracy range. Using the configuration of connecting two phases of PMSM to the current source and measuring the value of the current and voltage at the motor terminal, it is possible to accurately measure the stator resistance in

the case of small values for stator resistance. Table 4.1 shows three sets of measurements and calculations that were obtained by experiments on three line-to-line configurations.

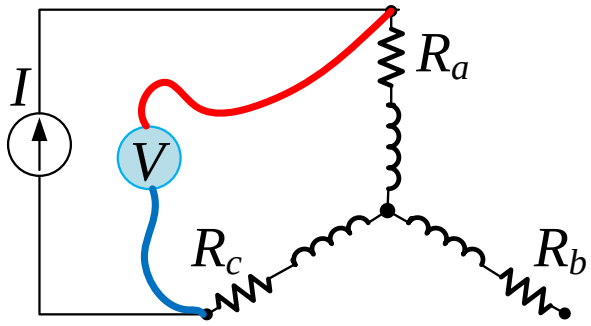

Figure 4.1: Measurements and calculations related to the PMSM stator resistance

Measurement		Calculated
I [A]	V [V]	Ra+Rb [Ω]
5.5033	0.43515	0.079071
5.4698	0.43241	0.079054
5.5129	0.43519	0.07894
5.4782	0.43292	0.079026
5.4903	0.43409	0.079065

Measurement		Calculated
I [A]	V [V]	Rb+Rc [Ω]
5.2778	0.41736	0.07907
5.2157	0.41057	0.078718
5.1818	0.40926	0.07898
5.1890	0.40991	0.078996
5.2275	0.41263	0.078934

Measurement		Calculated
I [A]	V [V]	Rc+Ra[Ω]
5.4259	0.42915	0.079093
5.4713	0.43317	0.079171
5.4528	0.43168	0.079167
5.4343	0.43014	0.079153
5.4423	0.43080	0.079158

Table 4.1: Measurements and calculations related to the PMSM stator resistance

Measurements related to each line-to-line measurement configuration are repeated and average value is considered for modeling and simulation in this study.

4.1.2 PMSM L_d Measurement

Standstill test procedure for identifying the inductances of PM machines are demonstrated in [57] The inductances of PM machines with surface mounted magnets are almost equal in d and q axis, because the permeability of surface mounted magnets is the same in all positions. When the rotor is aligned with the phase A winding, L_d can be derived from the measured equivalent inductance of the circuit, as shown in Fig. 4.2. In this experiment Venable Instruments 3225 2-channel frequency response analyzer (FRA) was used for sweeping the frequency range and acquiring the response from the setup during the test. This device's structure is demonstrated by the elements encircled by the red-line

boundary in the same figure. The procedure for measuring the impedance of passive components using Venable FRA is done on the basis of supplying a perturbation signal using this device and using the two other channels to measure the dynamic response of the model when a sweep of the desired frequency range is performed by the device. After connecting phase a to the positive and phase b and c to the negative side of the voltage source, d-axis alignment is achieved. In this position the rotor position is locked and the voltage source is removed. By using a 1 Ω standard resistance, the value of the current is recorded using channel 2 of Venable FRA. Channel 1 is used to measure the voltage which is applied to the setup. Impedance of the *d-axis* is calculated using the ratio of the measurements on two FRA's channels while sweeping across the frequency range.

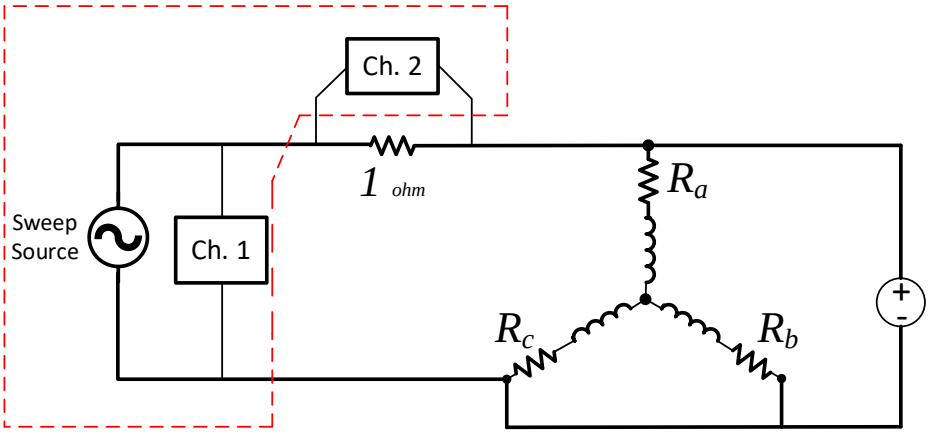

Figure 4.2: Connections configuration for L_d measurement

After performing the measurement, the resulting frequency response was recorded and post-processed with MATLAB software. Using MATLAB, a transfer function was fitted to the measurement frequency response values as it is shown in Fig. 4.3. Mathematical form of the fitted transfer function is shown in Eqn. (4.1). In this case the fitted model's order is selected to be the 3rd order, however in case that simplified model is required only the coefficient of 0.000679 which is observed in the fitted transfer function is demonstrating the equivalent observed inductance of the circuit.

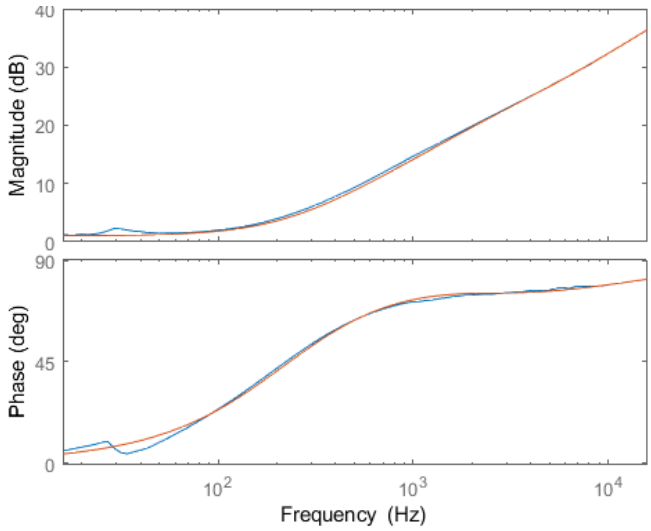

Figure 4.3: D-axis impedance, measured frequency response (blue) and MATLAB-fitted transfer function Z_d (red - curve fit)

(4.1)

$$Zd = \frac{0.000679s^3 - 24.35s^2 - 1.315e06s - 1.785e09}{s^2 - 5.34e04s - 1.583e09}$$

By considering the physical angle of the windings of phase b and c, the calculated value should be multiplied by 2/3 to obtain the d axis inductance of the machine using this procedure.

4.1.3 PMSM L_q Measurement

For aligning with *q-axis*, phase *a* is disconnected from the source and phase *b* and *c* are connected to the positive and negative side of the voltage source similar to Fig.4.4. With this configuration, *q*-axis alignment is achieved. Similar to the previous part, position of the rotor location is locked and the voltage source is connected as Fig. 4.4. By using a 1 Ω standard resistance, the value of the current is recorded using the channel 2 of Venable FRA. Channel 1 is used to measure the voltage which is applied to the setup.

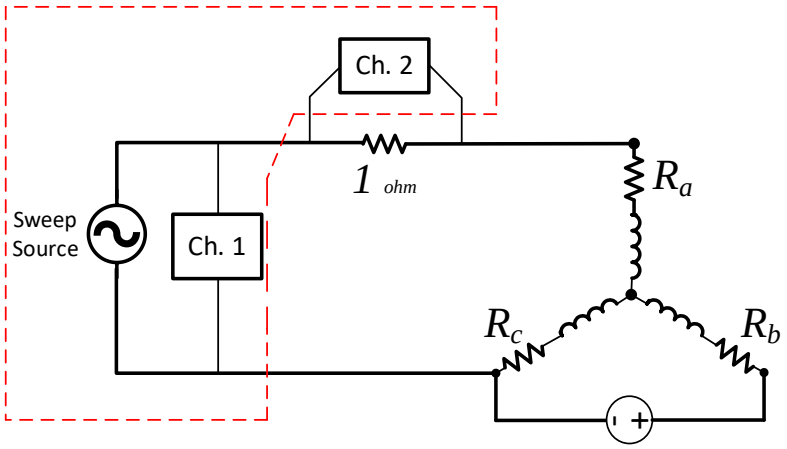

Figure 4.4: Connections configuration for L_q measurement

After performing the measurement, the resulting frequency response was recorded and post-processed with the MATLAB software. Using MATLAB, a transfer function was fitted to the measurement frequency response values leading to the form shown in Eqn. 4.2. Fig. 4.5 illustrates a third order TF Zq curve-fitted and overlaid with the frequency response plot.

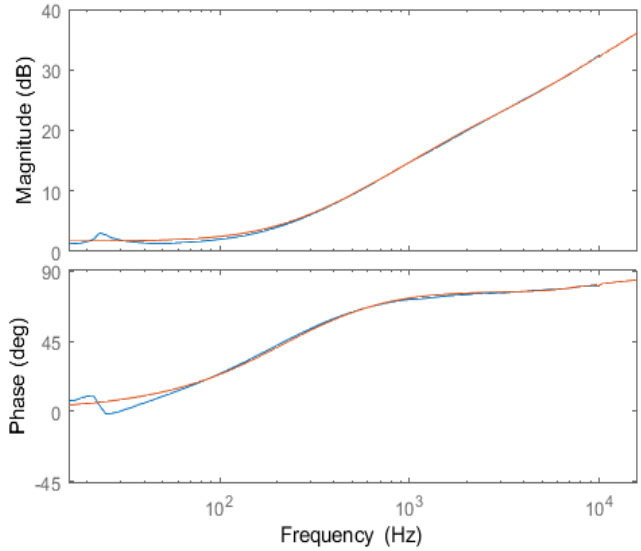

Figure 4.5: D-axis Impedance, measured frequency response (Blue) and MATLAB-fitted transfer function Z_q (Red - curve fit)

$$\mathrm{Zq} = \frac{0.000623\mathrm{s}^3 + 12.15\mathrm{s}^2 - 3.507\mathrm{e}05\mathrm{s} - 5.321\mathrm{e}08}{\mathrm{s}^2 + 7820\mathrm{s} - 4.863\mathrm{e}08} \tag{4.2}$$

By considering the physical angle of the windings of phase b and c, the calculated value should be multiplied by 2/3 to obtain the *q*-axis inductance of the machine using this procedure.

The type of the machine used in this study has permanent magnet on the surface of the rotor and since the permeability of the permanent magnets are almost the same as the permeability of the air as Eqn. (4.3), the measured inductances of the machine in d and q axis are very similar.

$$\mu_{\mathrm{PM}} \approx \mu_{\mathrm{air}} \rightarrow \mathrm{L_d} \approx \mathrm{L_q} \tag{4.3}$$

4.2 Pole Numbers Measurement

We can calculate number of poles with a voltage source and manually turning the motor while the terminals are connected to a voltage source. In this method we connect the phase a wire to the positive potential (+) and phase b and c to negative potential (-) of the voltage source. Value of the voltage source is selected to keep the current passing from the phase under the current rating of the motor and the current is low enough that makes it possible for the rotor position to be adjusted manually. Fig. 4.6 shows the connection of the motor to the voltage source.

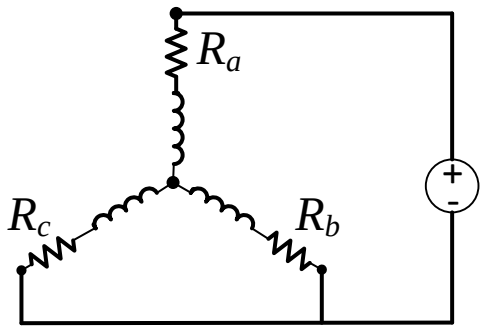

Figure 4.6: Motor connections for pole number estimation

After connecting the motor to the source with desired voltage, the position of the shaft is manually turned slowly for one full rotation. While turning, the rotor position

would become stable at some positions of the shaft. Number of the stable positions for the shaft is equal to the number of pole pairs of the motor. In this case Fig. 4.7 shows the stable positions of the shaft. On this basis, the motor has 3 pole pairs or 6 poles.

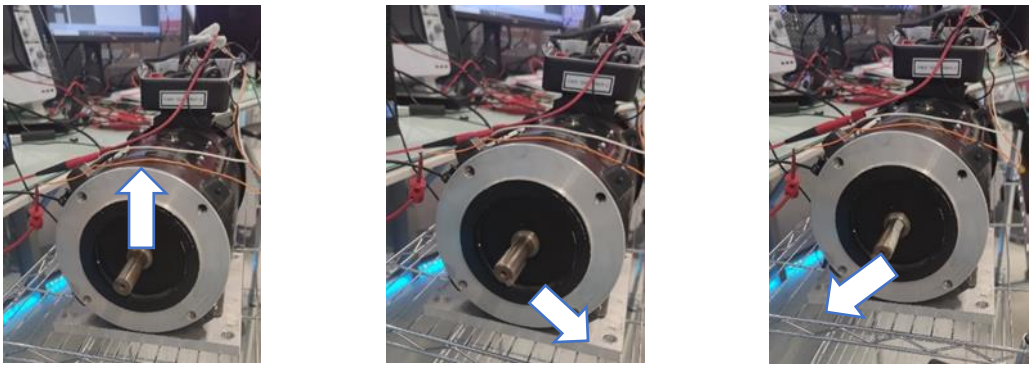

(a) *(b)* *(c)*

Figure 4.7: Rotor position alignment for pole number calculation

For another method, The PMSM motor is coupled with another motor which in this case was a Line-Start Permanent Magnet Motor with known number of poles. After connecting this motor to the power source with known line frequency and measuring the frequency of the generated voltage on the PMSM terminals, it is possible to calculate the ratio between the number of poles of the two motors. Fig. 4.8 shows the coupled setup containing two coupled motors and table below shows the measured frequencies and their ratio obtained with this test.

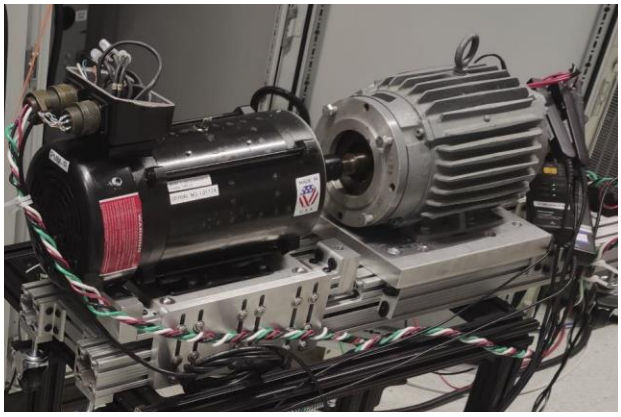

Figure 4.8: Coupled motor test for pole number calculation

LS-PMSM Frequency	PMSM Frequency	Ratio
60	90	$\frac{2}{3}$
65	97.5	$\frac{2}{3}$
70	105	$\frac{2}{3}$
75	112.5	$\frac{2}{3}$

Table 4.2: Measurements related to the PMSM pole number identification

In this experiment, the line-start permanent magnet synchronous machine (LS-PMSM) motor has 2 pole pairs (4 poles) and the ration for voltage frequencies measured on the terminals of the two machines was 2/3 in different tests. This shows that the number of poles of the PMSM should be $\frac{3}{2} * 2$ or 3 poles pairs.

4.3 Back-EMF Constant Measurement

Back-EMF is one other important parameter of the machine that is required for both modeling and simulation and for control of the machine. This parameter can be measured by rotating the machine using another motor and measuring the no load line voltage of the machine under test. This measurement results in the calculation of the ratio between the speed and the voltage that is generated across the windings of the machine. In this experiment, PM machine was coupled with a LSPMSM. Throughout this experiment LSPM machine is supplied with 70Hz supply. Considering that this machine is a 2-pole pair machine while the PM machine is a 3-pole pair machine, line frequency of the open circuit PM machine while being driven from LSPM machine will become 105Hz. In addition, line to line voltage of the PM machine at this experiment is measured to be 229.1 V peak to peak. Fig. 4.9 represents the measurements related to this experiment. From the top, first three channels are representing the LSPMSM currents while last two channels are representing the PM machine line to line voltages.

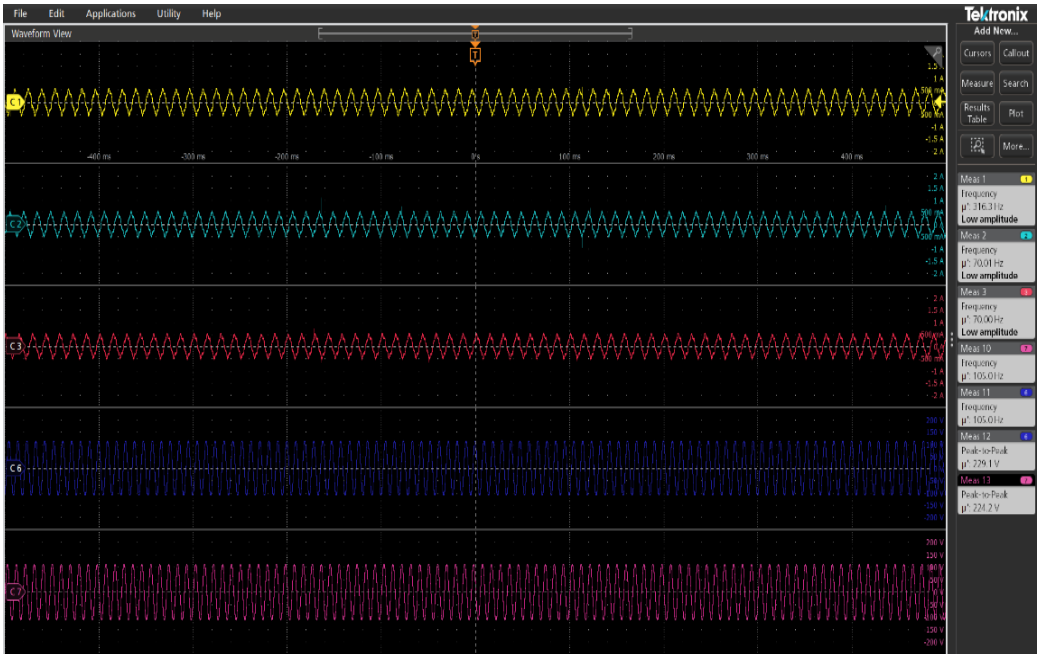

Figure 4.9: Measurements related to Back-EMF

Using the Eqn. (4.4) the Back-EMF parameter of the machine is calculated as following.

$$k_{e_{-\mathrm{ph}}} = \frac{V_{\mathrm{pk}}}{\sqrt{3}\cdot\omega_{\mathrm{el}}} = \frac{V_{\mathrm{pk-pk}}}{2\sqrt{3}\cdot\omega_{\mathrm{el}}} = \frac{229.1}{2\sqrt{3}\cdot 210\,\pi} = 0.1002 \text{ (v.s/rad)} \qquad (4.4)$$

4.4 Current and Voltage Measurement Boards

Accurate measurement of voltage and current waveforms is very important in this thesis since these measurements are essential to perform TBM method. For accurate measurement of the voltage and current waveforms, measurement board that consists of individual voltage and current sensors for each phase is being used. Fig 4.10-a shows the assembled voltage and current sensor board. PCB layout of this board is shown in Fig 4.10-b. Output of both voltage and current sensors is in the form of current signals. This current signal needs to be connected to an output resistance to generate an appropriate voltage signal for ADC. This board also needs a supply of voltage in the range of +-12 to +-15.

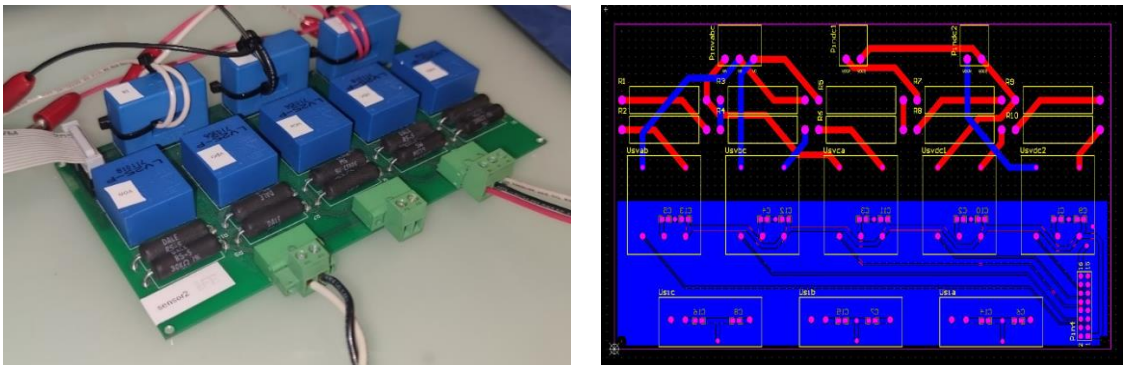

(a) (b)

Figure 4.10: (a), Assembled voltage and current sensor board.
(B), PCB layout of the sensor board

In order to supply this board and also convert the current outputs of the sensors to the voltage signal that is compatible with ADC unit inside OPAL-RT unit we modify a measurement signal-conditioning board developed by EGSTON. Fig. 4.11 shows this board. THN 20-2413 units on the board are DC-DC converters with isolated input-output that are being used to supply the sensor board shown in Fig. 4.10-a.

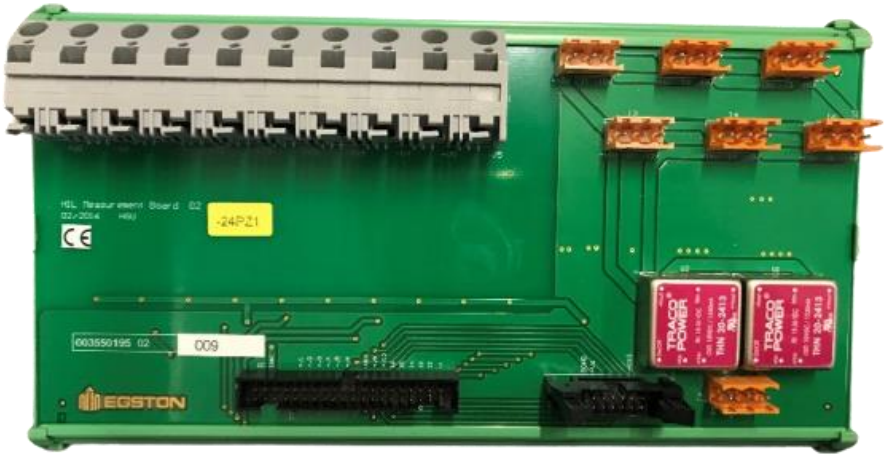

Figure 4.11: Modified EGSTON signal conditioning board (for OPAL-RT)

This board also consists of 5 differential inputs that consist of a voltage divider and a lowpass filter on each channel. DC gain of this voltage divider circuit is measured to be -32.1705 dB. Fig. 4.12-a shows the voltage divider circuit for each channel of the board.

In order to make the board compatible with resolver's signals, this voltage divider circuit has been modified. This modification, represented in Fig. 4.12-b increases the DC gain of the circuit to be suitable for small signals that are generated from the resolver and also for the torque sensor. These sensors have peak-to-peak values of less than 10 volts thus they can be directly fed to HIL for measurements and for control.

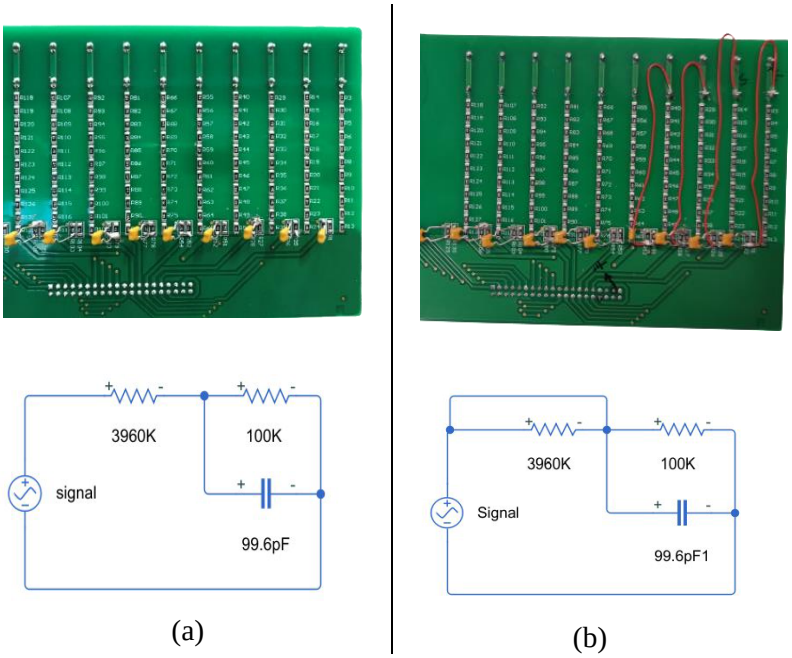

Figure 4.12 (a): Original voltage divider circuitry
(b): Modified voltage divider circuitry

Using this modified signal conditioning board, all the signals related to the voltage and currents of both machines, resolver's signal, and torque signal are fed to both control and measurements HILs using the 37-pin connector. Additionally, all of the sensor boards and measurements board circuits are organized inside a cabinet to eliminate unwanted disconnects and also to help with EMI mitigation related to the other equipment in the place where test are being done.

4.5 Common Noise Issue and Solution

After connecting the measurement board circuits to the setup in the form of Fig. 4.13 initial tests were done to ensure the validity of the measured signals. In the initial tests additional common noise was observed on the resolver signal and after an identification

and noise mitigation process the isolated voltage source was identified as the common noise issue reason in such way that substituting this source with a standalone battery pack eliminated the common mode noise propagation path. This effect was successfully mitigated using the common mode choke on the propagation path of the supply source and the sensor boards.

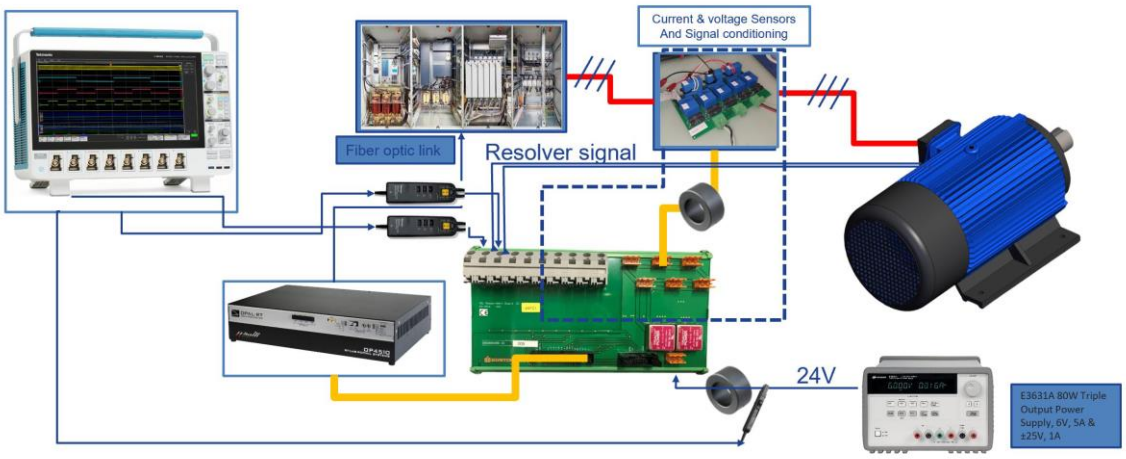

Figure 4.13 System connection for machine characterization

4.6 Accurate Speed and Rotor Position Measurement

4.6.1 Resolver Sensor

In this project having accurate values of speed and rotor position are important because they are directly needed to perform the TBM. Also having direct access to the position and speed of the rotor would make it easier to control the PMSM by simplifying the controller's structure and eliminating sensor-less estimation algorithms. The permanent magnet synchronous motor that is being used in this project is equipped with a resolver that is located at the back of the motor. This resolver is used to achieve accurate values of speed and the position of the rotor. In this part, a detailed description and principle of operation for the resolver is discussed and the method for acquiring the speed and position from the resolver signals is demonstrated. Fig. 4.14 shows the structure of a resolver.

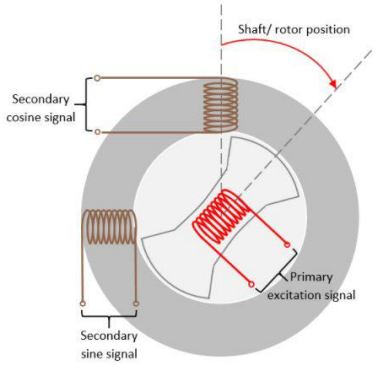

Figure 4.14: Simplified resolver's structure

The resolver consists of two orthogonally placed stator windings placed around the resolver rotor winding. Since the coupling between the primary coil and secondary coils relies on the angle of the resolver's shaft, if we supply primary excitation coil with a sinewave with relatively high frequency (in comparison to the angular frequency of the shaft of the resolver) we will have two signals on the secondary side that are modulated with the sine and cosine of angle of the rotor. Fig. 4.15-a shows the example of the excitation signal and Fig. 4.15-b and Fig. 4.15-c show the sine and cosine modulated signals that are available at the secondary side of the resolver.

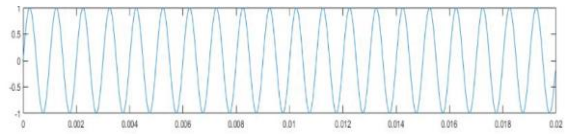

(a)

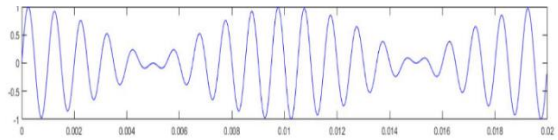

(b)

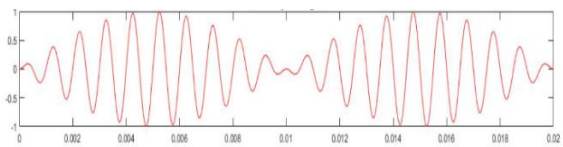

(c)

Figure 4.15 (a) Resolver's excitation signal
(b) Resolver's sine and cosine modulated output signals

Different methods have been discussed in the literature regarding acquiring the position and speed values from the resolver's signal.[58]–[60] .One of these methods is discussed hereunder. Fig. 4.16 shows the modulated Sine and Cosine signals that are coming from the resolver's secondary side.

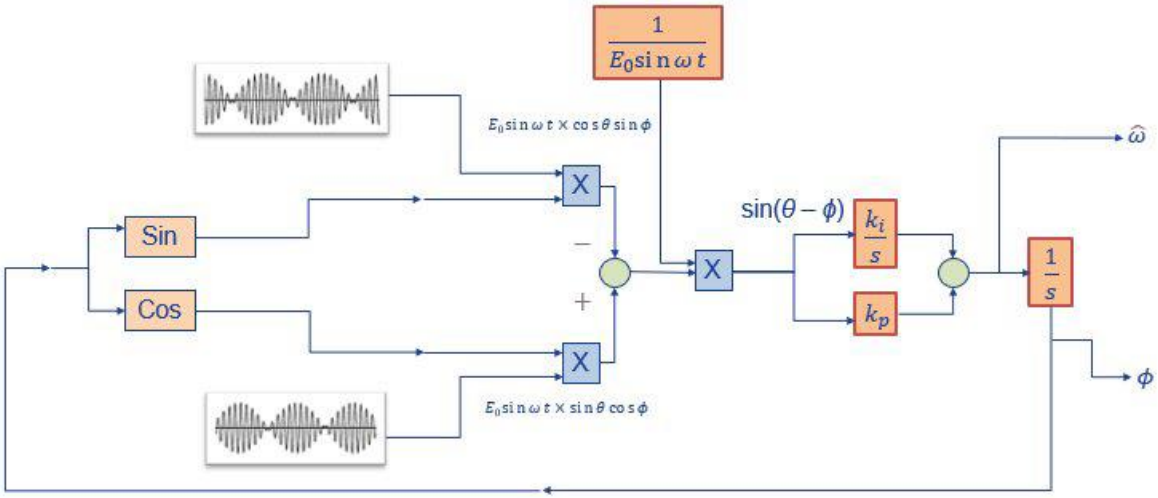

Figure 4.16: Speed and angle estimation from the resolver

This structure is very similar to the structure of a PLL. It shows the multiplication of the resolver's output signals with the sine and cosine terms that represent the estimated position of the rotor based on Eqn. (4.5).

$$\begin{aligned} & E_0 \sin(\omega t) \times \sin(\theta) \,.\, \cos(\phi) - E_0 \sin(\omega t) \times \cos(\theta) \,.\, \sin(\phi) \\ & \quad = E_0 \sin \omega t \times (\sin \theta \cos \phi - \cos \theta \sin \phi) \\ & \quad = E_0 \sin \omega t \,.\, \sin\,(\theta - \phi) \end{aligned} \tag{4.5}$$

Based on the equation above if we divide the resulting signal by the values of the excitation signal then we can achieve a signal that represents sinusoidal function of the difference of the angle of the actual rotor with estimated angle of the rotor. In the case that the estimated and real value of the position are close to one another $\sin(\theta - \phi)$ can be

approximated with $(\theta - \phi)$. In this case we can simply achieve the required bandwidth and phase margin by tuning the proportional and integral coefficients of the PLL structure. Accurate estimation of the position and angular speed of the rotor from the resolver signals is also achievable using the dedicated chips that are designed for driving the resolver's primary side and providing filtering, considering imperfections of the resolver, and analog to digital conversion. For this reason, AD2S1210 was selected to be used in this study. Figure 4.17 shows the development board for this chip as well as microcontroller board that is used to communicate with this board.

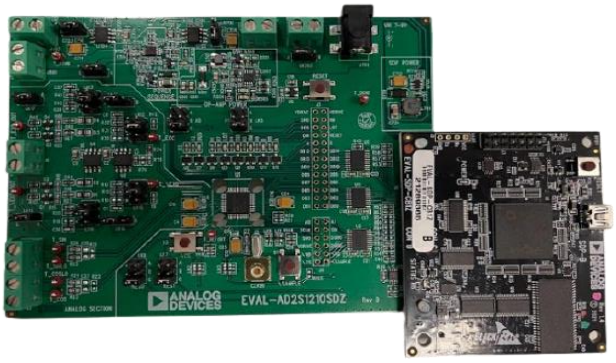

Figure 4.17: Resolver development and evaluation setup

Simplified block diagram of this board is shown in Fig. 4.18 showing the terminals, sensor connection ports as well as microcontroller and communication ports.

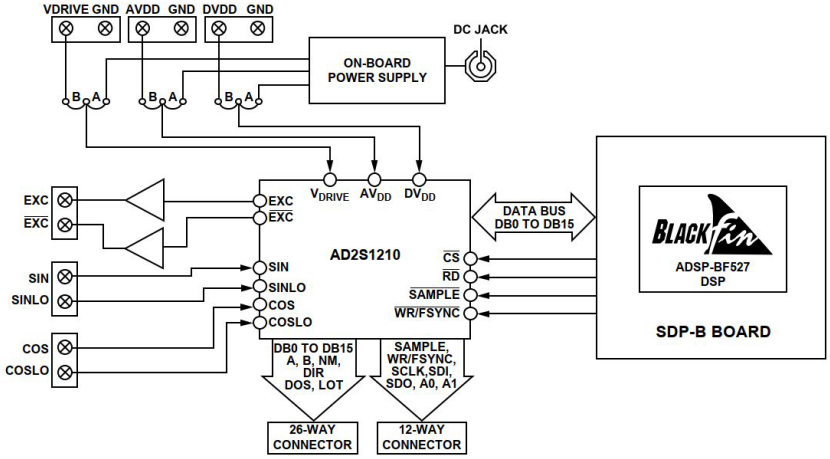

Figure 4.18: AD2S1210 Dev. board structure

Microcontroller board is also provided by a computer program that can be used for debugging purposes and the initial operation of the resolver. Since AD2S1210 board provides digital information of the speed and position of the rotor another microcontroller board was programmed to convert the digital values of the speed and position acquired from AD2S1210 to analog signals compatible with HIL. Limitations related to the loss of accuracy associated with multiple conversions of the signal were observed in this implementation and were incentive to implement a different approach for this problem. In order to resolve this issue, the PLL structure for speed and position estimation was directly deployed into the measurement HIL and non-pre-conditioned modulated signals from the resolver were directly fed to the analog input of the measurement HIL. Fig 4.19 show the implemented block diagram for real-time speed and position estimation of the machine that is used for its control. It should also be mentioned that the angle of the resolver on the shaft is not necessarily aligned with a specific phase of the machine meaning that in order to be able to control the machine properly, the offset angle of the resolver from the phase a of the machine windings should be calculated.

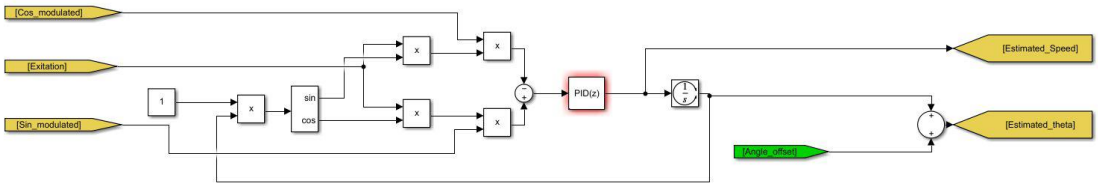

Figure 4.19: Implementation of resolver's position estimator

In order to ensure the proper calculation of the resolver's offset, this machine was driven with another machine and the offset angle of the resolver's position signal was modified gradually. While changing the position offset value inside the real-time HIL software, the *d*-*q* transformed voltages of the machine were observed. Modification of the resolver's offset was continued to achieve zero means value for the *d*-axis voltage of unloaded PM machine.

4.6.2 Encoder Sensor

Encoders are a different type of sensors used for speed and position estimation of rotary machines. Encoders are divided into two categories called incremental encoders and absolute encoders. Incremental encoders provide a series of pulses that can represent the position change of the rotary object. By using an encoder algorithm these pulses are then counted to represent the speed or position of the rotary object. This type of encoder requires initialization of the startup position since the pulses. On the other hand, absolute encoders output a digital packet of information to represent the exact location of the rotary object thus there is no need for initialization of the startup position using this type of encoders. The encoder that was used in this study was incremental type encoder with 2500 pulses per revolution. Position information acquired by the encoder was used to detect the synchronous reference frame for PM machine and transform the real-time measurements of voltage and current into *d-q* reference frame inside the measurement HIL. In this implementation RT Box 3 was used to convert digital pulses of the encoder into the real-time speed and position measurements.

4.7 Hardware Alignment

Since the setup is designed in a way that only PMSM and torque sensor have position adjustment capability, position of the induction machine (IM) is set first and then position of the sensor and PMSM are adjusted accordingly. As the first step, we try to adjust the location of IM to be parallel to the structure and vertically centered to the structure. After finding proper position, IM is tightened to the structure. *X axis* position of the motors and torque sensors are roughly adjusted so that the small slide of couplers on the shaft provides enough displacement for decoupling and coupling the shafts. In the second step, position of torque sensor is adjusted in Y and Z axis on all four legs to be aligned with the IM. In the next step couplers on the shafts are sided forward to make IM and sensor coupled. After this step, the IM is driven using V/F drive to make sure that this coupling was properly done, and no excessive vibration is observed. Finally, PMSM is aligned using the four adjustment systems that were demonstrated earlier in this thesis. After adjusting the location of all four legs of PMSM, 6 bolts that hold the PMSM structure

are tightened on each side to hold the PMSM position. As the last step the coupled system is driven using the variable frequency drive to ensure that there is no excessive vibration or noise. Fig. 4.20 shows the coupled system after the alignment is done.

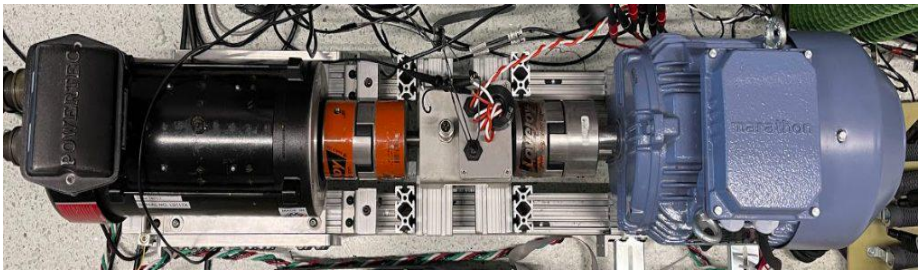

Figure 4.20 : Developed motor-generator dyno setup used for measurements

4.8 Machine Characterization Setup

The characterization setup needed for experimental verification of this project was made by combining various devices such as hardware-in-the-loop, power-hardware-in-the-loop, frequency response analyzer, voltage and current sensor boards, torque sensor, resolver and encoder and various other specially made components. Fig (4.21) shows the overall shape of the developed test setup.

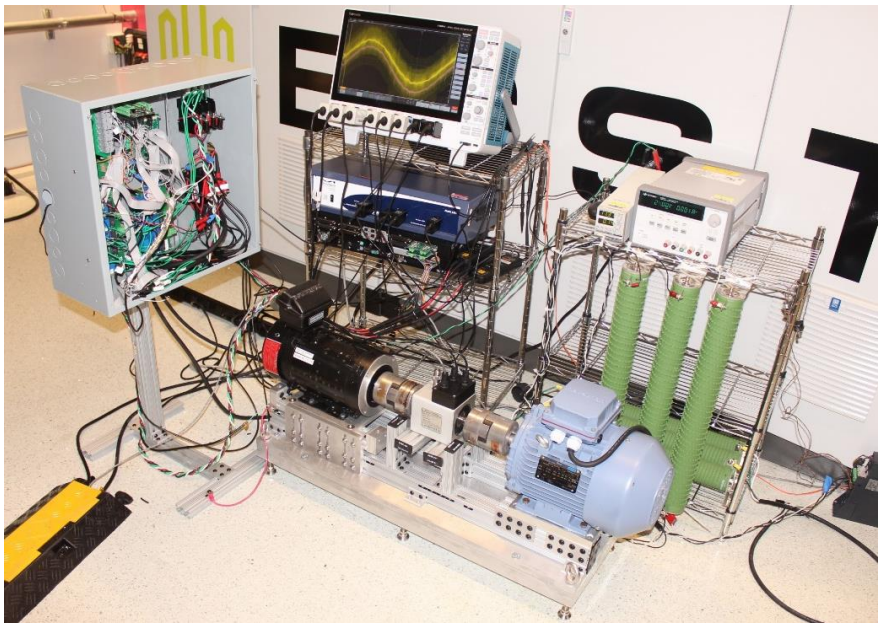

Figure 4.21: Developed TBM characterization setup

Fig 4.22 shows the simplified diagram representing the hardware setup that was developed for this study. In this study OPAL-RT is used to control the PHIL and also for obtaining all the measurements from electrical and mechanical sensors (voltage and current sensors, resolver sensor, and torque sensor). Perturbations generated by FRA are fed to OPAL-RT to generate the power signal that is needed to be applied to the electrical machine and the response signal is fed back from OPAL-RT to the FRA to calculate the desired frequency response for the TBM method. For study of the frequency response for each measurement it is important that all parts of the setup can cover the desired frequency range and as a requirement P-HIL used in this setup should be able to generate the desired small signal perturbation to cover the frequency range. According to the manufacturer's specification for PHIL unit used in this study it is capable of covering up to 15 kHz small signal generation which can cover the desired frequency range needed for this study considering that key dynamic characteristics of the electrical machine are at a much lower frequency range.

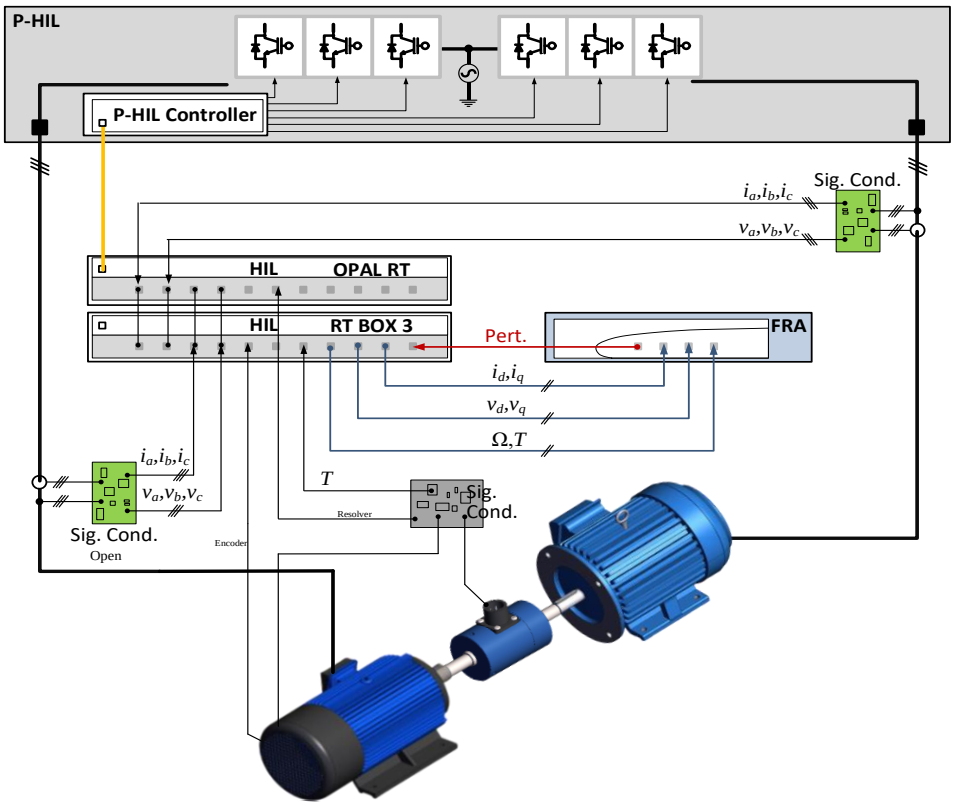

Figure 4.22: Simple diagram of developed machine characterization setup

4.9 IM Inertia Measurement Test

Different methods for calculating the inertia are represented in the literature [61]–[63], however, the measurement capabilities of the developed test setup in this study enable accurate calculation of the inertia using the frequency response characteristics. In this test a method for calculating the inertia of the induction machine is presented. For this test, the electrical connection of the induction machine is opened, and this machine is kept de-energized during the test as shown in Fig 4.23. In this case since there is no current passing through the IM stator windings, no electrical torque is generated with the induction machine and the induction machine acts similar to inertia connected to the mechanical shaft coupling.

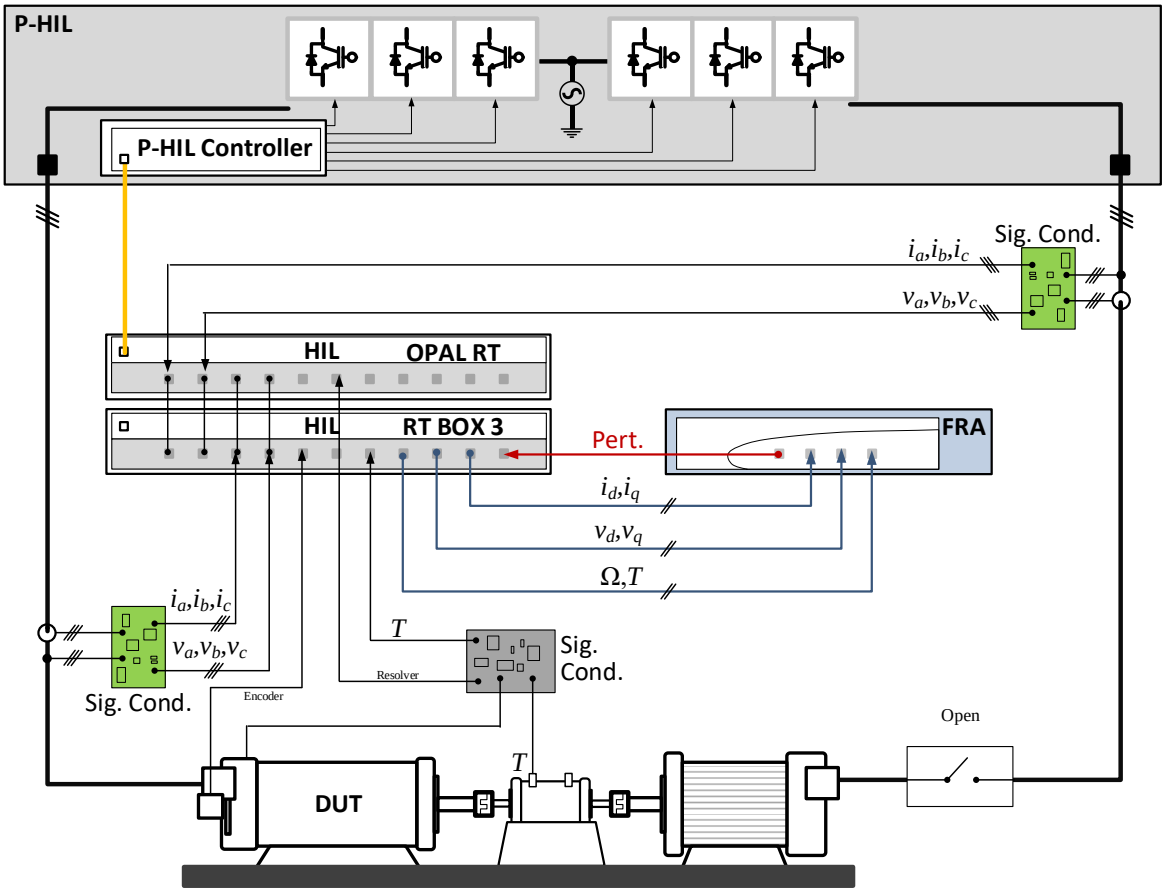

Figure 4.23: Test setup for measuring the inertia of IM

In this case we can draw the simplified electrical equivalent of this setup as Fig. 4.24. In this electrical equivalent, the induction machine is modeled as a capacitor and the PM machine is modeled as a controlled current source connected to the C_{PM} that is representing the inertia related to the PM machine.

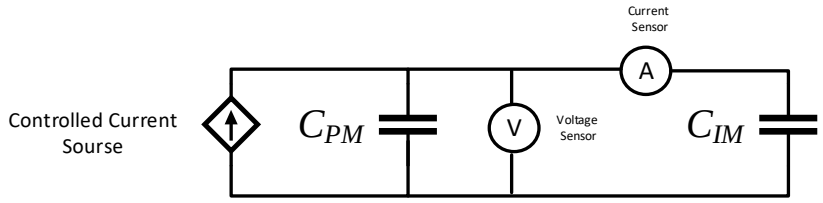

Figure 4.24: Simplified electrical equivalent model for IM inertia measurement setup

Using this setup, it is possible to perform a frequency response test by applying the torque perturbation using the PM machine observing the response on the speed change and calculating the observed mechanical impedance of the system. The frequency range for this test is chosen in the span of 1 to 10Hz. The reason for selecting the low-frequency range for this test is to avoid the potential effects of the non-rigid behavior of the mechanical shaft or other parts of the structure in the measurement. at the higher frequency range. Fig. 4.25 shows the response of the aforementioned experiment and interpolation of this measurement.

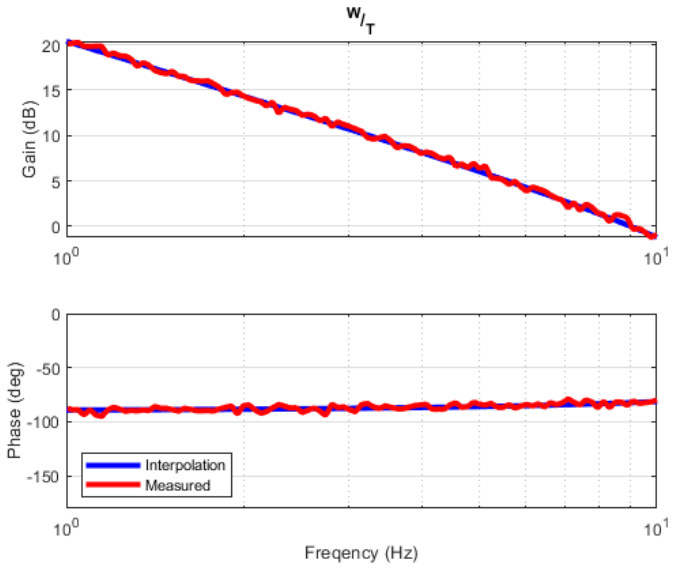

Figure 4.25: Low frequency range of the observed impedance of IM machine

By calculating the gain value of the observed mechanical impedance from the interpolated bode plot at the frequency of 5Hz, mechanical inertia of the IM machine is calculated to be 0.0152 kg.m2 This is simply done by substituting the values of the frequency and measured gain from the bode plot at that frequency based on Eqn. (4.6)

$$Z_{IM} = \frac{1}{C_{IM}S} \tag{4.6}$$

4.10 PM Inertia Measurement Test

In this experiment, the inertia of the PM machine is calculated using a procedure very similar to the method described in the previous section. In this case, the electrical connection to the PM machine is disconnected and PM machine is treated as inertia that is connected to the mechanical shaft similar to Fig 4.26.

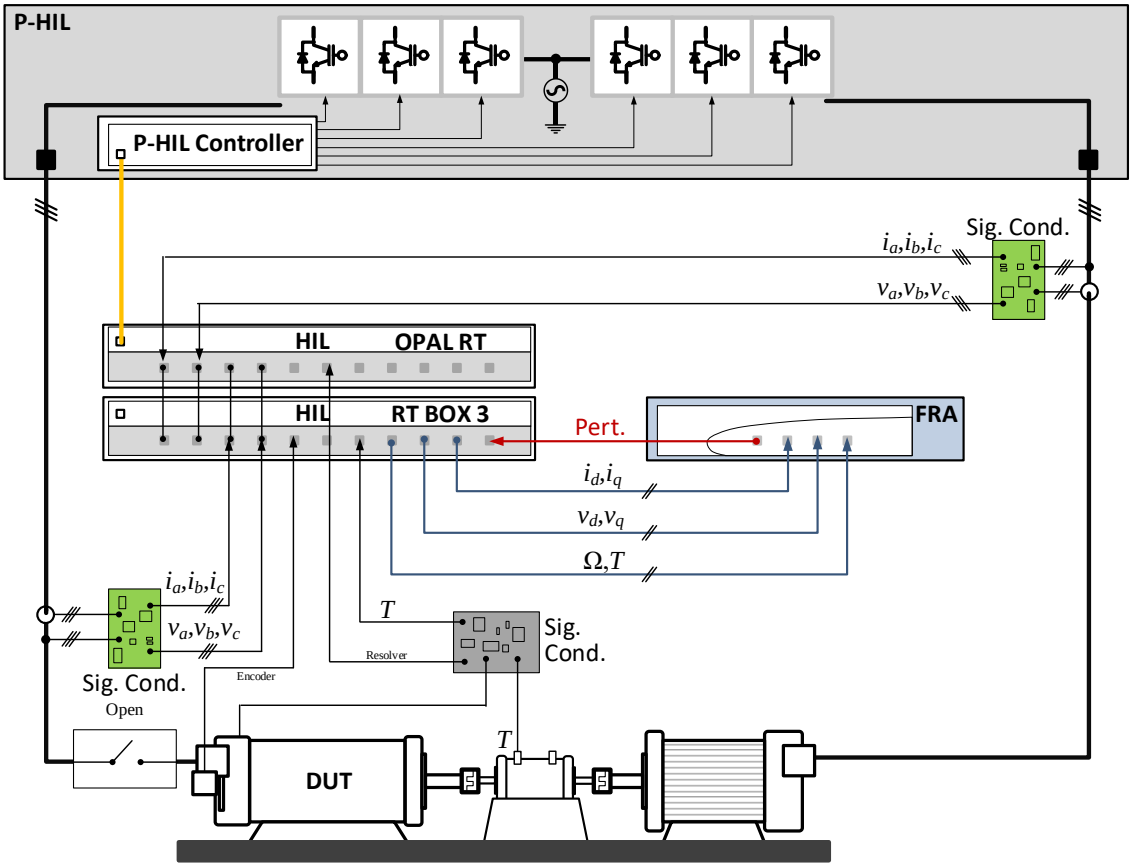

Figure 4.26: Test setup for measuring the inertia of PM

The simplified electrical equivalent for this experiment can be shown in Fig. 4.27. In this case, PM inertia is modeled as a capacitor while the energized IM machine acts similar to a current source connected to a capacitor that models the internal inertia of the IM machine. In this case it is possible to perform a frequency response sweep using the IM machine as the source of the torque perturbation and observe the speed variations using the interpreted speed signal from the mechanical encoder connected to the PM machine.

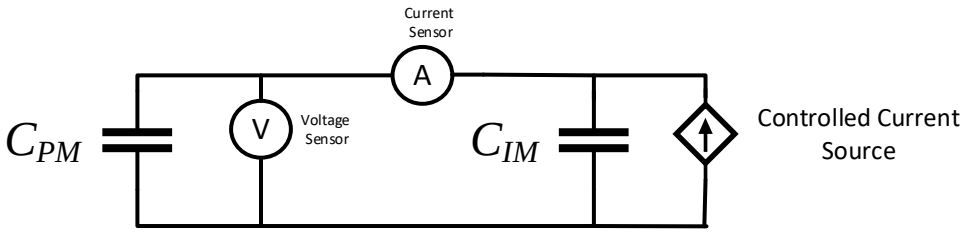

Figure 4.27: Simplified electrical equivalent model for PM inertia measurement setup

Fig 4.28 shows the frequency response results related to this experiment. Similar to the previous part, we can use the value of observed mechanical impedance at low frequency for calculating the value of the inertia. At the lower frequency Eqn. 4.7 can be used to demonstrate the observed impedance related to the PM machine

$$Z_{PM} = \frac{1}{C_{PM}S} \tag{4.7}$$

By substituting the value of the impedance at 5Hz into the equation (4.7), the value of the mechanical inertia of PM machine is calculated to be 0.0067 kg.m^2

As it can be seen in the frequency response, the measured bode plot at frequencies higher than 75 Hz includes a lot of inconsistencies and cannot be interpreted as valid measurements of the impedance. This observation is important since it shows that the potential reason is that an increased impedance of the mechanical coupling between the two machines at the higher frequencies is causing the reduction in the amplitude of the perturbation signal that results in miscalculation of the mechanical impedance of the PM inertia at the higher frequency. This observation is an incentive for having a more accurate model of the mechanical coupler between the two machines.

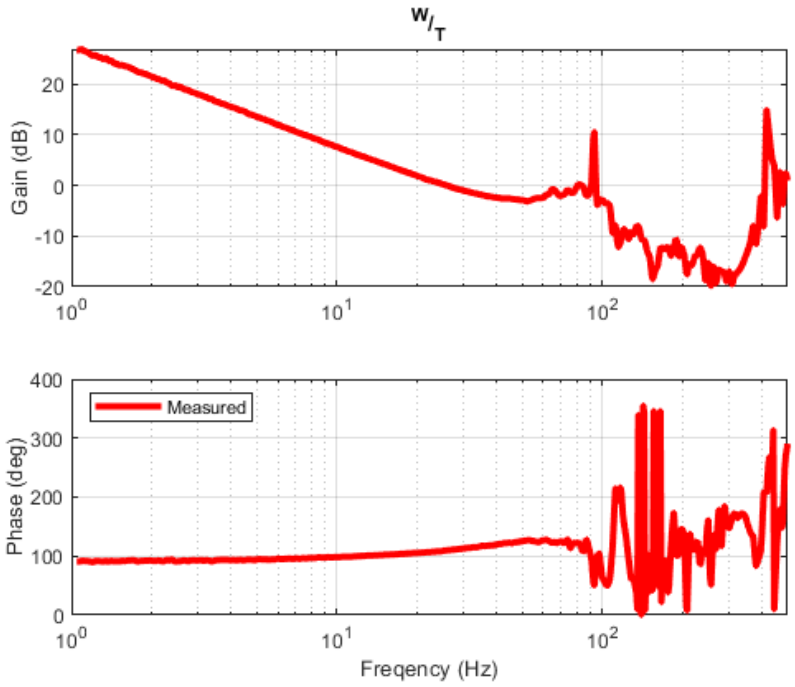

Figure 4.28: Observed impedance of PM machine at low and high frequency range

4.11 Characterization of Mechanical Shaft

Having an accurate model of the mechanical shaft is important in this study since measurement of some of the transfer functions necessary for TBM study requires a perturbation signal to pass through the mechanical shaft and the effect of this mechanical perturbation to be measured in the electrical side of permanent magnet machine. In addition to this, in the case that the dynamics of the mechanical shaft are at the same frequency range as the dynamics of the PM machine, the effect of these dynamics will appear in the TBM measurements. Thus, it is important to have a good model of the mechanical shaft. In order to identify the dynamics of the mechanical shaft, a series of experiments was performed in the test setup. In the first experiment PM machine is energized and IM machine's electrical terminals are opened similar to Fig 4.23. Using this setup frequency response test is performed at the frequency range of 1-200 Hz. Fig 4.29 shows the frequency response related to this test.

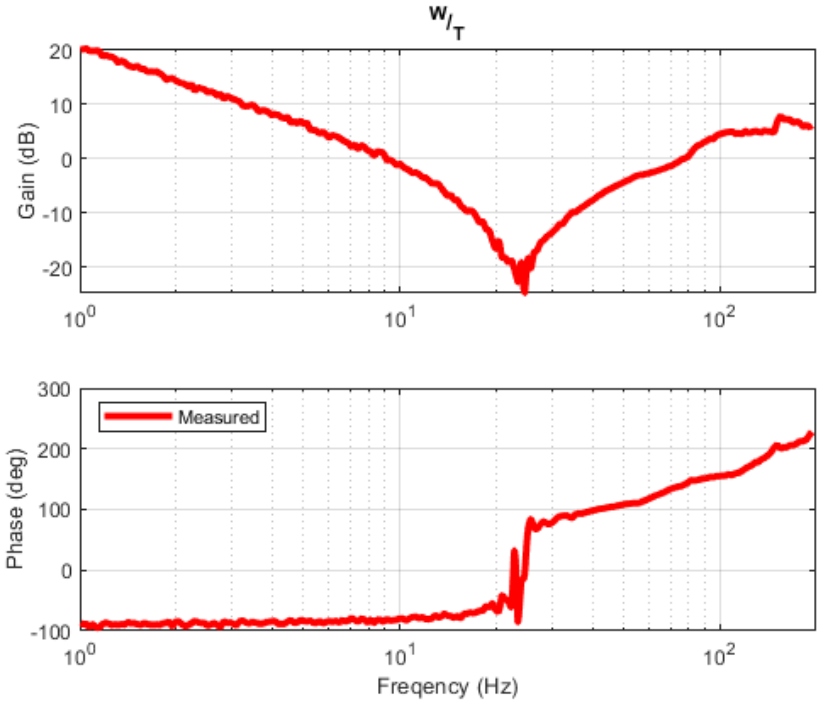

Figure 4.29: Observed impedance of IM and mechanical shaft

This observation shows that the mechanical impedance of the combination of the IM machine and the shaft coupler increases at higher frequencies. In this case we cannot assume that the mechanical shaft is solid at the higher frequency range and we should model this effect with proper mechanical and electrical equivalents. Table 4.3 shows the equivalent models of the mechanical components that are used in this effort for modeling the mechanical shaft coupler.

	Mechanical	**Electrical Equivalent**
Component name	***Damper***	***Resistor***
Symbol	B_{shaft}, w_1, w_2, T	I, v_1, R_{Shaft}
Equation	$T = B_{\text{shaft}}\,(w_1 - w_2)$	$I = R_{\text{shaft}}\,(v_1 - v_2)$
Parameter name	$T = Mechanical\ Torque$ $w_1, w_2 = Speed$ $B_{\text{shaft}} = Rotational\ Damping$	$I = Current$ $v_1, v_2 = Voltage$ $R_{\text{shaft}} = Resistance$
Component name	***Spring***	***Inductor***

Symbol	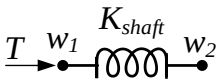	
Equation	$w_1 - w_2 = \frac{1}{K_{\text{shaft}}} \frac{dT}{dt}$	$v_1 - v_2 = L_{\text{shaft}} \frac{dI}{dt}$
Parameter name	$T = Mechanical\ Torque$ $w_1, w_2 = Speed$ $K_{\text{shaft}} = Rotational\ Spring\ Constant$	$I = Current$ $v_1, v_2 = Voltage$ $L_{\text{shaft}} = Inductance$

Table 4.3: Mechanical and electrical equivalent models

As the first attempt effect of the observed dynamics of the mechanical shaft is modeled using the mechanical stiffness model. Fig 4.30 shows this simplified model of the mechanical shaft.

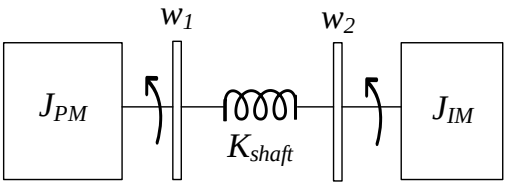

Figure 4.30: Mechanical representation of mechanical shaft stiffness

By comparing the equation related to the mechanical spring and comparing it to an inductor, the electrical equivalent model can be prepared. with an equation related to the voltage across an inductor we can find assume the electrical equivalent of this mechanical model to be similar to Fig. 4.31.

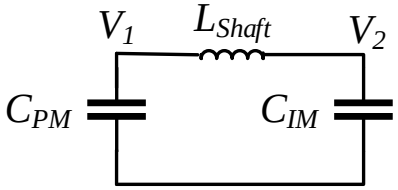

Figure 4.31: Electrical equivalent model of stiffness for mechanical shaft

This electrical equivalent mode can be completed by putting the equivalent of the generated torque of the PM machine as a controlled current source and mechanical speed sensor attached to the PM machine as the voltage sensor equivalent and the torque sensor as the current sensor equivalent. By putting the equivalent inductance into the electrical equivalent of the system we can represent the system as Fig. 4.32.

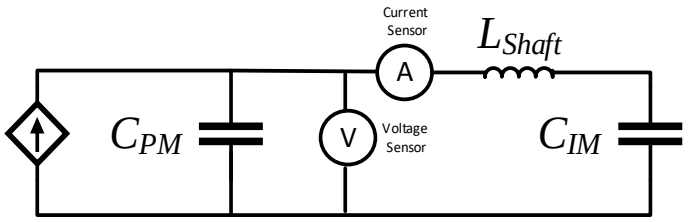

Figure 4.32: Electrical equivalent model of system considering stiffness shaft stiffness

By representing the electrical model in the Laplace domain, the sum of the impedance of the C_{IM} and L_{Shaft} can be represented as Eqn. (4.8)

$$Z_{IM+shaft} = \frac{1+C_{IM}L_{\text{Shaft}}S^2}{C_{IM}S} \tag{4.8}$$

This representation of the combination of the electrical equivalent of IM inertia and compliance (1/stiffness) of the mechanical shaft can describe the increased observed impedance gain at the higher frequencies. By observing the minimum impedance point at the frequency response measurement plot and substituting the value of C_{IM} calculated at the previous section we can calculate the value of equivalent inductance in the electrical equivalent model to be L_{Shaft} =0.0029 H. As the next step we can simulate the observed electrical equivalent model and plot the impedance of the simulated model as Fig 4.33.

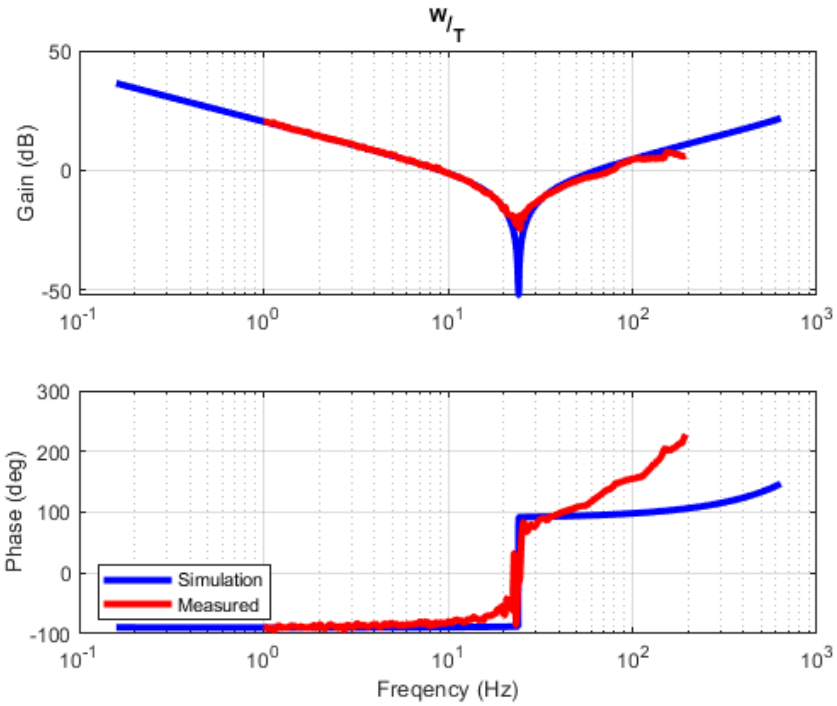

Figure 4.33: Comparison of simulated model and experimental mechanical impedance

As it can be seen from this model, the assumed stiffness for the shaft can properly describe the observed mechanical impedance at the higher frequency however by looking at the minimum value of observed mechanical impedance we can see that the measurement values have higher value than zero. This observation shows that we should add another element to the mechanical and electrical equivalent models to mimic the same observed effect of the observation impedance plot. By adding a damper model in parallel to the stiffness model of the mechanical shaft we can show the mechanical model of the shaft as Fig. 4.34.

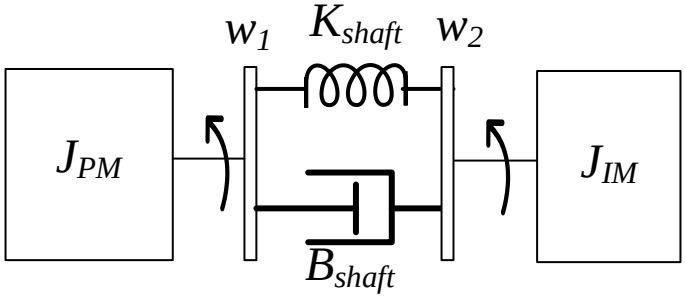

Figure 4.34: Modeling the mechanical shaft as combination of stiffness and damper

Electrical equitant of this mechanical model can be demonstrated as Fig. 4.35.

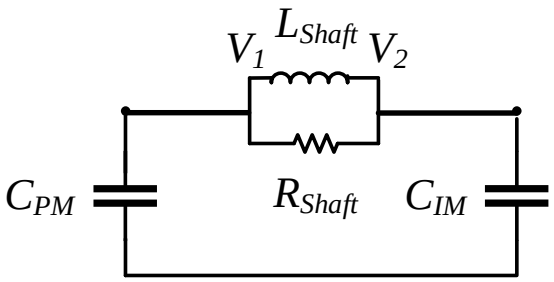

Figure 4.35: Electrical equivalent of the mechanical shaft as with stiffness and damper

By putting the equivalent inductance into the electrical equivalent of the system we can represent the system as Fig. 4.36.

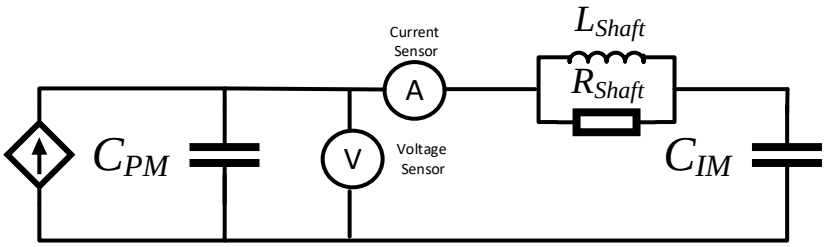

Figure 4.36: Electrical equivalent for IM mechanical impedance measurement test

By representing the electrical model in Laplace domain, the sum of the impedance of the C_{IM} and L_{Shaft} can be represented as Eqn. (4.9)

$$Z_{IM+Shaft} = \frac{1+R_{Shaft}\,C_{IM}S+C_{IM}\,L_{Shaft}\,S^2}{C_{IM}S} \tag{4.9}$$

By substituting the values of C_{IM} and frequency of the minimal impedance of the circuit we can calculate the value for the equivalent resistance of the shaft to be $R_{Shaft} =$ 0.07 ohm. As the next step we can simulate the observed electrical equivalent model and plot the impedance of the simulated model as Fig. 4.37.

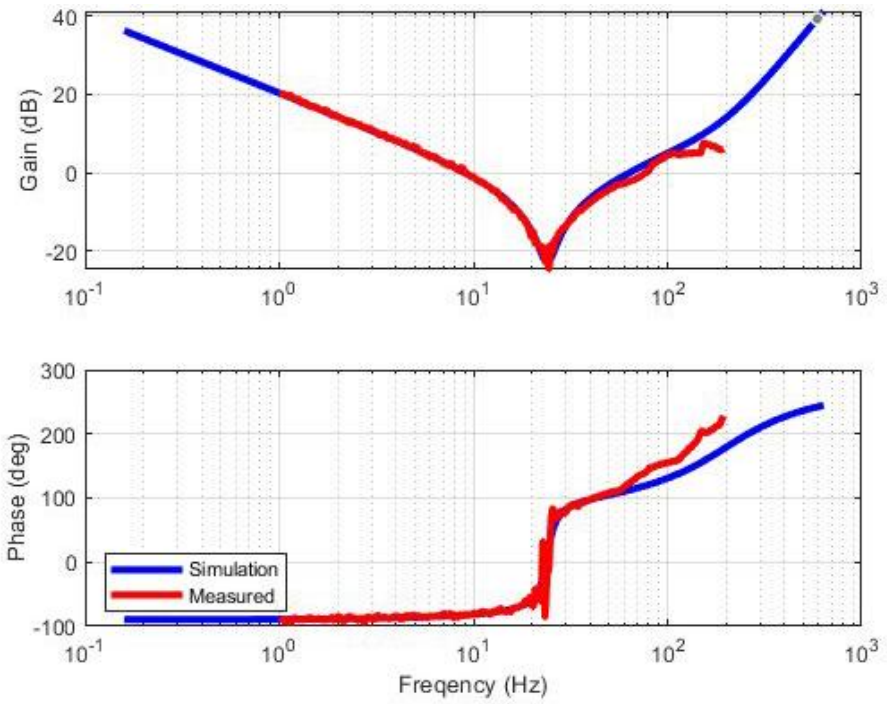

Figure 4.37: Comparison of IM simulation and measured mechanical impedance

As it was demonstrated as a step-by-step model development for mechanical shaft couple, this model was demonstrated suing a parallel combination of a rotary spring and damper. An electrical equivalent to this model was also developed and demonstrated.

4.12 Effect of Shaft Coupler Dynamics

In the previous section it was in the test related to the observed impedance of the PM machine shown that the frequency response at frequency range higher than 75 Hz was not consistent. This can be due to the fact that the high impedance of the mechanical shaft at higher frequencies, reduces the amplitude of the perturbation signal, resulting in the signal-to-noise ratio being lower than the detectable value required by FRA. To verify this assumption an experiment is done by modifying one of the mechanical shaft couplers that is used to couple the two machines together and the effect of this modification on the frequency response measurements related to observed mechanical impedances is studied. Fig 4.38 shows the mechanical shaft coupler used in the first experiment. This shaft coupler

consists of two metal parts with a hard rubber spider insert in between. Fig 4.38 shows the structure of this shaft coupler.

This shaft coupler is then modified by adding a metallic ring to the intersection of the two metal sections. By doing so, this metal ring connects the two metal parts of the shaft coupler together and reduces the effect of the internal rubber part of the shaft coupler by providing a parallel mechanical path to this rubber part. After doing this modification we can repeat the test related to measuring the inertia of the PM machine and compare the observed result with the previous observation. As it can be seen from Fig. 4.38 measured impedance after modifying the shaft coupler (in blue) shows consistent measuring of the impedance up to the frequency of 260 Hz while a similar test with the shaft coupler without the added ring (red) can only show consistent measurements of the impedance up to about 60 Hz. This can verify the assumption related to the effect of the shaft stiffness (mechanical impedance of the shaft) on the span of consistent measurements related to the impedance measurements of the PM machine.

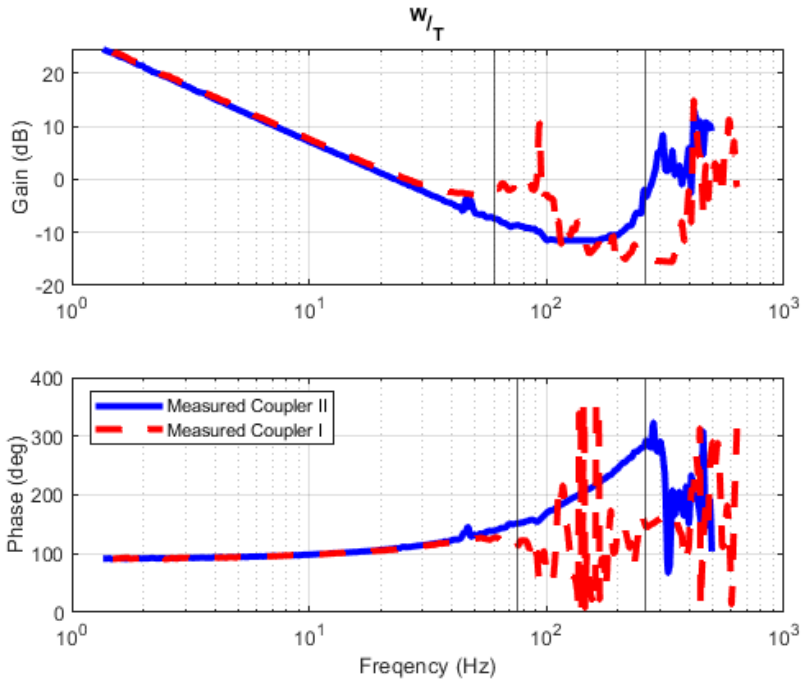

Figure 4.38: Comparison of PM simulation and measured mechanical impedance

In another test we can use the modified shaft coupler to repeat the experiment related to observing the summation of impedance of the IM machine inertia and the

mechanical shaft. By deenergizing the IM machine and using the PM machine as the source of perturbation, we can measure the impedance of the combination of the mechanical shaft and IM machine as Fig. 4.39.

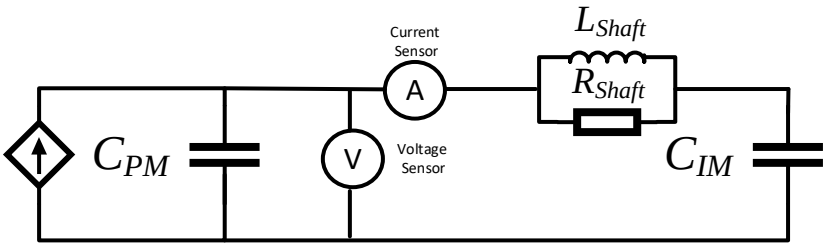

Figure 4.39: Simplified electrical equivalent of IM mechanical impedance

Fig 4.40 shows the comparison related to the measured impedance with two different conditions of the shaft coupler. It can be seen that the measured impedance of the combination of the IM inertia and the mechanical shaft is substantially decreased with the new modification of the shaft coupler. Additionally, the minimum impedance point is moved from 23Hz to around 61Hz. This experiment verifies the assumptions related to the effect of the shaft coupler type on the impedance of the mechanical shaft coupler that connects the two machines together.

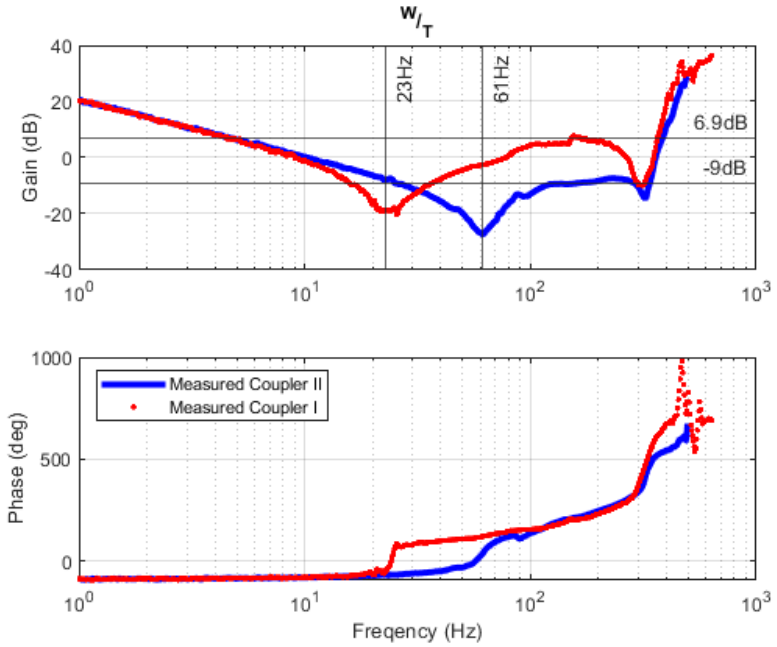

Figure 4.40: Measured mechanical impedance of IM and shaft with different couplers

Similar to the previous calculations, values of the inductance and resistance in the equivalent electrical model of the mechanical shaft can be calculated as shown in table 3.

	L_{Shaft}	R_{Shaft}
Coupler I (Rubber Spider Type)	29 uH	0.4 ohm
Coupler II (Added Metal Ring)	4.6 uH	1.6 ohm

Table 4.4: Measured parameters related to two mechanical shaft combinations

Comparing the values of the electrical equivalent shaft inductance and resistance shows significant decrease in the impedance of the mechanical shaft. This reduction in the impedance of the mechanical shaft is crustal to ensure the quality of the TBM frequency response measurements that requires the perturbation signal to be applied using the IM machine.

4.13 Experimental TBM Characterization of PMSM

The permanent magnet synchronous machine in this setup was controlled with decoupled current controller and outer speed loop controller. Output shaft of the machine was connected to the induction machine. Induction machine was controlled with V/F control strategy. Machines were tested at 1400 rpm and 4 Nm load torque. By performing the frequency response measurement related to the TBM decoupling procedure, resulting frequency response were used to perform the decoupling procedure. After performing the decoupling procedure, decoupled frequency response of the PM machine was calculated. Fig 4.41 shows the resulting decoupled transfer function related to this experiment.

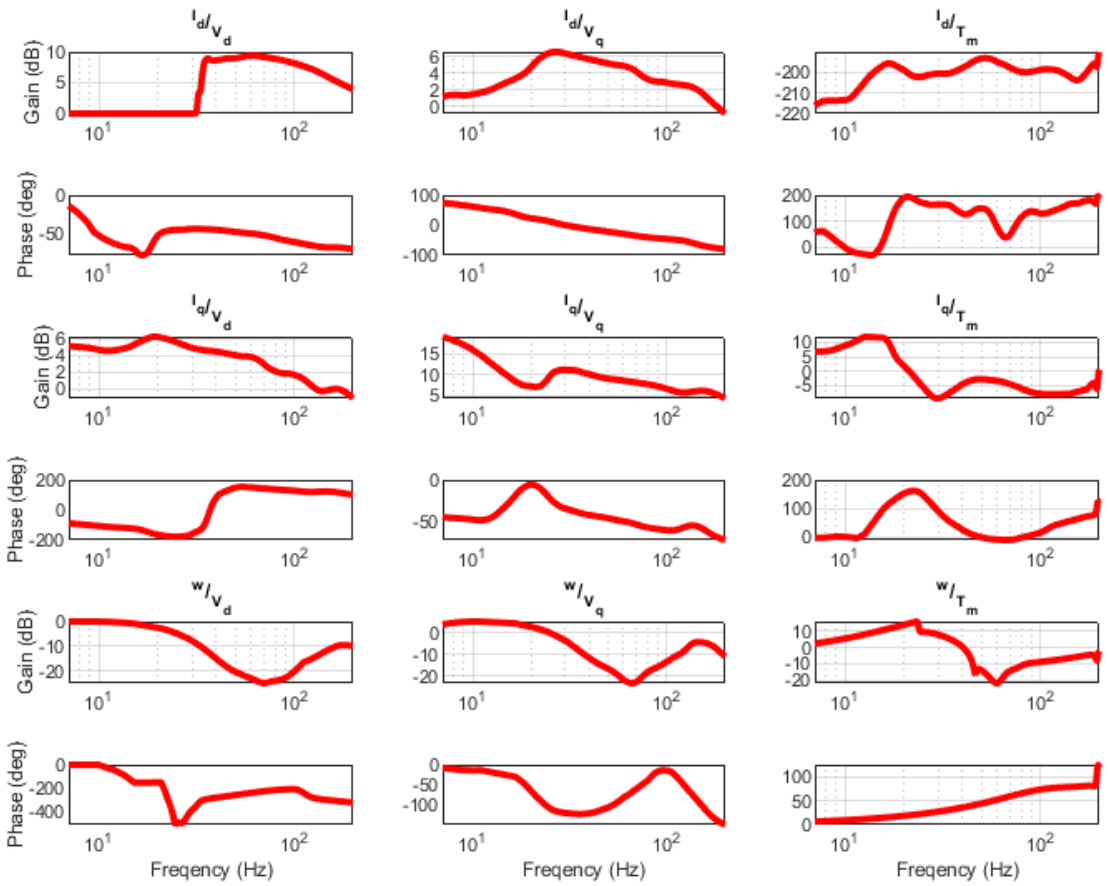

Figure 4.41: Terminal Behavioral Model experimental results

To verify the resulting experimental results another test was performed. In this test a transient torque was imposed using the induction machine, and the response of this transient in d-q frame was recorded using the oscilloscope and HIL. Fig 4.42 shows the measurements of voltages of PMSM in d and q axis and also the torque transient that is imposed on the PM machine. Eqn. 4.10 shows the form of the developed Terminal Behavioral Model for this machine based on demonstrations in Chapter 3.

$$\begin{bmatrix} G_d & G_q & Z_o \\ Y_{dd} & Y_{dq} & H_d \\ Y_{qd} & Y_{qq} & H_q \end{bmatrix} . \begin{bmatrix} \tilde{v}_{id} \\ \tilde{v}_{iq} \\ \tilde{T} \end{bmatrix} = \begin{bmatrix} \tilde{w}_o \\ \tilde{\imath}_{id} \\ \tilde{\imath}_{iq} \end{bmatrix} \tag{4.10}$$

As it can be seen from the TBM matrix, d and q axis voltages and mechanical torque on the shaft are the inputs of the model. In this experiment the input parameters of the

system are measured using measurement HIL and after proper transformation, d and q voltages are recorded as Fig 4.42.

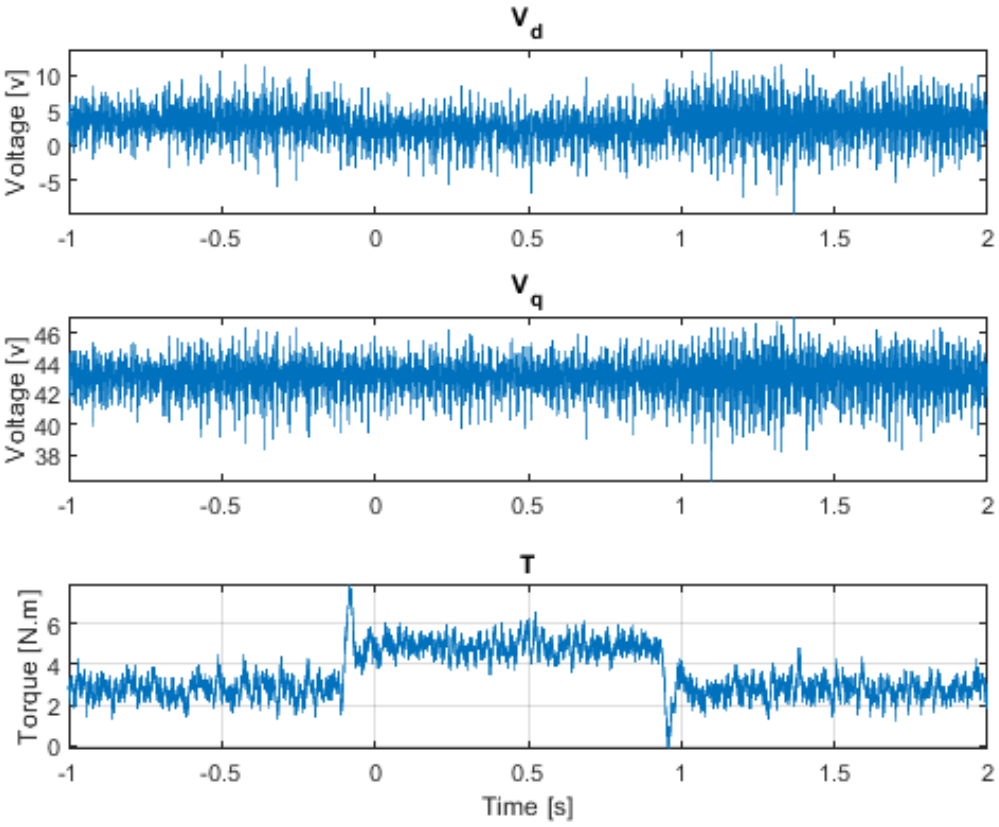

Figure 4.42: Time domain measurements of input variables of TBM model

Similar to the demonstration in Chapter 3, the time-domain response of the TBM model is compared with the recorded measurements in the case of transients in mechanical torque on the shaft. In TBM model currents in d and q axis and speed of the PMSM are the outputs of the model. These outputs of the model are compared with the outputs of the machine and demonstrated in Fig. 4.43.

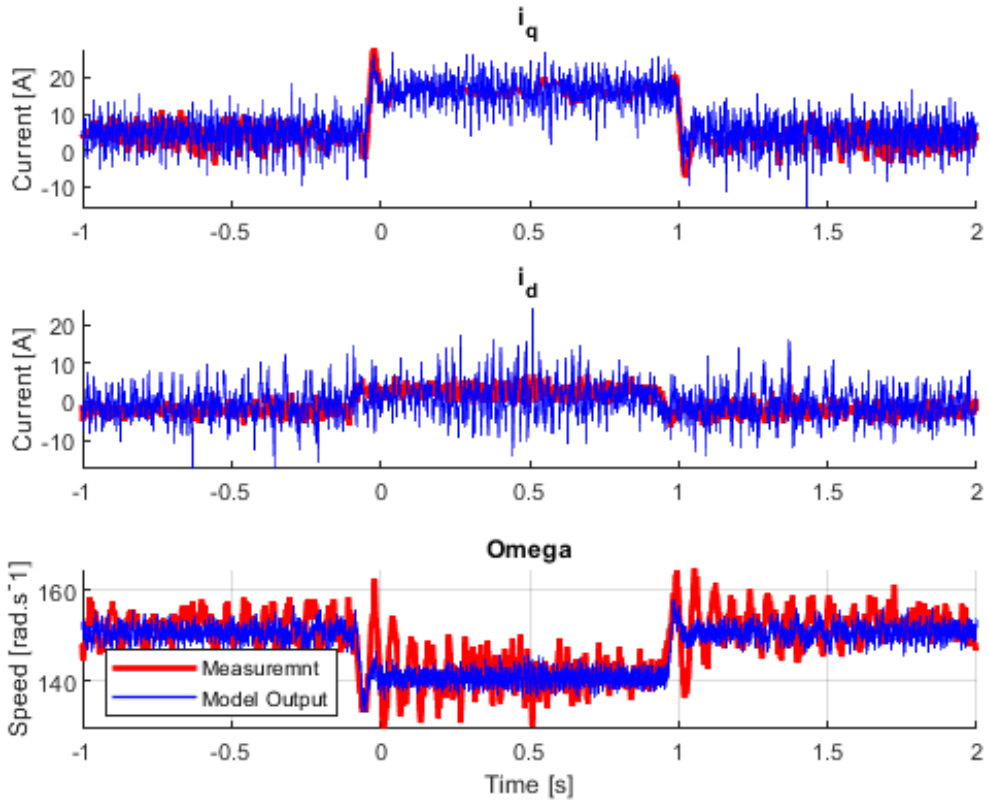

Figure 4.43: Comparison of TBM results and machine real-time emulation

As it can be seen the resulting response from the TBM model is very consistent with the time domain response from the PM machine in presence of a transient in shaft torque.

Chapter 5

Summary and Conclusions

This thesis starts by explaining the motivation for having accurate terminal behavioral models and the importance of having such a model for stability studies. After summarizing the existing art on decoupling procedure for TBM study of power DC-DC converts and three-phase active rectifiers, the application of this method for achieving the decoupled model of the PMSM is presented. Applicability of the decoupling procedure to achieve a black box decoupled model of the machine is then shown mathematically using a small-signal representation of the machine by computing the mathematical form of transfer functions related to the system. This mathematical form shows that individual transfer functions that describe the input-output relationships of the terminals of the machine can be affected by the dynamics related to the electrical source and dynamics of the load coupled through the mechanical shaft. It is then shown that by applying the decoupling procedure, it is possible to decouple all of the dynamics from the load and source and obtain the matrix of transfer functions that represent only the dynamics of the PM machine. In the experimental verification part of this thesis a characterization test setup was developed by integrating a variety of tools such as Hardware-In-The-Loop, Power-Hardware-In-The-Loop, Frequency Response Analyzer, many different sensors such a volage, current, torque, resolver, and encoder, and various other components. Integration of Frequency Responses Analyzer with HIL and PHIL system to perform impedance measurement studies in DC, three-phase AC, and mechanical impedance cases was another achievement in this study. Using the developed testbed frequency response measurements essential for applying the decoupling procedure to calculate the unterminated model of permanent magnet synchronous machine was achieved while the electrical machines were being driven at the operating point of interest. Response of the resulting TBM model of the machine to step changes in the mechanical load was then compared to the actual time domain measurements response of the PMSM at a similar operating point. This comparison showed satisfactory similarity of the achieved model of the machine and the time domain response of the machine in the experimental test which confirms the applicability of this modeling and decoupling procedure for PMSM modeling studies.

References

[1] "Distributed Energy Generation Market Size, Share & Trends Analysis Report By Application (Residential, Commercial & Industrial), By Technology (Fuel Cells, Solar PV), By Region, And Segment Forecasts, 2020 - 2027," 2020.

[2] Robert W. Erickson and Dragan Maksimovic, *Fundamentals of Power Electronics, Second Edition*, 2nd ed. Springer, 2001.

[3] G. Wester, M. R. Ieee Middlebrook, and S. Member, "Low-Frequency Characterization of Switched dc-dc Converters Presented at the Third IEEE Power Processing and Electronic Specialists Conference, Atlantic City, N."

[4] A. Nazari, Y. Xue, J. K. Motwani, I. Cvetkovic, D. Dong, and D. Boroyevich, "Dynamic Phasor Modeling of Multi-Converter Systems," in *2021 IEEE Energy Conversion Congress and Exposition, ECCE 2021 - Proceedings*, 2021, pp. 2716–2721. doi: 10.1109/ECCE47101.2021.9595120.

[5] S. R. Sanders, J. M. Noworolski, X. Z. Liu, and G. C. Verghese, "Generalized Averaging Method for Power Conversion Circuits," *IEEE Transactions on Power Electronics*, vol. 6, no. 2, pp. 251–259, 1991, doi: 10.1109/63.76811.

[6] A. Nazari, Y. Xue, J. K. Motwani, I. Cvetkovic, D. Dong, and D. Boroyevich, "Dynamic phasor modeling of three phase voltage source inverters," 2021. doi: 10.1109/EGRID52793.2021.9712467.

[7] J. K. Motwani, Y. Xue, A. Nazari, D. Dong, I. Cvetkovic, and D. Boroyevich, "Analysis of Inter Converter Interactions using Harmonic State Space Modeling," 2021. doi: 10.1109/eGRID52793.2021.9662130.

[8] "Input filter considerations in design and application of switching regulators - Middlebrook - 1976".

[9] F. Zhao *et al.*, "Control Interaction Modeling and Analysis of Grid-Forming Battery Energy Storage System for Offshore Wind Power Plant," *IEEE Transactions on Power Systems*, vol. 37, no. 1, pp. 497–507, Jan. 2022, doi: 10.1109/TPWRS.2021.3096850.

[10] D. Yang and Y. Sun, "SISO Impedance-Based Stability Analysis for System-Level Small-Signal Stability Assessment of Large-Scale Power Electronics-Dominated Power Systems," *IEEE Transactions on Sustainable Energy*, vol. 13, no. 1, pp. 537–550, Jan. 2022, doi: 10.1109/TSTE.2021.3119207.

[11] I. Cvetkovic, D. Boroyevich, P. Mattavelli, F. C. Lee, and D. Dong, "Unterminated small-signal behavioral model of DC-DC converters," *IEEE Transactions on Power Electronics*, vol. 28, no. 4, pp. 1870–1879, Apr. 2013, doi: 10.1109/TPEL.2012.2215056.

[12] B. Sun, R. Burgos, and D. Boroyevich, "Common-Mode EMI Unterminated Behavioral Model of Wide-Bandgap-Based Power Converters Operating at High Switching Frequency," *IEEE Journal of Emerging and Selected Topics in Power Electronics*, vol. 7, no. 4, pp. 2561–2570, 2019, doi: 10.1109/JESTPE.2018.2888604.

[13] R. M. Nelms, B. W. Evans, and L. L. Grigsby, "Simulation of AC Spacecraft Power Systems," *IEEE Transactions on Industrial Electronics*, vol. 36, no. 3, pp. 398–402, 1989, doi: 10.1109/41.31503.

[14] P. G. Maranesi, V. Tavazzi, and V. Varoli, "Two-Port Characterization of PWM Voltage Regulators at Low Frequencies," *IEEE Transactions on Industrial Electronics*, vol. 35, no. 3, pp. 444–450, 1988, doi: 10.1109/41.3120.

[15] I. G. Park, S. Y. Park, and J. K. Park, "An analysis of boost rectifier," in *IECON Proceedings (Industrial Electronics Conference)*, 1991, vol. 1, pp. 519–524. doi: 10.1109/iecon.1991.239231.

[16] O. P. Mandhana and R. G. Hoft, "Two-port characterization of DC to DC resonant converters," *Conference Procedings - IEEE Applied Power Electronics Conference and Exhibition - APEC*, pp. 737–745, 1990, doi: 10.1109/apec.1990.66376.

[17] V. Agarwal and A. K. S. Bhat, "Small signal equivalent circuit modeling of the LCC-type parallel resonant converter," in *Proceedings of the International Conference on Power Electronics and Drive Systems*, 1995, vol. 1, pp. 146–151. doi: 10.1109/peds.1995.404932.

[18] A. K. S. Bhat, "Generalized steady-state analysis of resonant converters using two-port model and Fourier-series approach," in *Conference Proceedings - IEEE Applied Power Electronics Conference and Exposition - APEC*, 1995, vol. 2, pp. 920–926. doi: 10.1109/apec.1995.469050.

[19] C. Y. Lin and F. C. Lee, "Design of a piezoelectric transformer converter and its matching networks," in *PESC Record - IEEE Annual Power Electronics Specialists Conference*, 1994, vol. 1, pp. 607–612. doi: 10.1109/pesc.1994.349674.

[20] I. Stevanović, B. Wunsch, G. L. Madonna, and S. Skibin, "High-frequency behavioral multiconductor cable modeling for EMI simulations in power electronics," *IEEE Transactions on Industrial Informatics*, vol. 10, no. 2, pp. 1392–1400, 2014, doi: 10.1109/TII.2014.2307198.

[21] I. Stevanović and S. Skibin, “Behavioral circuit modeling of single- and three-phase chokes for EMI simulations,” in *2010 International Power Electronics Conference - ECCE Asia -, IPEC 2010*, 2010, pp. 2867–2871. doi: 10.1109/IPEC.2010.5544583.

[22] M. Belkhayat, “STABILITY CRITERIA FOR AC POWER SYSTEMS WITH REGULATED LOADS,” 1997.

[23] S. Golestan, E. Ebrahimzadeh, B. Wen, J. M. Guerrero, and J. C. Vasquez, “Dq-Frame Impedance Modeling of Three-Phase Grid-Tied Voltage Source Converters Equipped with Advanced PLLs,” *IEEE Transactions on Power Electronics*, vol. 36, no. 3, pp. 3524–3539, Mar. 2021, doi: 10.1109/TPEL.2020.3017387.

[24] C. Li, R. Burgos, B. Wen, Y. Tang, and D. Boroyevich, “Analysis of STATCOM Small-Signal Impedance in the Synchronous d-q Frame,” *IEEE Journal of Emerging and Selected Topics in Power Electronics*, vol. 8, no. 2, pp. 1894–1910, Jun. 2020, doi: 10.1109/JESTPE.2019.2942332.

[25] H. Hu, H. Tao, F. Blaabjerg, X. Wang, Z. He, and S. Gao, “Train-Network Interactions and Stability Evaluation in High-Speed Railways-Part I: Phenomena and Modeling,” *IEEE Transactions on Power Electronics*, vol. 33, no. 6, pp. 4627–4642, Jun. 2018, doi: 10.1109/TPEL.2017.2781880.

[26] B. Wen, D. Boroyevich, R. Burgos, P. Mattavelli, and Z. Shen, “Analysis of D-Q Small-Signal Impedance of Grid-Tied Inverters,” *IEEE Transactions on Power Electronics*, vol. 31, no. 1, pp. 675–687, Jan. 2016, doi: 10.1109/TPEL.2015.2398192.

[27] J. Sun, “Two-Port Characterization and Transfer Immittances of AC-DC Converters–Part II: Applications,” *IEEE Open Journal of Power Electronics*, vol. 2, pp. 483–510, Aug. 2021, doi: 10.1109/ojpel.2021.3104496.

[28] M. Khayamy and H. Chaoui, “Current Sensorless MTPA Operation of Interior PMSM Drives for Vehicular Applications,” *IEEE Transactions on Vehicular Technology*, vol. 67, no. 8, pp. 6872–6881, Aug. 2018, doi: 10.1109/TVT.2018.2823538.

[29] W. Lu *et al.*, “Load Adaptive PMSM Drive System Based on an Improved ADRC for Manipulator Joint,” *IEEE Access*, vol. 9, pp. 33369–33384, 2021, doi: 10.1109/ACCESS.2021.3060925.

[30] C. Chen, W. Du, H. Wang, and T. Littler, “Sub-synchronous oscillations in power systems caused by grid-connected wind farms — A survey of mechanism studies,” *CSEE Journal of Power and Energy Systems*, vol. 4, no. 4, pp. 495–503, Dec. 2018, doi: 10.17775/CSEEJPES.2018.00560.

[31] D. M. Yehia, D. E. A. Mansour, and W. Yuan, "Fault Ride-Through Enhancement of PMSG Wind Turbines with DC Microgrids Using Resistive-Type SFCL," *IEEE Transactions on Applied Superconductivity*, vol. 28, no. 4, Jun. 2018, doi: 10.1109/TASC.2018.2821362.

[32] M. F. M. Arani and Y. A. R. I. Mohamed, "Assessment and Enhancement of a Full-Scale PMSG-Based Wind Power Generator Performance under Faults," *IEEE Transactions on Energy Conversion*, vol. 31, no. 2, pp. 728–739, Jun. 2016, doi: 10.1109/TEC.2016.2526618.

[33] I. Cvetkovic *et al.*, "Modeling and Control of Voltage-Controlling Converters for Enhanced Operation of Multi-Source Power Systems," 2017.

[34] "D. W. Novotny, T. A. Lipo - Vector Control and Dynamics of AC Drives (Monographs in Electrical and Electronic Engineering, 41)-Clarendon Press (1996)".

[35] H. Lin, H. Guo, and H. Qian, "Design of High-performance Permanent Magnet Synchronous Motor for Electric Aircraft Propulsion."

[36] D. Lee *et al.*, "Design and Prototype of a High Power Density Slotless PMSM for Direct Drive Aircraft Propulsion," Apr. 2021. doi: 10.1109/PECI51586.2021.9435256.

[37] A. M. EL-Refaie, "Fault-tolerant PM machines: A review," in *2009 IEEE International Electric Machines and Drives Conference, IEMDC '09*, 2009, pp. 1700–1709. doi: 10.1109/IEMDC.2009.5075432.

[38] J. Sun, "Small-signal methods for AC distributed power systems-A review," *IEEE Transactions on Power Electronics*, vol. 24, no. 11. pp. 2545–2554, 2009. doi: 10.1109/TPEL.2009.2029859.

[39] J. Liu, X. Feng, F. C. Lee, and D. Borojevich, "Stability Margin Monitoring for DC Distributed Power Systems via Perturbation Approaches," *IEEE Transactions on Power Electronics*, vol. 18, no. 6, pp. 1254–1261, Nov. 2003, doi: 10.1109/TPEL.2003.818822.

[40] F. Gao and S. Bozhko, "Modeling and impedance analysis of a single dc bus-based multiple-source multiple-load electrical power system," *IEEE Transactions on Transportation Electrification*, vol. 2, no. 3, pp. 335–346, Sep. 2016, doi: 10.1109/TTE.2016.2592680.

[41] X. Feng, C. Liu, Z. Ye, and F. C. Lee, "Monitoring the Stability of DC Distributed Power Systems* Blacksburg, VA 2406 1-0 1 1 1 **."

[42] X. Feng and F. C. Lee, "On-line Measurement on Stability Margin 04 DC Distributed Power System*."

[43] A. Riccobono and E. Santi, "Comprehensive review of stability criteria for DC power distribution systems," *IEEE Transactions on Industry Applications*, vol. 50, no. 5, pp. 3525–3535, Sep. 2014, doi: 10.1109/tia.2014.2309800.

[44] A. Rygg and M. Molinas, “Apparent Impedance Analysis: A Small-Signal Method for Stability Analysis of Power Electronic-Based Systems,” *IEEE Journal of Emerging and Selected Topics in Power Electronics*, vol. 5, no. 4, pp. 1474–1486, Dec. 2017, doi: 10.1109/JESTPE.2017.2729596.

[45] B. Wen, D. Boroyevich, R. Burgos, P. Mattavelli, and Z. Shen, “Small-Signal Stability Analysis of Three-Phase AC Systems in the Presence of Constant Power Loads Based on Measured d-q Frame Impedances,” *IEEE Transactions on Power Electronics*, vol. 30, no. 10, pp. 5952–5963, Oct. 2015, doi: 10.1109/TPEL.2014.2378731.

[46] F. Gao and S. Bozhko, “Modeling and impedance analysis of a single dc bus-based multiple-source multiple-load electrical power system,” *IEEE Transactions on Transportation Electrification*, vol. 2, no. 3, pp. 335–346, Sep. 2016, doi: 10.1109/TTE.2016.2592680.

[47] S. J. Mason, “Feedback Theory—Further Properties of Signal Flow Graphs,” *Proceedings of the IRE*, vol. 44, no. 7, pp. 920–926, 1956, doi: 10.1109/JRPROC.1956.275147.

[48] A. Guha and G. Narayanan, “Impact of Undercompensation and Overcompensation of Dead-Time Effect on Small-Signal Stability of Induction Motor Drive,” *IEEE Transactions on Industry Applications*, vol. 54, no. 6, pp. 6027–6041, Nov. 2018, doi: 10.1109/TIA.2018.2846719.

[49] A. Guha and G. Narayanan, “Small-signal stability analysis of an open-loop induction motor drive including the effect of inverter deadtime,” *IEEE Transactions on Industry Applications*, vol. 52, no. 1, pp. 242–253, Jan. 2016, doi: 10.1109/TIA.2015.2464305.

[50] A. Rygg and M. Molinas, “Apparent Impedance Analysis: A Small-Signal Method for Stability Analysis of Power Electronic-Based Systems,” *IEEE Journal of Emerging and Selected Topics in Power Electronics*, vol. 5, no. 4, pp. 1474–1486, Dec. 2017, doi: 10.1109/JESTPE.2017.2729596.

[51] A. Riccobono and E. Santi, “Comprehensive review of stability criteria for DC power distribution systems,” *IEEE Transactions on Industry Applications*, vol. 50, no. 5, pp. 3525–3535, Sep. 2014, doi: 10.1109/tia.2014.2309800.

[52] J. Sun, “Small-signal methods for AC distributed power systems-A review,” *IEEE Transactions on Power Electronics*, vol. 24, no. 11. pp. 2545–2554, 2009. doi: 10.1109/TPEL.2009.2029859.

[53] M. Kazerooni and N. C. Kar, “Methods for determining the parameters and characteristics of PMSM,” in *2011 IEEE International Electric Machines and Drives Conference, IEMDC 2011*, 2011, pp. 955–960. doi: 10.1109/IEMDC.2011.5994944.

[54] K. Liu, C. Hou, and W. Hua, “A Novel Inertia Identification Method and Its Application in PI Controllers of PMSM Drives,” *IEEE Access*, vol. 7, pp. 13445–13454, 2019, doi: 10.1109/ACCESS.2019.2894342.

[55] I. Omrane, E. Etien, O. Bachelier, and W. Dib, “A simplified least squares identification of permanent magnet synchronous motor parameters at standstill,” in *IECON Proceedings (Industrial Electronics Conference)*, 2013, pp. 2578–2583. doi: 10.1109/IECON.2013.6699537.

[56] T. Tandel, S. Matani, S. Pillai, S. Chaudhuri, A. Gupta, and S. Gupta, “Parameter Estimation Algorithm of Surface-PMSM for FOC, Rotor Angle and Speed Estimation,” 2022. doi: 10.1109/DELCON54057.2022.9753111.

[57] V. Rallabandi, N. Taran, D. M. Ionel, and P. Zhou, “Inductance testing for IPM synchronous machines according to the new IEEE Std 1812 and typical laboratory practices,” *IEEE Transactions on Industry Applications*, vol. 55, no. 3, pp. 2649–2659, May 2019, doi: 10.1109/TIA.2019.2897668.

[58] D. A. Khaburi, “Software-based resolver-to-digital converter for DSP-based drives using an improved angle-tracking observer,” *IEEE Transactions on Instrumentation and Measurement*, vol. 61, no. 4, pp. 922–929, Apr. 2012, doi: 10.1109/TIM.2011.2179825.

[59] S. H. Hwang, H. J. Kim, J. M. Kim, L. Liu, and H. Li, “Compensation of amplitude imbalance and imperfect quadrature in resolver signals for PMSM drives,” *IEEE Transactions on Industry Applications*, vol. 47, no. 1, pp. 134–143, Jan. 2011, doi: 10.1109/TIA.2010.2091477.

[60] S. Chen, Y. Zhao, H. Qiu, and X. Ren, “High-Precision Rotor Position Correction Strategy for High-Speed Permanent Magnet Synchronous Motor Based on Resolver,” *IEEE Transactions on Power Electronics*, vol. 35, no. 9, pp. 9718–9728, Sep. 2020, doi: 10.1109/TPEL.2020.2968502.

[61] K. Liu, C. Hou, and W. Hua, “A Novel Inertia Identification Method and Its Application in PI Controllers of PMSM Drives,” *IEEE Access*, vol. 7, pp. 13445–13454, 2019, doi: 10.1109/ACCESS.2019.2894342.

[62] S. Hall, Y. Loayza, A. Reinap, and M. Alakula, “Consistency analysis of torque measurements performed on a PMSM using dynamic testing,” in *Proceedings - 2014 International Conference on Electrical Machines, ICEM 2014*, Nov. 2014, pp. 1529–1535. doi: 10.1109/ICELMACH.2014.6960385.

[63] K. Liu and Z. Zhu, “Fast Determination of Moment of Inertia of Permanent Magnet Synchronous Machine Drives for Design of Speed Loop Regulator,” *IEEE Transactions on*

Control Systems Technology, vol. 25, no. 5, pp. 1816–1824, Sep. 2017, doi: 10.1109/TCST.2016.2615090.